Lehrstuhl E15
Physik - Department

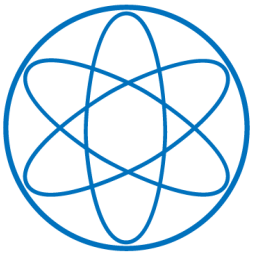

Monte Carlo Study of Solar ^{8}B Neutrinos and the Diffuse Supernova Neutrino Background in LENA

Dissertation
von

Randolph Möllenberg

Technische Universität
München

Technische Universität München

Lehrstuhl E15 für Experimentalphysik und Astroteilchenphysik

Monte Carlo Study of Solar ^{8}B Neutrinos and the Diffuse Supernova Neutrino Background in LENA

Randolph Möllenberg

Vollständiger Abdruck der von der Fakultät für Physik der Technischen Universität München zur Erlangung des akademischen Grades eines

Doktors der Naturwissenschaften (Dr. rer. nat.)

genehmigten Dissertation.

Vorsitzender: Univ.-Prof. Dr. H. Kaiser

Prüfer der Dissertation:

1. Univ.-Prof. Dr. L. Oberauer
2. Univ.-Prof. S. Bishop, Ph.D.

Die Dissertation wurde am 16.10.2013 bei der Technischen Universität München eingereicht und durch die Fakultät für Physik am 26.11.2013 angenommen.

Abstract

LENA (**L**ow **E**nergy **N**eutrino **A**stronomy) has been proposed as a next generation 50 kt liquid scintillator detector. One of its main physics goal is the high precision measurement of solar ^{8}B neutrinos, allowing an energy dependent measurement of the electron neutrino survival probability P_{ee}, which is sensitive to new physics. Another important goal is the detection of the Diffuse Supernova Neutrino Background (DSNB), as the average supernova neutrino spectrum can be extracted from the DSNB spectrum.

Due to its large target mass, LENA can perform a high statistics measurement of solar ^{8}B neutrinos with an unprecedentedly low energy threshold of 2 MeV. Hence, it will be possible to perform a precision test of the MSW-LMA prediction for P_{ee}. This prediction includes an increase of P_{ee} with decreasing energy. As a prerequisite for this analysis, an energy reconstruction algorithm was developed and tested with a full detector Monte Carlo simulation based on GEANT4. No systematic shift between the true and the reconstructed energy was found and the energy resolution was 6.5 % at 1 MeV. Based on simulations of the expected ^{8}B neutrino spectrum and of the background spectra, it was found that after 5 y of data taking a test model with constant P_{ee} can be excluded with $5\,\sigma$ significance, even if the concentration of radioactive isotopes in the scintillator is two orders of magnitude larger than in Borexino. Hence, if the upturn of the ^{8}B spectrum is not detected in LENA after 5 y, this would rule out the MSW-LMA prediction and show that new physics influence P_{ee} in the transition region between matter and vacuum dominated oscillations.

Besides detecting neutrinos from a rare supernova in our galaxy, LENA will also search for the DSNB, which was generated by core-collapse supernovae throughout the universe. In order to determine the detection potential of LENA, the DSNB and all relevant background spectra were simulated. The backgrounds from reactor and atmospheric antielectron neutrinos limit the detection window to energies between 9.5 MeV and 25 MeV. Depending on the mean supernova neutrino energy, about 50 to 100 events are expected per 10 y in this energy window. The background from neutral current reactions of atmospheric neutrinos of all flavours is more than one order of magnitude larger than the DSNB signal. But this background can be reduced by a pulse shape analysis to 21.8 ± 0.4(stat.) events per 10 y, though this cut will also reduce the DSNB event rate by 60 %. Assuming that the expected value of the background rate is known with 5 % uncertainty, the DSNB can be detected with more than $3\,\sigma$ significance after 10 y of data taking. In case that no DSNB signal is found with LENA, all current standard DSNB models would be ruled out with more than 90 % C.L.

Zusammenfassung

LENA ist ein zukünftiger 50 kt Flüssigszintillationsdetekor. Eines seiner physikalischen Ziele ist die Hochpräzisionsmessung von solaren ^{8}B neutrinos. Dies ermöglicht eine Energieabhängige Messung der Elektronneutrino Überlebenswahrscheinlichkeit P_{ee}, die durch neue Physik beeinflusst werden kann. Ein anderes wichtiges Ziel ist die Detektion des Diffusen Supernova Neutrino Untergrundes (DSNB), weil man dadurch das durchschnittliche Supernovaneutrinospektrum bestimmen kann.
Aufgrund seiner großen Masse ist LENA in der Lage eine Hochpräzisionsmessung von solaren ^{8}B Neutrinos mit einer beispiellos niedrigen Energieschwelle von 2 MeV durchzuführen. Folglich kann ein Präzisionstest der MSW-LMA Vorhersage für P_{ee}, die einen Anstieg mit sinkender Energie prognostiziert, durchgeführt werden. Für diese Analyse wurde eine Energierekonstruktionsalgorithmus entwickelt, der anschließend mit einer Monte-Carlo-Simulation getestet wurde, die auf GEANT4 basiert. Es wurde keine systematische Abweichung zwischen der tatsächlichen und der rekonstruierten Energie festgestellt und die Energieauflösung betrug 6.5 % bei 1 MeV. Anschließend wurden 10^5 Messungen des solaren ^{8}B Neutrinospektrums, inklusive aller relevanter Untergründe, simuliert. Nach 5 Jahren kann ein Testmodell mit konstanten P_{ee} mit $5\,\sigma$ Signifikanz ausgeschlossen werden, selbst wenn die Konzentration von radioaktiven Isotopen im Szintillator hundert Mal größer ist als in Borexino. Falls der Anstieg des ^{8}B Spektrums nicht detektiert wird, muss neue Physik P_{ee} im Übergangsbereich zwischen Materie und Vakuum dominierten Oszillationen beeinflussen.
LENA kann nicht nur Neutrinos von einer Supernova in der Milchstraße detektieren, sondern wird auch nach dem DSNB suchen, der von allen Supernovae, die es im Universum gegeben hat, erzeugt wurde. Um das Detektionspotential von LENA zu bestimmen, wurde das DSNB-Spektrum und alle relevanten Untergrundspektren simuliert. Die Untergründe von Reaktor und atmosphärischen Antielektronneutrinos begrenzen das Energiefenster auf Energien zwischen 9.5 MeV und 25 MeV. In diesem Energiefenster werden zwischen 50 und 100 Ereignisse erwartet, abhängig von der mittleren Energie der Supernovaneutrinos. Der Untergrund der durch die neutralen Stromwechselwirkung von atmosphärischen Neutrinos verursacht wird ist mehr als zehn Mal so groß wie das DSNB-Signal. Jedoch kann dieser Untergrund durch eine Pulsformanalyse auf 21.8 ± 0.4(stat.) Ereignisse pro 10 Jahre reduziert werden, was allerdings die DSNB-Ereignissrate um 60 % verringert. Falls der Erwartungswert der Untergrundrate mit 5 % Genauigkeit bekannt ist, kann der DSNB nach 10 Jahren mit mehr als $3\,\sigma$ Signifikanz detektiert werden. Falls kein DSNB-Signal gefunden wird, würden alle heutigen standard DSNB-Modelle mit 90 % C.L. ausgeschlossen werden.

Contents

Chapter 1

Introduction

Neutrinos only interact weakly and thus are only marginally affected by matter and point back directly to their source. Hence, neutrinos offer the possibility to directly look inside an astrophysical object or phenomema, like core-collapse supernovae, the sun or the earth itself. But as the interaction cross section for neutrinos with matter is very low, it is also very hard to detect them. Thus, a large detector mass is needed to measure neutrinos from astrophysical objects [1]. The proposed LENA (**L**ow **E**nergy **N**eutrino **A**stronomy) detector is a 50 kt liquid scintillator detector [2]. Due to its large target mass and low energy threshold (200 keV), LENA is capable of performing high statistics measurements of solar neutrinos. Using these measurements, it is possible to study the fusion process in the sun. But it is also possible to learn something about the neutrino itself, for example by measuring the energy dependent survival probability for solar ^{8}B neutrinos. This measurement is very important as new physics could influence the survival probability in the transition region between vacuum and matter dominated oscillations ($2\,\mathrm{MeV} < \mathrm{E}_\nu < 5\,\mathrm{MeV}$).
Furthermore, besides measuring geoneutrinos and possibly supernova neutrinos, LENA could be the first experiment to detect the Diffuse Supernova Neutrino Background (DSNB), which is generated by the cumulative emission of all core-collapse supernovae throughout the universe. Its detection is very challenging as, even in such a huge detector, only 5 to 10 events are expected per year. Hence, background suppression is a critical issue for this measurement.
In the present Chapter, a short introduction about neutrino oscillations, solar neutrinos and the DSNB will be given. Furthermore, the Water-Čerenkov and liquid scintillator detector technology will be briefly described. In Chapter 2, the detector layout and the physics program of the LENA detector will be outlined. The energy reconstruction of point like events in LENA will be discussed in Chapter 3, which is a prerequisite for the following studies. Additionally, a description of the GEANT4 based LENA Monte Carlo simulation, which was used for the studies in

this thesis, will be given. In Chapter 4, a Monte Carlo study about the sensitivity of LENA to detect deviations of the energy dependent neutrino survival probability from the MSW-LMA prediction by measuring ^{8}B solar neutrinos will be presented. In case that a significant deviation would be detected, this would mean that new physics like non-standard neutrino interactions or light sterile neutrinos have to be introduced. The identification and suppression of background events by pulse shape analysis will be discussed in Chapter 5. This pulse shape analysis can be used to suppress the ^{210}Po alpha background for the measurement of solar ^{7}Be neutrinos. Furthermore, it is also an important background reduction tool for the detection of the DSNB. In Chapter 6, the detection potential for the DSNB will be analysed. Therefore, the energy spectrum of the DSNB and the relevant backgrounds were simulated, and possible methods to suppress these backgrounds were studied.

1.1 Vacuum Neutrino Oscillations

According to the standard model of particle phyiscs (SM), the neutrino is massless and only interacts weakly. There a three different neutrino flavours (ν_{e}, ν_μ, ν_τ), corresponding to the charged leptons and the lepton flavour number is conserved [3]. But there are several evidences from atmospheric [4], solar [5] and reactor neutrino experiments [6], that neutrinos can oscillate between different flavour eigenstates.
The weak flavour eigenstates of the neutrino (ν_e, ν_μ, ν_τ) can be expressed as linear superpositions of orthogonal neutrino mass eigenstates (ν_1, ν_2, ν_3) [7]:

$$\begin{pmatrix} \nu_e \\ \nu_\mu \\ \nu_\tau \end{pmatrix} = U \begin{pmatrix} \nu_1 \\ \nu_2 \\ \nu_3 \end{pmatrix} \tag{1.1}$$

where U is the unitary Pontecorvo-Maki-Nakagawa-Sakata (PMNS) matrix. It can be parameterized with three rotation angles θ_{ij} and one CP violating phase δ [8]:

$$U = \begin{pmatrix} 1 & 0 & 0 \\ 0 & c_{23} & s_{23} \\ 0 & -s_{23} & c_{23} \end{pmatrix} \begin{pmatrix} c_{13} & 0 & s_{13}e^{-i\delta} \\ 0 & 1 & 0 \\ -s_{13}e^{-i\delta} & 0 & c_{13} \end{pmatrix} \begin{pmatrix} c_{12} & s_{12} & 0 \\ -s_{12} & c_{12} & 0 \\ 0 & 0 & 1 \end{pmatrix} \tag{1.2}$$

In this parameterization s_{ij} and c_{ij} are abbreviations of $\sin(\theta_{ij})$ and $\cos(\theta_{ij})$. If neutrinos are Majorana particles, two additional CP violating phases are introduced. These Majorana CP violating phases are omitted in the following discussion, as they do not affect the oscillation probability [9].

In the following, the plane wave approach was used. For a derivation using the wave packet and the quantum field theory approach, see [10]. The time evolution of the neutrino mass eigenstates is given by the Schrödinger equation[1] [9]:

$$|\nu_i(t)\rangle = e^{-iE_i t}|\nu_i(0)\rangle \ , \tag{1.3}$$

where $\mathrm{E_i}$ is the energy of the mass eigenstate ν_i.
Assuming that the neutrino has a finite but small mass, such that $\mathrm{m_i} \ll \mathrm{p_i}$ and $\mathrm{p_i} \approx \mathrm{E}$, the neutrino energy $\mathrm{E_i}$ can be written as:

$$\mathrm{E_i} = \sqrt{\mathrm{p_i^2 + m_i^2}} \simeq \mathrm{p_i} + \frac{\mathrm{m_i^2}}{2\mathrm{p_i}} \simeq \mathrm{E} + \frac{\mathrm{m_i^2}}{2\mathrm{E}} \tag{1.4}$$

From equations (1.1)-(1.4) it follows that the probability $\mathrm{P}_{\alpha\to\beta}$ to detect a neutrino which was produced in the flavour eigenstate α in the flavour eigenstate β is:

$$\mathrm{P}_{\alpha\to\beta} = \left|\langle\nu_\beta|\nu_\alpha(\mathrm{t})\rangle\right|^2, \text{ with } |\nu_\alpha\rangle = \sum_{\mathrm{i}} \mathrm{U}_{\alpha\mathrm{i}}|\nu_i(t)\rangle \tag{1.5}$$

$$\mathrm{P}_{\alpha\to\beta} = \left|\sum_{\mathrm{i}} \mathrm{U}^*_{\alpha\mathrm{i}}\mathrm{U}_{\beta\mathrm{i}}\mathrm{e}^{-\frac{\mathrm{m_i^2 t}}{2\mathrm{E}}}\right|^2 \tag{1.6}$$

The survival probability to detect a neutrino which was produced in the flavour eigenstate α in the flavour eigenstate α is:

$$\mathrm{P}_{\alpha\to\alpha} = \left|\sum_{\mathrm{i}} \mathrm{U}^*_{\alpha\mathrm{i}}\mathrm{U}_{\alpha\mathrm{i}}\mathrm{e}^{-\frac{\mathrm{m_i^2 t}}{2\mathrm{E}}}\right|^2 = \left|\sum_{\mathrm{i}} |\mathrm{U}_{\alpha\mathrm{i}}|^2\,\mathrm{e}^{-\frac{\mathrm{m_i^2 t}}{2\mathrm{E}}}\right|^2 \tag{1.7}$$

As θ_{13} is small compared to the other mixing angles and as $\Delta m^2_{13} \gg \Delta m^2_{12}$ (see Table 1.1), it is often possible to make the approximation of only two neutrino flavours. In this case, equation (1.6) simplifies to:

$$\mathrm{P}_{\alpha\to\beta} = \sin^2(2\theta)\sin^2\left(\frac{\mathrm{m_2^2} - \mathrm{m_1^2}}{4\mathrm{E}}\mathrm{L}\right) \tag{1.8}$$

Thus, the neutrino only oscillates if the masses $\mathrm{m_i}$ of the mass eigenstates are not equal and if $\theta > 0$, which implies that U is not diagonal. Consequently, the lepton flavour number is not conserved in the case of neutrino oscillations and at least two neutrino mass eigenstates are not massless, contrary to the prediction of the SM.
Up to now, the mixing angles θ_{12}, θ_{13} and θ_{23} and the mass square differences $\Delta\mathrm{m^2_{12}}$ and $|\Delta\mathrm{m^2_{23}}|$ were measured in several experiments (see Table 1.1). The sign

[1] In the following $\hbar = c = 1$

Δm^2_{12}	$= (7.50 \pm 0.20) \cdot 10^{-5} \mathrm{eV}^2$
$\lvert\Delta m^2_{23}\rvert$	$= \left(2.32^{+0.12}_{-0.08}\right) \cdot 10^{-3} \mathrm{eV}^2$
$\sin^2(2\theta_{12})$	$= 0.857 \pm 0.024$
$\sin^2(2\theta_{23})$	> 0.95
$\sin^2(2\theta_{13})$	$= 0.098 \pm 0.013$

Table 1.1: Neutrino square mass differences and mixing angles [9].

of Δm^2_{12} is known from solar neutrino experiments [5, 11] (see Section 1.2), while the sign of Δm^2_{23} is still unknown. Therefore, there are two possible hierachies of the neutrino mass eigenvalues, the normal ($m_3 > m_2 > m_1$) (NH) and the inverted hierachy ($m_2 > m_1 > m_3$) (IH).
Furthermore, the value of the CP violating phase δ is not known. As the imaginary phase δ does not affect the survival probablity (see equation 1.7), it can not be measured in dissapearance experiments, like reactor neutrino experiments. A measurement in a neutrino beam appearance experiment is possible, but challenging (see section 2.2.6 for details).

1.2 Neutrino Oscillations in Matter

In normal matter, muon and tau neutrinos can only scatter elastically by neutral current (NC) reactions, while electron neutrinos can also scatter elastically off electrons by charged current (CC) reactions. Thus, electron neutrinos have a larger cross section. This enlarged cross section leads to an additional potential $V = \sqrt{2} G_F n_e(\vec{x})$ for electron neutrinos, where G_F is the Fermi coupling constant and $n_e(\vec{x})$ is the electron density. This potential can be interpreted as an addition to the mass terms of the Hamiltonian, which describes the propagation of the neutrino mass eigenstates. Thus, the mixing angles and the mass differences are changed compared to the vacuum case. The third matter eigenstate ν_{3m} essentially decouples from the first two matter eigenstates and is almost not affected by solar or Earth matter ($\nu_{3m} \simeq \nu_3$)[1]. Thus, the electron neutrino survival probability can be approximated by the following expression [12]:

$$P_{ee} = c^4_{13} P_{2f}\left(\theta_{12}, \Delta m^2_{12}, c^2_{13} V\right) + s^4_{13} \ , \tag{1.9}$$

where P_{2f} is the electron neutrino survival probability for the two flavour case and an effective potential $c^2_{13}V$.
In the two flavour scenario, the mixing angle in matter is [13]:

[1] This approximation is not valid anymore in a core-collapse supernova, due to the high density.

$$\cos(2\theta_{12,\mathrm{m}})\,(\mathrm{V}) = \frac{\cos 2\theta_{12} - 2\mathrm{EV}/\Delta\mathrm{m}^2_{12}}{\sqrt{\left(\cos 2\theta_{12} - 2\mathrm{EV}/\Delta\mathrm{m}^2_{12}\right)^2 + \sin^2 2\theta_{12}}}\ , \tag{1.10}$$

where E is the neutrino energy. From equation (1.10) one can see that there are three special cases:

- $2\mathrm{EV}/\Delta\mathrm{m}^2_{12} \ll \cos 2\theta_{12} \Rightarrow \cos 2\theta_{12,\mathrm{m}} \simeq \cos 2\theta_{12}$: The mixing angle is almost unaffected by the matter (vacuum region).
- $2\mathrm{EV}/\Delta\mathrm{m}^2_{12} \simeq \cos 2\theta_{12} \Rightarrow \theta_{12,\mathrm{m}} \simeq 45°$: The mixing between the two neutrino flavours is maximal, independent of the value of θ_{12} (transition region).
- $2\mathrm{EV}/\Delta\mathrm{m}^2_{12} \gg \cos 2\theta_{12} \Rightarrow \theta_{12,\mathrm{m}} \simeq 90°$: Almost no mixing occurs (matter dominated region). In this case, an electron neutrino mainly consists of the matter eigenstate $\nu_{2\mathrm{m}}$.

In the sun, the last condition applies to electron neutrinos that are produced in the center at energies above $\sim 10\,\mathrm{MeV}$. When these neutrinos propagate through the sun, the electron density decreases, thus changing the mixing angle $\theta_{12,\mathrm{m}}$. As the density gradient is small in comparison to the oscillation length, an adiabatic conversion occurs and the neutrinos stay in the mass eigenstate $\nu_{2\mathrm{m}}$[2]. The resonant conversion of ν_e into ν_2 is referred to as the Mikheev-Smirnov-Wolfenstein (MSW) effect [7]. It is is only possible if $\mathrm{m}_{\nu_2} > \mathrm{m}_{\nu_1}$ and thus the sign of $\Delta\mathrm{m}^2_{12}$ is positiv. As the neutrinos are in the mass eigenstate $\nu_{2\mathrm{m}}$, they do not oscillate on the way to the earth, and the probability to detect them as electron neutrinos is[3]:

$$\mathrm{P}_{\mathrm{ee}} = \left|\langle\nu_{2\mathrm{m}}|\nu_\mathrm{e}\rangle\right|^2 \cong \sin^2(\theta_{12}) \cong 30\% \tag{1.11}$$

Averaging over all production points, the 2-flavour electron neutrino survival probability in the sun is [12]:

$$\mathrm{P}_{2\mathrm{f}} = \frac{1}{2}\left[1 + \cos 2\theta_{12}\langle\cos 2\theta_{12\mathrm{m}}\rangle\right]\ , \tag{1.12}$$

where $\langle\cos(2\theta_{12,\mathrm{m}})\rangle$ is the value of $\cos(2\theta_{12,\mathrm{m}})$ averaged over all neutrino production points:

[2]The probability for a non adiabatic transition between $\nu_{2\mathrm{m}}$ and $\nu_{1\mathrm{m}}$ is $\mathrm{P_c} = 10^{-9} - 10^{-7}\left(\frac{\mathrm{E}}{\mathrm{MeV}}\right)^2$ [13] and is thus neglected in the following discussion.

[3]The possible transition of $\nu_{2\mathrm{m}} \to \nu_{1\mathrm{m}}$, when the neutrino traverses the earth, the so-called earth-matter-effect, is neglected in the following discussion as it only changes $\mathrm{P_{ee}}$ by about 1-2 % [12].

$$\langle \cos(2\theta_{12\mathrm{m}}) \rangle = \int_0^{\mathrm{R}_\odot} \mathrm{dr}\, \mathrm{f(r)}\, \cos 2\theta_{12\mathrm{m}}(\mathrm{r}) \tag{1.13}$$

Here, $\mathrm{R}_\odot$ is the radius of the sun and f(r) is the normalized spatial distribution function of the neutrino source [14]. As $\langle \cos(2\theta_{12,\mathrm{m}}) \rangle$ depends on the neutrino energy, the survival probability is also energy dependent.
Figure 1.1 shows the predicted survival probability for solar neutrinos, the so-called MSW-LMA solution[4] and the results of several measurements.

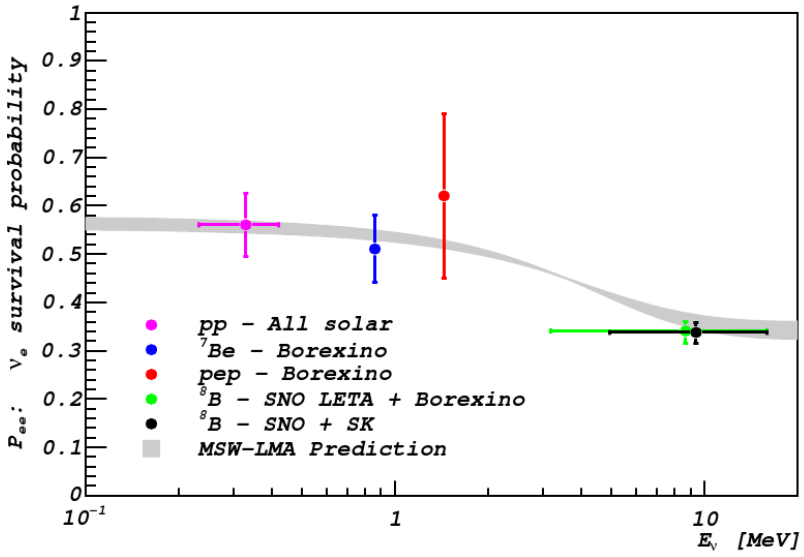

Figure 1.1: The energy dependent survival probability of ν_e from the sun [17]. The grey band shows the predicted survival probability ($1\,\sigma$) according to the MSW-LMA solution. Additionally, the measurements from Borexino (^{7}Be, pep, ^{8}B), SNO(^{8}B), and the results of a combined analysis of all solar neutrino experiments (pp) are shown.

While, $\mathrm{P_{ee}}$ has been measured in the vacuum and the matter dominated region, a precise measurement in the transition region between 2 MeV and 5 MeV is still missing. A measurement in this region is very important, as new physics could influence $\mathrm{P_{ee}}$ in the transition region.
For example, non-standard neutrino interactions could change $\mathrm{P_{ee}}$ in this region. In a simple general model for non-standard neutrino interactions, the fermi cou-

[4] In the 1990's, there were several different combinations of $\Delta\mathrm{m}^2_{12}$ and θ_{12} possible [15]. The large mixing angle (LMA) solution (see Table 1.1) is the only one of those which is consistent with the KamLAND measurement if CPT invariance is assumed [6]. Recently, the Borexino experiment was also able to confirm the LMA solution without assuming CPT invariance [16].

pling constant is replaced by $A_{MSW}G_F$ [18], where $A_{MSW} = 1$ refers to the standard model case. If $A_{MSW} < 1$, the matter effect is weakened and for $A_{MSW} > 1$ it is strengthened. Hence, the survival probability in the transition regions is either reduced ($A_{MSW} > 1$) or enhanced ($A_{MSW} < 1$) compared to the MSW-LMA prediction. Using the currently available solar neutrino data, A_{MSW} was measured to:

$$A_{MSW} = 1.47^{-0.42}_{+0.54} \, , \tag{1.14}$$

which is consistent with the SM. In case that the upturn of ^{8}B spectrum at low energies is detected with $3\,\sigma$ significance, the upper bound on A_{MSW} could be improved from 2.01 to 1.79 ($1\,\sigma$) [18].
Furthermore, light sterile neutrinos[5] ($m_{\nu_1} < m_{\nu_0} < m_{\nu_2}$, where the sterile neutrino ν_s is mainly present in the mass eigenstate ν_0) could reduce the electron neutrino survival probability [19]. In case that the mixing angle α between the mass eigenstates ν_0 and ν_1 is small, the electron neutrino survival probability in the matter and vacuum dominated region would remain almost unchanged compared to the MSW-LMA prediction. But in the transition region, the mixing angle α_m is enlarged and a resonant conversion of electron neutrinos to sterile neutrinos becomes possible. Hence, even for small mixing angles α like $\sin^2 2\alpha = 1 \cdot 10^{-3}$, P_{ee} is significantly reduced compared to the MSW-LMA prediction, so that the upturn of the ^{8}B spectrum is no longer present in the transition region [19].

1.3 Solar Neutrinos

In the sun, energy is produced by the fusion of hydrogen to helium. There are two different fusion mechanisms. In the pp-chain [20] (see Figure 1.2), hydrogen is fused directly to helium in several steps, while in the CNO-cycle [21] (see Figure 1.3), carbon, nitrogen and oxygen serve as catalysers.
The net reaction in both cases is:

$$4p \rightarrow {}^4He + 2e^+ + 2\nu_e, \; Q = 26.73\,MeV \; . \tag{1.15}$$

Due to the higher Coloumb barrier, the CNO-cycle is more sensitive to the core temperatur. In our sun, only $\simeq 1.5\,\%$ of the energy is produced by the CNO-cycle [22]. But in heavier stars with a larger core temperature, the CNO-cycle is dominating.
Figure 1.4 shows the neutrino spectrum, calculated according to the standard solar model (SSM). The dominant neutrino source is the pp reaction. As the pp reaction stands at the beginning of the pp-chain, it is directly connected to the luminosity of the sun and thus the pp neutrino flux is very well known. The theoretical

[5] Neutrinos that do not interact weakly.

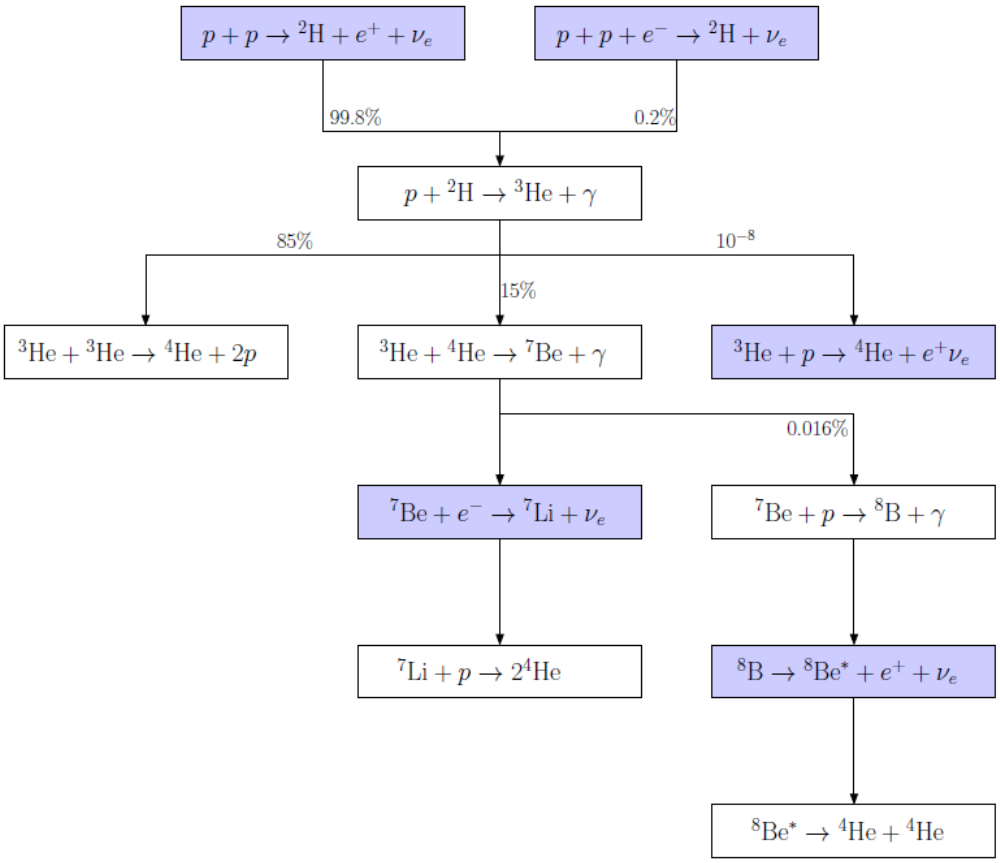

Figure 1.2: The sub reactions of the pp-chain [20]. There are five reactions that generate neutrinos. The neutrinos from the pp, ^{8}B and hep reactions have a continious energy spectrum, while the neutrinos from the ^{7}Be and pep reactions are monoenergetic, due to the kinematics of the reaction.

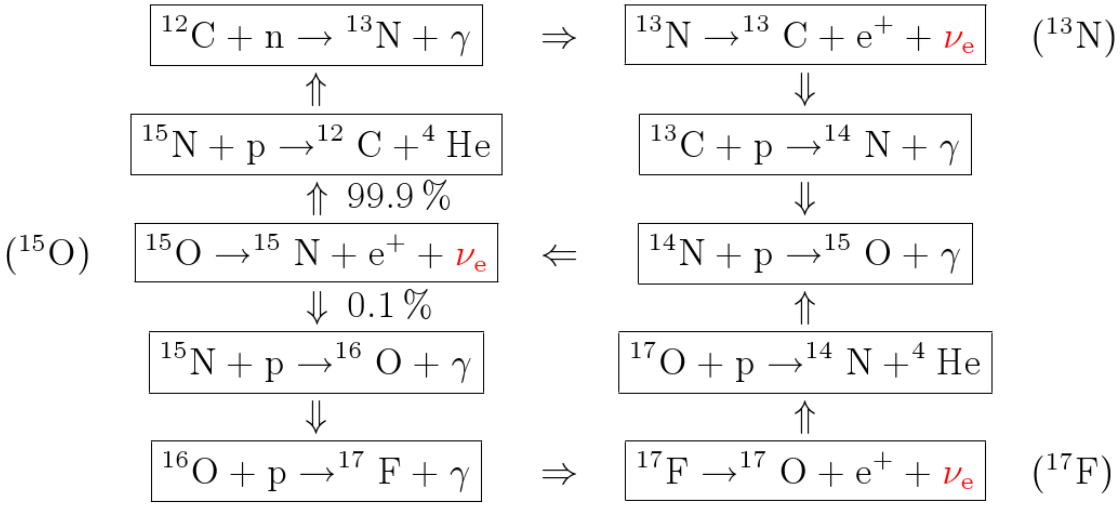

Figure 1.3: The CNO-cycle[21]. There are three neutrino generating reactions with a continious energy spectrum: ^{13}N ,^{15}O and ^{17}F.

prediction for the branching ratio of the pp and pep reaction is very precise and thus the uncertainty of the pep flux is very small. For the other neutrino fluxes, the theoretical uncertainties are larger, due to the uncertainties of the fusion reaction cross sections and of the element abundances in the sun [23].
There are two conflicting measurements of the metallicity Z (abundance of elements that are heavier than helium), resulting in a low metallicity (AGS) [25] and a high metallicity (GS) standard solar model [26]. The ^{7}Be, ^{8}B and CNO flux are sensitive to the metallicity. But at the moment, the theoretical uncertainties of the ^{7}Be and ^{8}B are too large to distinguish between the two models. As the CNO flux depends strongly on the metallicity, a measurement of it could rule out one of the two models, in spite of the theoretical flux uncertainties. Unfortunately, while the ^{7}Be [27] and the ^{8}B [28, 29] flux have been precisely measured, only upper limits on the CNO flux exists [17].

1.4 The Diffuse Supernova Neutrino Background

In a core-collapse supernova, $\sim 10^{58}$ neutrinos and antineutrinos are released in about 10 s [30]. Despite this large flux, only supernovae in the milky way and its satellite galaxies, which occur less than 3 times per century [31], can be detected with the current neutrino detectors. However, the cumulative emission of all core-collapse supernovae throughout the universe have created the so-called Diffuse

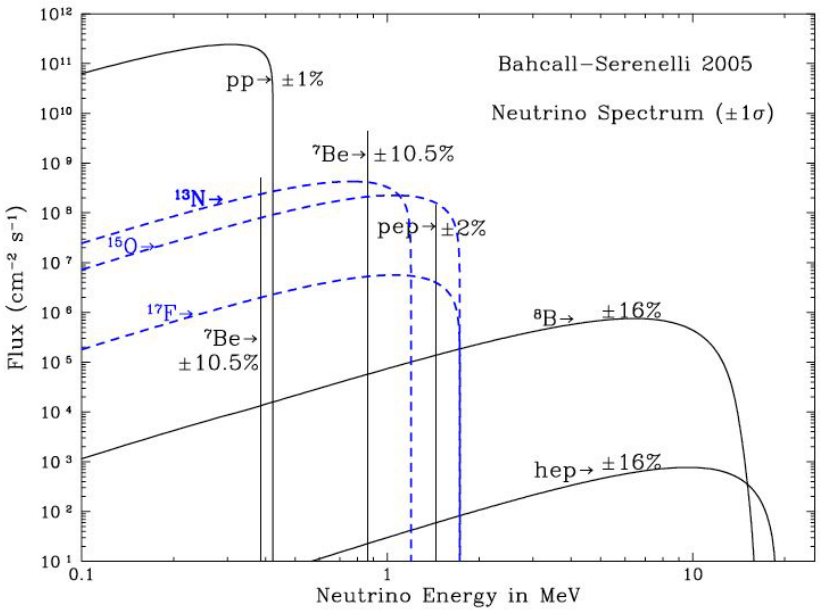

Figure 1.4: Neutrino spectrum calculated according to the SSM [24]. The neutrino fluxes resulting from the pp-chain reactions are plotted as black solid lines, the fluxes from the CNO-cycle reactions as dashed blue lines.

Supernova Neutrino Background (DSNB).

The flux of the DSNB is given by [32]:

$$\frac{dF_\nu}{dE_\nu} = \frac{c}{H_0}\int_0^{z_{max}} R_{SN}(z)\frac{dN_\nu(E'_\nu)}{dE'_\nu}\frac{dz}{\sqrt{\Omega_m\,(1+z)^3+\Omega_\Lambda}}\,, \tag{1.16}$$

where $R_{SN}(z)$ is the supernova rate at redshift z, $E' = E(1+z)$ is the redshift corrected energy of the neutrinos, $\frac{dN_\nu(E_\nu)}{dE_\nu}$ is the number spectrum of the neutrinos emitted by one supernova explosion, H_0 is the hubble constant, c is the speed of light, Ω_m is the cosmic matter density, Ω_Λ is the cosmic constant and $z_{max} = 5$ is the redshift, where the first core-collapse supernova occurred. The factor $1/H_0\sqrt{\Omega_m\,(1+z)^3+\Omega_\Lambda}$ in equation (1.16) takes the expansion of the universe into account.

Assuming that every star above ∼8 solar masses ($M_\odot$) ends in a core-collapse

supernova, $R_{SN}(z)$ can be derived from the star formation rate $R_*(z)$[6] [32]:

$$R_{SN}(z) = \frac{\int_{8M_\odot}^{125M_\odot} \Psi(M)dM}{\int_{0M_\odot}^{125M_\odot} \Psi(M)dM} R_*(z) = 0.0122 M_\odot^{-1} R_*(z) \ , \tag{1.17}$$

where $\Psi(M) = dN/dM$ is the Salpeter initial mass function (IMF) [33] of the stars in the universe.
The star formation rate can be parametrized by the following function [32]:

$$R_*(z) = 0.32 f_{SN} \frac{H_0}{70\,\mathrm{kms^{-1}Mpc^{-1}}} \frac{e^{3.4z}}{e^{3.8z}+45} \frac{\sqrt{\Omega_m (1+z)^3 + \Omega_\Lambda}}{(1+z)^{3/2}} \mathrm{yr^{-1}Mpc^{-3}} \ , \tag{1.18}$$

where $f_{SN} = 1.5 \pm 0.3$ [30] is a normalization factor.
The neutrino emission spectrum can be approximated by a Maxwell-Boltzmann spectrum [2]:

$$\frac{dN_\nu(E_\nu)}{dE_\nu} = \frac{27}{2} \frac{L_\nu}{\langle E_\nu \rangle^2} \left(\frac{E}{\langle E_\nu \rangle} \right)^2 e^{-\frac{3E}{\langle E_\nu \rangle}} \ , \tag{1.19}$$

where $L_\nu = 3 \cdot 10^{53}\,\mathrm{erg}$ is the neutrino luminosity and $\langle E_\nu \rangle$ is the mean neutrino energy. Indirect constraints from the chemical abundances of neutrino induced elements predict $\langle E_\nu \rangle = 12 - 21\,\mathrm{MeV}$ [34]. Assuming that E_ν is independent of the neutrino flavour, this range is in agreement with the measured neutrino spectrum from the supernova 1987A [35]. Numerical supernova simulations also predict $\langle E_{\bar{\nu}_e} \rangle$ to be in the same energy range [36, 37, 38].
Up to now, the DSNB was not measured. The best limit comes from the Super-Kamiokande experiment (see Section 1.5.1), which sets an upper limit (90% C.L.) on the flux of $3.1\,\bar{\nu}_e\,\mathrm{cm^{-2}s^{-1}}$ for $E_{\bar{\nu}_e} > 17.3\,\mathrm{MeV}$ [39], which is about a factor of two above the predicted value from [30] for $\langle E_{\bar{\nu}_e} \rangle = 18\,\mathrm{MeV}$.

1.5 Real-time Neutrino Detectors

The detection of solar neutrinos in the Homestake experiment by Raymond Davis in the 1970s was the first detection of a natural neutrino source [40]. The detection reaction was

$$\nu_e + {}^{37}\mathrm{Cl} \rightarrow {}^{37}\mathrm{Ar} + e^- \ , \tag{1.20}$$

[6] The redshift dependent supernova rate is usually derived from the star formation rate, as the measurements of the star formation rate are more precise.

where the produced ^{37}Ar was extracted and its decays were counted. Thus, only the integrated rate above the energy threshold could be measured. Furthermore, this experiment was only sensitive to electron neutrinos.
Contrary to the radiochemical experiments, Water-Čerenkov detectors (WCDs) and liquid-scintillator detectors (LSDs) can also measure the deposited energy of a neutrino event in real-time. WCDs also have the advantage that they reconstruct the direction of an event, but due to low light yield they are only sensitive to ^{8}B solar neutrinos [11]. LSDs have a higher light yield and thus a lower threshold, so that they can also measure the low energetic ^{7}Be solar neutrinos [27].
In the following sections, Super-Kamiokande and SNO are described as examples for WCDs and Borexino as an example for a LSD.

1.5.1 Super-Kamiokande

Super-Kamiokande is a 50 kt Water-Čerenkov detector, that is located at the Kamioka Observatory in Japan [41]. It is covered by 1000 m of rock (2700 meter water equivalent (m w.e.)) to shield cosmic muons. The fiducial volume of the detector is 22.5 kt.
The detection reaction for low energy neutrinos ($E < 100\,\mathrm{MeV}$) is the elastic neutrino electron scattering reaction (ES):

$$\nu_x + e^- \rightarrow \nu_x + e^- \ . \tag{1.21}$$

The cross section for electron neutrinos is about 6 times higher than for muon and tau neutrinos, as they can interact via the CC and NC channel [42]. As the scattered neutrino can not be detected, the neutrino energy can not be reconstructed on an event by event basis, but only through a statistical analysis of several events.
If the scattered electron moves faster than the phase speed of light in water, it emits so-called Čerenkov light. Due to the constructive interference of spherical light waves emitted along the particle track, a conical light front is generated analogously to a supersonic mach cone [43]. The opening angle α of the cone depends on the velocity $\beta = \frac{v}{c}$ of the electron and on the refractive index n_w in water:

$$\cos\alpha = \frac{1}{\beta n_w} \ . \tag{1.22}$$

As the electron has to move faster than the phase speed of light in water to emit Čerenkov light, the Čerenkov threshold for electrons in water is

$$E_t = \frac{1}{\sqrt{1 - n_w^{-2}}} m_e \approx 800\,\mathrm{keV} \ . \tag{1.23}$$

In Super-Kamiokande, the emitted light is detected by 11000 20-inch Photomultiplier tubes (PMTs). Due to the characteristic shape of the Čerenkov cone, the

direction of the electron can be reconstructed. The Čerenkov light yield amounts to about 200 photons per MeV [44], but due to the limited quantum efficiency of the PMTs and the 40 % optical coverage, only a small fraction of the emitted photons are detected. Furthermore, PMT dark noise limits the current detector threshold for electrons to $E_{kin} = 4.0\,MeV$[7].
Thus, Super-Kamiokande is not sensitive to ^{7}Be and pep solar neutrinos. In Phase III, which includes 548 days live time and had a energy threshold of 4.5 MeV, the ^{8}B flux was measured to [41]

$$\Phi_{^8B} = (2.32 \pm 0.04(\text{stat.}) \pm 0.05(\text{syst.})) \cdot 10^6 \text{cm}^{-2}\text{s}^{-1} \ , \tag{1.24}$$

which is less than 50 % of the expectation from the SSM, as electron neutrinos can oscillate into muon and tau neutrinos (see Section 1.2), which have a lower cross section for the ES reaction. This result is in agreement with the prediction of the MSW-LMA solution, but a spectral analysis of the recent Phase IV data favors a flat electron neutrino survival probability above 4.5 MeV compared to the MSW-LMA prediction at a level of $1.1 \sim 1.9\,\sigma$ [45] (see Figure 4.3 for a comparison between the flat P_{ee} model and the MSW-LMA prediction).
Super-Kamiokande is also sensitive to the Diffuse Supernova Neutrino Background (see Section 1.4). The antielectron neutrinos can be detected with the inverse beta decay reaction, which has a larger cross section than the ES reaction:

$$\bar{\nu}_e + p \rightarrow e^+ + n \ . \tag{1.25}$$

As the neutron is much heavier than the positron, the positron gets almost all the energy of the $\bar{\nu}_e$, but reduced by ~ 1.8 MeV, due to the Q-Value of reaction (1.25). Thus, the neutrino energy can be reconstructed from the prompt positron signal. The neutron is captured by a free proton with a mean capture time of ~ 0.2 ms, producing a 2.2 MeV gamma. Hence, it is in principle possible to use this delayed coincidence to suppress the background, but due to the high threshold this is not possible in Superkamiokande[8].
Cosmogenic radioisotopes, which are produced by cosmic muons, limit the detection threshold to 17.3 MeV. Further backgrounds from atmospheric neutrinos, solar neutrinos and the decays of invisible muons limit the detection efficiency. Thus, the DSNB could not be detected, but Super-Kamiokande has determined the best current upper limit on the flux with $3.1\,\bar{\nu}_e\text{cm}^{-2}\text{s}^{-1}$ (90 % C.L.) for $E_{\bar{\nu}_e} > 17.3$ MeV [39], which is a factor of 2-4 above the theoretical predictions.

[7] Due to changes in the electronics and number of active PMTs, the detector threshold varied from 4.0 MeV to 6.5 MeV over the lifetime of the experiment.

[8] There are plans to dissolve Gadolinium into water, which would increase the energy of the gammas from the neutron capture to ~ 8 MeV, so that the neutron capture can be detected [30].

1.5.2 SNO

The solar neutrino experiment SNO (Sudbury Neutrino Observatory) was a Water-Čerenkov detector that used 1 kt heavy water (D_2O) as a target [46]. It was covered by 1.8 km of rock (5.9 km w.e) to shield cosmic muons. The detector threshold for electrons was $E_{kin} = 3.5\,\text{MeV}$. Compared to Super-Kamiokande, it had two additional detection channels for solar neutrinos, because heavy water was used as target material [46]. One CC channel which is only sensitive to electron neutrinos and one NC channel that has the same cross section for all neutrino flavours:

$$\text{CC}: \qquad \nu_e + d \rightarrow e^- + 2p \tag{1.26}$$

$$\text{NC}: \qquad \nu + d \rightarrow \nu + n + p \tag{1.27}$$

In the CC channel, the electron was detected directly by its Čerenkov light, as it was done in the ES channel. The ES and CC events were separated statistically by a spectral fit. As the neutron that is produced in the NC reaction does not produce Čerenkov light, it could not be detected directly. But when it is captured on deuterium, it emits a 6.25 MeV gamma, that is subsequently detected[9]. With the NC channel, it is possible to measure the ^{8}B flux directly, without taking neutrino oscillation into account [46]:

$$\Phi_{NC} = \left(5.14 \pm 0.16(\text{stat.})^{+0.13}_{-0.12}(\text{syst.})\right) \cdot 10^6 \text{cm}^{-2}\text{s}^{-1} \ , \tag{1.28}$$

which is in agreement with the predictions from the SSM. Furthermore, the electron neutrino survival probability can be determined by measuring the flux with the CC channel [28]:

$$\Phi_{CC} = \left(1.67^{+0.05}_{-0.04}(\text{stat.})^{+0.07}_{-0.08}(\text{syst.})\right) \cdot 10^6 \text{cm}^{-2}\text{s}^{-1} \ , \tag{1.29}$$

and comparing it with the results from the CC channel. The resulting electron neutrino survival probability is:

$$P_{ee} = \frac{\Phi_{CC}}{\Phi_{NC}} = 0.301 \pm 0.033 \ , \tag{1.30}$$

which is in agreement with the MSW-LMA prediction. Furthermore, the spectral shape of P_{ee} was also measured, but due to the low statistics and the large systematic errors below 5 MeV, it was not possible to distinguish between the MSW-LMA prediction and the hypothesis that P_{ee} is constant [46].

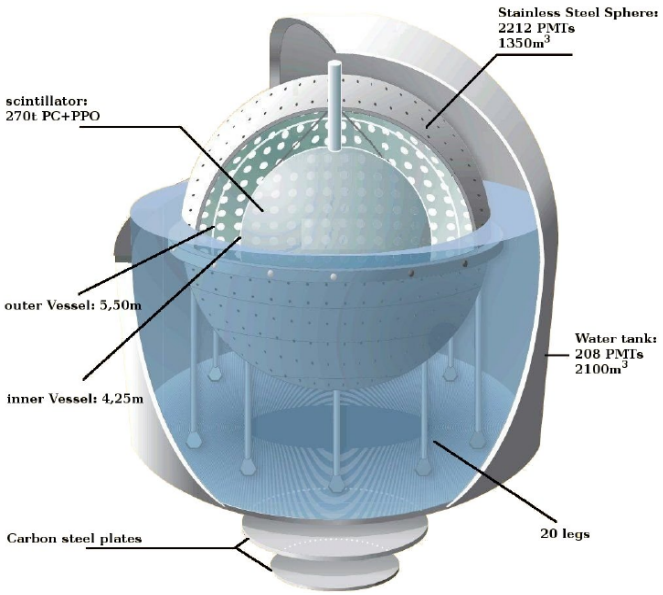

Figure 1.5: Schematical view of the Borexino detector [47]. It consist of 278 t liquid scintillator in the inner Vessel, that is shielded by several layers of buffer liquid and water. The scintillation light is detected by 2212 8-inch PMTs.

1.5.3 Borexino

Borexino is a liquid scintillator detector that is located at the underground Laboratori Nazionali del Gran Sasso (LNGS) at a depth of 3800 meter water equivalent. Its target consist of 278 t pseudocumene (PC, 1,2,4-Trymethylbenze), that is doped with 1.5 g/l of 2,5-diphenyloxazole (PPO), the so-called wavelength shifter. The scintillator is contained in a 125 μm thin nylon vessel with a radius of 4.25 m, the so-called inner Vessel (IV) (see Figure 1.5) [29].
When a charged particles traverses the scintillator, it excites the weakly bound electrons in the π-orbitals of the benzene ring at the base of the PC molecule. The excited PC molecule can subsequently transfer its energy non-radiatively to a PPO molecule. Finally, a photon is emitted that has a larger wavelength than a photon that would be emitted directly by the PC molecule. Thus, it can not be absorbed by a PC molecule[10] and the scintillator becomes transparent [48]. The addition

[9] In Phase II, 2 tons of NaCl were dissolved in the water, so that the neutron could also be captured on ^{35}Cl, which has a larger capture cross sections, releases more energy (8.6 MeV) and emits multiple gammas [46]. In Phase III, neutrons could also be detected by an array of ^{3}He proportional counters [28].

[10] Photons that are directly emitted by a PC molecule can be absorbed because the emission and absorption bands of the PC molecule overlap.

of the wavelength shifter PPO has the additional advantage, that the photons are shifted to a region where common PMTs are more efficient.
The IV is contained in the so-called outer Vessel (OV), that is filled with a buffer liquid to shield the target volume from external gamma rays. It consists of PC, doped with 3g/l DMP (dimethylphthalate), which reduces the light yield. The OV itself is contained in a Stainless Steel Sphere (SSS) with a diameter of 13.7 m, that is filled with buffer liquid. The scintillation light is detected by 2212 8-inch Photomulitplier, that are mounted to the SSS. The SSS is placed in a steel dome with 18 m diameter and 16.9 m height, that is filled with deionized water and shields the detector from fast neutrons that are produced in the surrounding rock. Furthermore, it serves as a Water-Čerenkov muon veto.
Compared to a Water-Čerenkov detector, the advantage of a liquid scintillator detector is that the light yield is with about 10^4 photons per MeV much higher. Thus, Borexino has a detector threshold below 200 keV, so that it is also sensitive to the lower energetic part of the solar neutrino spectrum (pp, ^{7}Be, pep and CNO). Furthermore, the energy resolution is also much better.

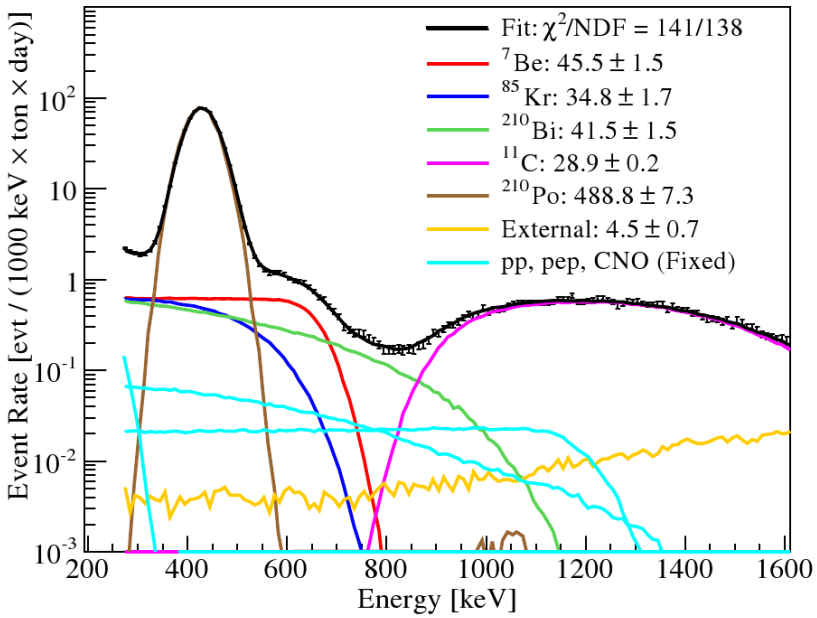

Figure 1.6: A Monte Carlo based fit to the low energy spectrum (270 keV-1.6 MeV) in Borexino, including all known background sources [27].

Due to the unprecedentedly low radioactive background level (see Figure 1.6), Borexino could perform the first real time measurement of ^{7}Be neutrinos in 2007 [49]. Following an intensive calibration campaign to reduce the systematic error,

the ^{7}Be rate could be measured with less than 5 % uncertainty in 2011 [27]:

$$\mathrm{R}\left(^7\mathrm{Be}\right) = \left(46.0 \pm 1.5(\mathrm{stat})^{+1.5}_{-1.6}(\mathrm{syst})\right) \frac{\mathrm{counts}}{\mathrm{d} \cdot 100\,\mathrm{t}} \ , \tag{1.31}$$

which corresponds to a ν_e-equivalent ^{7}Be flux of:

$$\Phi_{^7\mathrm{Be}} = (3.10 \pm 0.15) \cdot 10^9 \mathrm{cm}^{-2}\mathrm{s}^{-1} \ . \tag{1.32}$$

Using the SSM prediction for ^{7}Be flux, the electron neutrino survival probability is $\mathrm{P_{ee}} = 0.51 \pm 0.07$ at 862 keV, which confirms the MSW-LMA prediction in the vacuum region.
Borexino is also able to measure the pep solar neutrino flux. The latest result is [17]:

$$\Phi_{\mathrm{pep}} = (1.6 \pm 0.3) \cdot 10^8 \mathrm{cm}^{-2}\mathrm{s}^{-1} \ . \tag{1.33}$$

Due the low flux of CNO neutrinos and the intrinsic ^{210}Bi background, only an upper limit of $\Phi_{\mathrm{cno}} < 7.7 \cdot 10^8 \mathrm{cm}^{-2}\mathrm{s}^{-1}$ (95 % C.L.) could be determined [17]. Up to now, it was not possible to measure the pp flux, due the intrinsic ^{14}C background.
Borexino has also measured the ^{8}B flux, using a unprecedentedly low energy threshold of 3 MeV [29]:

$$\Phi_{^8\mathrm{B}} = (2.4 \pm 0.4 \pm (\mathrm{stat}) \pm 0.1(\mathrm{syst})) \cdot 10^6 \mathrm{cm}^{-2}\mathrm{s}^{-1} \ . \tag{1.34}$$

Due to the low statistics, the predicted upturn of $\mathrm{P_{ee}}$ below ~ 5 MeV could not be detected.
Furthermore, Borexino has also measured the rate of antielectron neutrinos from radioactive beta decays in the earth, the so-called geoneutrinos, to be:

$$\mathrm{S_{geo}} = (38 \pm 12)\,\mathrm{events/year/}10^{32}\mathrm{protons} \ , \tag{1.35}$$

which is consistent with the predictions from different Bulk Silicate Earth (BSE) models [50].

Chapter 2

The LENA Project

The present liquid scintillator detectors (LSDs) like Borexino (278 t target mass) and KamLAND (1 kt target mass) [51] have demonstrated the large potential of this detector technology. Thus, LENA (**L**ow **E**nergy **N**eutrino **A**stronomy) has been proposed as a next-generation 50 kt LSD [2]. Du to its larger target mass, a high statistic measurements of strong astrophysical neutrino sources, like the sun or a core-collapse supernova can be performed. This will improve our understanding of these neutrino sources and also allow a measurement of the neutrino properties itself (see Section 2.2.1 and Section 2.2.2). Furthermore, a precision measurement of geoneutrinos (see Section 2.2.4) and a first detection of the Diffuse Supernova Neutrino Background (see Section 2.2.3) will be possible. In addition, LENA can also be used as a far detector of a long baseline neutrino beam experiment, which can determine the mass hierarchy and search for CP violation in the neutrino sector (see Section 2.2.6).
LENA is currently part of the LAGUNA-LBNO design study, which is funded by the European Union and investigates the construction of a large volume neutrino observatory, that can also be used as a far detector of a long baseline neutrino oscillation experiment (LBNO). This design study will last until the end of 2014. In case of a positive funding decision, the construction could start in 2015 and would take about 9 years, so that the data taking would begin in 2024.

2.1 Detector Setup

Figure 2.1 shows a schematic overview of the current LENA design [52]. The target material will consist of ~ 50 kt of liquid scintillator, that is enclosed in a cylinder with 14 m radius and 98 m height. The liquid scintillator will be a mixture of three components. Linear-alkyl-benze (LAB) will be the solvent, with a small admixture of the wavelength shifters 2,5-diphenyl-oxazole (PPO) as primary fluor and 1,4-

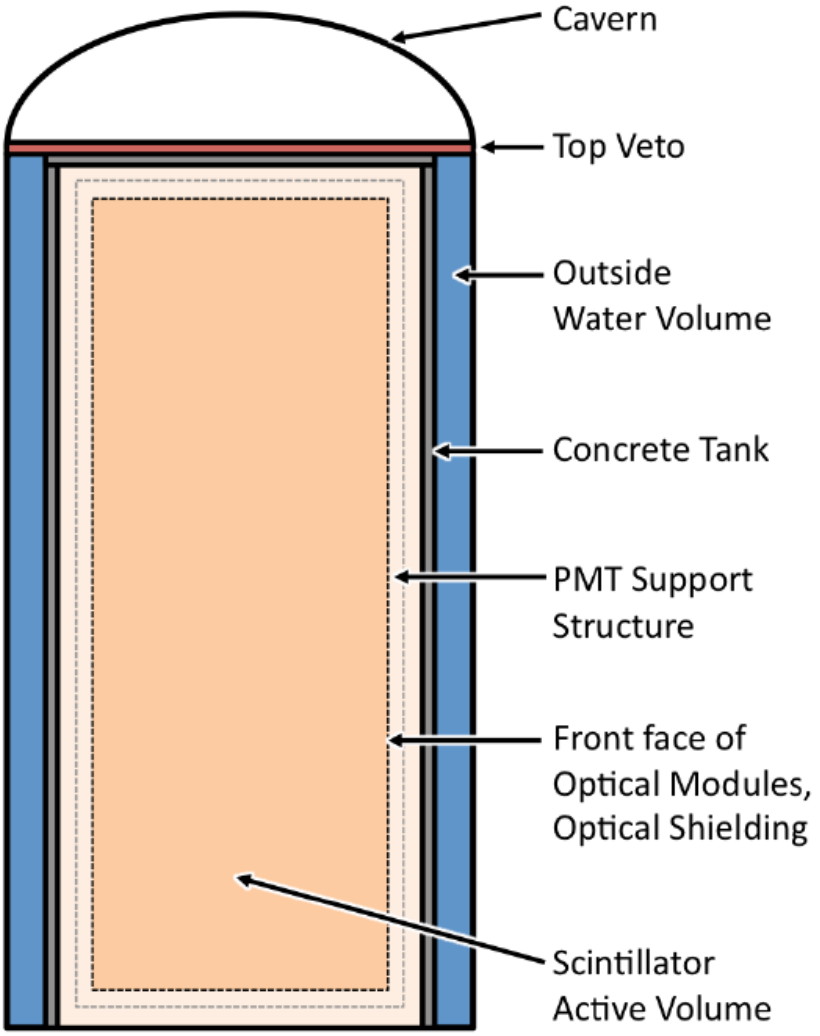

Figure 2.1: Schematical view of the LENA detector [52]. The target volume will consist of $\sim 50\,\mathrm{kt}$ liquid scintillator. The apertures of the optical modules will be positioned at the edge of the target volume. The optical modules will consist of a 8-12 inch PMT and a light concentrator, which will be mounted inside a pressure encapsulation, that is filled with a non-scintillating buffer liquid. An optical shielding will be attached to the PMT support structure, so that no light from the 2 m thick volume behind the PMTs can be detected. The concrete tank will be surrounded by at least 2 m of water, which serves as a passive shielding and as an active Water-Čerenkov muon veto. An additional muon veto will be placed on top of the detector, which could e.g. consists of plastic scintillator panels.

bis-(o-methylstryryl)-benzene (bisMSB) as secondary fluor[1]. These fluors will shift the maximum of the emission spectrum to $\sim 420\,\mathrm{nm}$, where the scintillator is more transparent [48].

The scintillation light will be collected by $\sim 3 \cdot 10^4$ PMTs if 12-inch PMTs will be used, though 8 and 10-inch PMTs are also on option. The PMTs will be mounted to a stainless steel support structure at a radius of 14 m. Non-imaging light concentrators will be attached to the PMTs, which increase the effective optical coverage to $\sim 30\,\%$. Due to the high pressure at the bottom of the tank, the PMTs and light concentrators will be mounted in a pressure encapsulation. This pressure encapsulation will be filled with a non-scintillating buffer liquid to shield the target volume from gamma rays emitted by radioactive impurities in the PMT glass. Apart from that, no buffer liquid will be present between the PMTs and target volume, which puts stringent limits on the radioactivity of the PMT glass and the electronics (see Section 4.2.3 for details). The target volume and PMTs will be inside a cylindrical concrete tank with 16 m radius and 100 m height. A thin optical shield will be placed between the PMTs, to prevent the detection of photons, that were emitted in the space between the target volume and the tank. This volume will be filled with liquid scintillator, to shield the target volume from gamma rays emitted inside the tank. Thin stainless steel sheets will be welded to the tank walls, to prevent a chemical reaction between the liquid scintillator and the concrete.

The space between the tank and the cavern will be filled with clean water, which shields the detector from external radioactivity coming from the rock and from fast neutrons, that are produced by cosmic muons traversing the surrounding rock. To shield the target volume, at least 2 m of water are needed. Additionally, it will serve as an active muon veto. The Čerenkov light from the traversing muons will be detected with 2000 encapsulated 12-inch PMTs, mounted to the outer tank wall. Another benefit of the water is that the forces on the tank generated by the liquid scintillator are partly compensated.

As no water will be on top of the tank, an additional muon veto will be installed on top of the tank. One possible option is to use plastisc scintillator panels, though limited streamer tubes and resistive plate chambers are also considered at the moment. The DAQ system will be installed in an auxiliary cavern close to the top of the detector and the total height of the cavern will be 115 m.

The favored location for the detector is the Pyhäsalmi mine in Finland. It is planned to built the detector at an depth of 1400 m corresponding to 4000 m of water equivalent. This will reduce the cosmic muon flux to $\sim 0.2\,\mathrm{m}^{-2}\mathrm{h}^{-1}$ [53],

[1]The exact amounts of PPO and bisMSB are currently determined in small scale laboratory measurements. At the moment, a PPO concentration of 3 g/l and bisMSB concentration of 20 mg/l is favored.

Source	Event Rate [d^{-1}]
pp	$2.3 \cdot 10^3$
^{7}Be	$1.1 \cdot 10^4$
pep	$8.5 \cdot 10^2$
CNO	$8.8 \cdot 10^2$
^{8}B	$1.3 \cdot 10^2$
hep	0.4

Table 2.1: Expected solar neutrino event rates in LENA for 36 kt fiducial volume and 200 keV detection threshold. The rates were calculated using the low metallicity BS05(AGS,OP) solar standard model [14].

which is about a factor 5 less than in Borexino [29].

2.2 Physics Program

2.2.1 Solar Neutrinos

Compared to the current solar neutrino experiment Borexino, LENA has a bigger target mass and a lower cosmic muon flux, due to the increased shielding. Table 2.1 shows the calculated rates for the different solar neutrinos (see Section 4.1 for details).
Despite the large event rate of the pp neutrinos, a measurement will be very challenging, due to the intrinsic ^{14}C β^- background. ^{14}C has a Q-Value of 156 keV and is thus only a background for the low energy pp neutrinos. Due to the large abundance and the limited energy resolution at these low energies, the ^{14}C rate above 200 keV is expected to be $\sim 1 \cdot 10^3 s^{-1}$, surpassing the pp neutrino signal at 200 keV by several orders of magnitude.
Due to the large ^{7}Be-rate of $1.1 \cdot 10^4\,d^{-1}$, periodic modulations on time scales ranging from a few minutes to more than 10 years will be detectable on a sub-percent level [54]. This will allow to search for temperature and density variations in the inner regions of the sun, the so called helioseismic g-mode oscillations. Furthermore, possible variations of the fusion rate with the solar cycle could be detected.
Due to high statistics, and the lower cosmogenic ^{11}C background, LENA can perform a high precision measurement of the pep flux. As the pep flux has a small theoretical uncertainty ($\sim 1\,\%$ [23]), this will give the possibility to make a stringent test of the MSW-LMA prediction at 1.44 MeV. Furthermore, the CNO flux can be measured for the first time if the ^{210}Bi background is approximately at the

same level as in Borexino. The ^{210}Bi background is crucial, as its spectral shape is very similar to the shape of the CNO spectrum. Thus, Borexino was only able to set an upper limit on the CNO flux ($\Phi_{\mathrm{cno}} < 7.7 \cdot 10^8 \mathrm{cm}^{-2}\mathrm{s}^{-1}$ (95 % C.L.)) [17]. But as ^{210}Bi decays with 5.0 d half life to ^{210}Po, it is possible to determine the ^{210}Bi rate by measuring the ^{210}Po rate, which has a destinctive spectral shape. Furthermore, ^{210}Po is an α-emitter, so that its rate can also be determined by a pulse shape discrimination (see Chapter 5 for details). Of course, this method only works if ^{210}Po and ^{210}Bi are in an secular equilibrium, which is the case once the ^{210}Po rate is stable. As ^{210}Po has a half life of 138 d, this requires that no operations are performed after the filling and calibration which could introduce ^{210}Po into the detector. Once the ^{210}Po rate becomes stable, the ^{210}Bi rate can be subtracted statistically, so that the CNO flux can be measured.
Due to the large target mass, the external gamma background, which prevented the measurement of ^{8}B neutrinos below 3 MeV in Borexino, can be suppressed by using a small fiducial volume (see Section 4.2.3). A further background below 3 MeV is the cosmogenic ^{10}C, which can be suppressed by applying a time and space cut around each cosmic muon. Thus, LENA will be able to make the first high statistic measurement of ^{8}B neutrinos above 2 MeV. Hence, the MSW-LMA prediction for the transition region between vacuum and matter dominated oscillations can be tested (see Chapter 4 for details).

2.2.2 Supernova Neutrinos

Stars with a mass of more than eight solar masses $M_\odot$ build up an iron core, which is surrounded by different shells. As iron has highest binding energy per nucleon of all elements, it is not possible to gain energy by iron fusion. Thus, no fusion reactions occur in the centre of the star and the iron core grows through fusion reactions in the surrounding shell, until it reaches the Chandrasekhar mass of about 1.4 $M_\odot$ [55]. As this point, the core has a diameter of about 3000 km and a temperature of about 10^{10} K. Due to the high temperature, high energetic photons begin to disintegrate the iron core. This endothermic process reduces the thermal energy and thus the Fermi pressure of the electrons, which stabilized the core against the gravitational inward pull. The density increases further, so that electrons are captured on heavy nuclei and free protons. As the produced electron neutrinos can still leave the core, this loss in lepton number reduces the fermi pressure further, so that the core becomes gravitationally instable and collapses.
The collapse continues until the core reaches nuclear matter density and forms a so-called proto-neutron star, where the repulsive nuclear forces are large enough to compensate the gravitational force. While the inner part of the iron core collapses homogeneously and subsonically, the outer part of the core collapses supersonically and bounces on the proto-neutron star, forming a shock front. This shock front

Detection Channel	Type	Event Rate
(1) $\bar{\nu}_e + p \rightarrow n + e^+$	CC	$1.1 \cdot 10^4$
(2) $\nu_e + {}^{12}\mathrm{C} \rightarrow {}^{12}\mathrm{N} + e^-$	CC	$1.9 \cdot 10^2$
(3) $\bar{\nu}_e + {}^{12}\mathrm{C} \rightarrow {}^{12}\mathrm{B} + e^+$	CC	$1.8 \cdot 10^2$
(4) $\nu + p \rightarrow p + \nu$	NC	$1.3 \cdot 10^3$
(5) $\nu + e^- \rightarrow e^- + \nu$	NC+CC	$6.2 \cdot 10^2$
(6) $\nu + {}^{12}\mathrm{C} \rightarrow {}^{12}\mathrm{C}^* + \nu$	NC	$6.0 \cdot 10^2$

Table 2.2: Expected event rates for a supernova explosion of a $8\,\mathrm{M}_\odot$ star in the center of our galaxy (d=10 kpc), assuming a Maxwell-Boltmann spectrum with $\langle \mathrm{E}_\nu \rangle = 12\,\mathrm{MeV}$ and a detector threshold of 200 keV [56].

expand into the overlying iron core material, but loses energy by the dissociation of iron nuclei into free nucleons. Initially this shock still moves outwards, because of the high mass accretion rate of up to several solar masses per second. But when the mass accretion rate has decreased sufficiently, the shock front comes to a halt and forms a stagnant accretion shock at a radius between 100 km and 200 km.
Thus, there must be a mechanism that revives the stalled shock and triggers the supernova explosion. One possible explanation is that the neutrinos transfer energy to the shock by absorption-reemission processes as well as in scattering reactions. As the majority of the proto-neutron stars binding energies ($\sim 3 \cdot 10^{53}$ erg) is emitted by the neutrinos, a small fraction of the neutrino energy would already be sufficient to account for the canonical explosion energy of a core-collapse supernova (10^{50} erg to 10^{51} erg).
The expected neutrino emission of a supernova consists of three phases [56]:

- **Promp neutrino burst**: During the first ≈ 20 ms, the prompt ν_e burst is emitted. The neutrinos are mainly formed by electron capture on protons, so that the ν_e flux dominates.
- **Accretion phase**: During the accretion phase, which lasts about a few hundred ms, the shock stalls and the neutrino emission is powered by the infalling material. The flux of ν_e and $\bar{\nu}_e$ is expected to be up to two times larger than the flux of the other neutrino flavours.
- **Cooling phase**: The neutrino flux is dominated by the cooling of the proto neutron star. This phase lasts about 10 s to 20 s and the neutrinos are produced thermally. Thus, it is expected that the fluxes of the different flavours are almost equal.

About one to three supernova explosions are expected in our galaxy per century [31]. The mean distance of a supernova in the milky way is ≈ 10 kpc, so that about

$1.5 \cdot 10^4$ events are expected in LENA. There are six different detection channels. Three CC, two NC and one combined detection channel (see Table 2.2). Thus, a time resolved measurement of the ν_e and $\bar{\nu}_e$ flux as well as of the integrated flux over all flavours is possible. This would give important informations about the supernova explosion mechanism and would allow to improve the current models. The good energy resolution also allows to make a precise measurement of the neutrino spectrum, which would also be a very important information.
Furthermore, it might be possible to determine the mass hierarchy [57]. Depending on the mass hierarchy, the measured $\bar{\nu}_e$ flux on earth is:

$$\mathrm{NH} : \Phi_{\bar{\nu}_\mathrm{e}} = \cos^2\theta_{12}\Phi^0_{\bar{\nu}_\mathrm{e}} + \sin^2\theta_{12}\Phi^0_{\bar{\nu}_\mathrm{x}} \tag{2.1}$$

$$\mathrm{IH} : \Phi_{\bar{\nu}_\mathrm{e}} = \Phi^0_{\bar{\nu}_\mathrm{x}} \tag{2.2}$$

where $\Phi^0_{\bar{\nu}_\mathrm{e}}$ and $\Phi^0_{\bar{\nu}_\mathrm{x}}$ are the unoscillated fluxes. As the rise time of $\Phi^0_{\bar{\nu}_\mathrm{e}}$ and $\Phi^0_{\bar{\nu}_\mathrm{x}}$ is different during the accretion phase, it could be possible to identify the mass hierarchy by measuring the time resolved $\bar{\nu}_e$ and ν_x fluxes.

2.2.3 Diffuse Supernova Neutrinos

Apart from detecting supernova neutrinos, LENA is also sensitive to the Diffuse Supernova Neutrino Background (see Section 1.4). Due to the low flux, the only possible detection channel is the inverse beta decay (IBD) reaction on free protons:

$$\bar{\nu}_\mathrm{e} + \mathrm{p} \rightarrow \mathrm{e}^+ + \mathrm{n} \ . \tag{2.3}$$

As the neutron is much heavier than the positron, the positron gets almost all the energy of the $\bar{\nu}_e$, but reduced by $\sim 1.8\,\mathrm{MeV}$, due to the Q-Value of reaction (2.3). Thus, the neutrino energy can be reconstructed from the prompt positron signal. The neutron is captured by a free proton with a mean capture time of $\sim 250\,\mu\mathrm{s}$, producing a 2.2 MeV gamma[2]. Contrary to Super-Kamiokande, LENA can detect this gamma due to the lower threshold and uses the delayed coincidence signal to reduce the background.
Irreducible background from reactor and atmospheric antielectron neutrinos limit the detection window to $10\,\mathrm{MeV} - 25\,\mathrm{MeV}$ [44]. About 2 to 10 DSNB events per year are expected in this energy region. The exact value depends on the redshift dependent supernova rate and on the mean energy of the $\bar{\nu}_e$ spectrum.
Cosmogenic ^{9}Li, fast neutrons from the surrounding rock and neutral current interactions of atmospheric neutrinos pose additional backgrounds. A detailed analysis of these background sources and of the detection potential will be given in Chapter 6.

[2] About 1% of the neutrons are captured on ^{12}C, resulting in the emission of a 4.9 MeV gamma, or multiple gammas with 4.9 MeV total energy.

2.2.4 Geoneutrinos

Geoneutrinos are antielectron neutrinos that are produced by β^- decays of radioactive isotopes inside the earth. The main contribution to the geoneutrino flux comes from ^{40}K and from nuclides of the U and Th chains. Geoneutrinos from the U and Th chains can be detected with the inverse beta decay reaction (see equation 2.3), which has the advantage of a very good background suppression, due to the delayed coincidence signal. But because of the 1.8 MeV threshold for the IBD reaction, geoneutrinos that were emitted by ^{40}K can not be detected.
While geoneutrinos have already been detected by KamLAND [58] and Borexino [50], LENA would be the first experiment to perform a high statistic measurement with $\sim$ 1000 events per year [56].
Reactor antielectron neutrinos are a crucial background for the geoneutrino detection, as this background can not be distinguished on an event by event basis. At the Pyhäsalmi site, about 240 reactor $\bar{\nu}_e$ events are expected in the relevant energy region between 1.8 MeV and 3.2 MeV [59]. As the reactor $\bar{\nu}_\mathrm{e}$ spectrum extends above these energies and as its shape is well known, this background can be subtracted statistically.
Another background is caused by neutrons that are produced inside the target volume by the reaction of alpha particles, emitted for example by ^{210}Po, with ^{13}C:

$$^{13}\mathrm{C} + \alpha \rightarrow {}^{16}\mathrm{O} + \mathrm{n}\ . \tag{2.4}$$

These neutrons can mimic the delayed coincidence signal, as they produce a prompt signal by scattering off protons and a delayed signal when they are captured on a free proton. If the same radioactive purity level as in Borexino is reached, this background is negligible with about 10 events per year. The β^--neutron emitters ^{9}Li ($\mathrm{T}_{1/2} = 178$ ms) and ^{8}He ($\mathrm{T}_{1/2} = 119$ ms), that are produced by cosmic muons, are also a background for the geoneutrino detection. Due to the short half life of these isotopes, this background can be suppressed to about 1 event per year by applying a 2 s time cut after each cosmic muon crossing the detector [56]. As the cosmogenic isotopes are produced close to the muon track, the introduced dead time can be reduced from 6 % to 0.1 % if only a cylinder with 2 m radius is vetoed around each muon with nearly no loss in rejection power.
A further background are fast neutrons, that are produced by cosmic muons in the surrounding rock. These neutrons have a large range and can reach the target volume without triggering the muon veto. But due to the high energy of these neutrons, less than 10 events are expected in the geoneutrino energy region [60].
Due to the large signal and the low background, the geoneutrino flux at the Pyhäsalmi site can be measured with 3 % precision after one year. Thus, the current geochemical models, which predict that about 50 % terrestial heat flow is

generated by radioactive decays [61], can be tested. Furthermore, due to the different energy spectrum of geoneutrinos from the U and Th chain, the ratio between the U and Th abundance can be determined with 10 % precision after 3 years, which would also be an important test of the current earth models [56].
As the neutron is emitted in forward direction, it is also possible to obtain informations about the $\bar{\nu}_e$ direction by measuring the displacement between the prompt positron and the delayed neutron event. As the average displacement is with $1.9\,\text{cm} \pm 0.4\,\text{cm}$ rather small compared to the expected position resolution of about 10 cm [62], only a very unprecise reconstruction of the $\bar{\nu}_e$ direction is possible. Thus, a combined measurement with a second detector on the oceanic crust is probably necessary to disentangle the geoneutrino flux of the crust and of the earth mantle.

2.2.5 Proton Decay

The proton is stable in the standard model of particle physics, due to baryon number conservation, which has been introduced emperically. As there is no fundamental gauge symmetry which generates the baryon number conservation (as there is e.g. for the charge conservation), several extensions of the standard model predict a decay of the proton [63].
The best experimental limits for the proton decay were achieved by the Super-Kamiokande experiment. For the channel $p \rightarrow e^+\pi^0$, which is predicted by the minimal Grand Unified Theory SU (5), the current limit is $\tau_p > 8 \cdot 10^{33}$ y (90 % C.L.) [64]. The present limit for the channel $p \rightarrow K^+\bar{\nu}$, that is favored by supersymmetric models, is $\tau_p > 2 \cdot 10^{33}$ y (90 % C.L.) [65]. The sensitivity for the latter channel is limited by background, as the K^+ is below the Čerenkov threshold, so that only its decay products are visible in Super-Kamiokande.
In LENA, both the prompt signal of the K^+ and delayed signal of its decay products can be detected. Thus, there is a clear event signature which allows an efficient background rejection (see Figure 2.2). The main background for this channel are the charged current reactions of atmospheric muon neutrinos. Due to the double peak structure of the proton decay signal, this background can be reduced to less than 1 event per 10 years by a pulse shape analysis with 65 % signal efficiency. If no signal would be detected after 10 years, the proton lifetime limit could be increased to $\tau_p > 4 \cdot 10^{34}$ y (90 % C.L.), which is about one order of magnitude better than the current limit [48].

2.2.6 Long Baseline Neutrino Oscillations

LENA can also be used as the far detector of a long baseline neutrino beam experiment, which aims at the measurement of the mass hierarchy and CP-violating

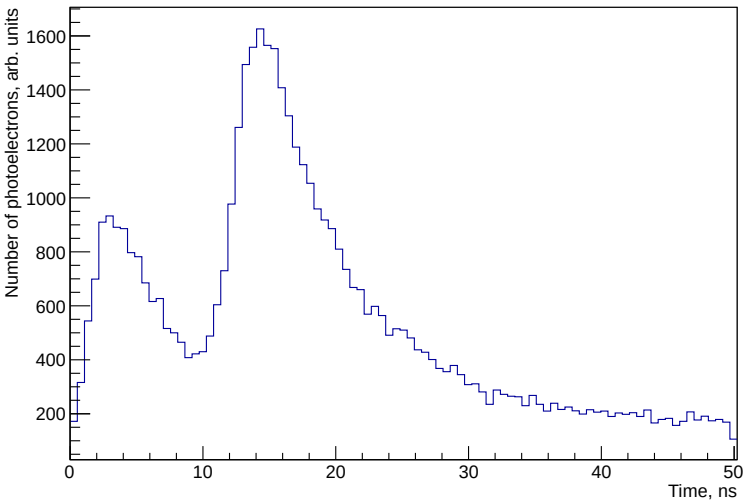

Figure 2.2: Simulated signal of a proton decay into a K^+ and an antineutrino. The first peak is due to the direct K^+ signal, while the second peak is caused by its decay products.

phase δ_{CP}. In a neutrino beam, protons are shot on a light target and produce charged pions. These pions are focused by a magnetic horn into a decay tunnel, where they decay mainly by the reaction:

$$\pi^{\pm} \rightarrow \mu^{\pm} + \overset{(-)}{\nu}_{\mu} \ . \tag{2.5}$$

Depending on the horn polarization, either muon or antimuon neutrinos are produced in the decay tunnel. The most important signal is the appearance of electron neutrinos ($\overset{(-)}{\nu}_{\mu} \rightarrow \overset{(-)}{\nu}_{\mathrm{e}}$), which depends amongst others on δ_{CP} and the mass hierarchy [66].
Currently, a neutrino beam experiment from CERN to the Pyhäsalmi mine with a distance of about 2300 km is investigated in the LAGUNA-LBNO design study. Figure 2.3 shows the electron appearance probability for NH and IH at this baseline. The oscillation maximum is at about 4 GeV, which requires a high energy proton beam. An upgraded version of the SPS accelerator could deliver $1.5 \cdot 10^{20}$ 400 GeV protons per year, which would correspond to a beam power of about 770 kW.
The clear difference of the signal for the NH and IH can be used to determine the mass hierarchy. To measure the electron neutrino appearance probability, $\overset{(-)}{\nu}_{\mu}$ and $\overset{(-)}{\nu}_{\mathrm{e}}$ CC events need to be distinguished, which can be done by pulse shape analysis,

due to the different lenghts of the muon and electron tracks.

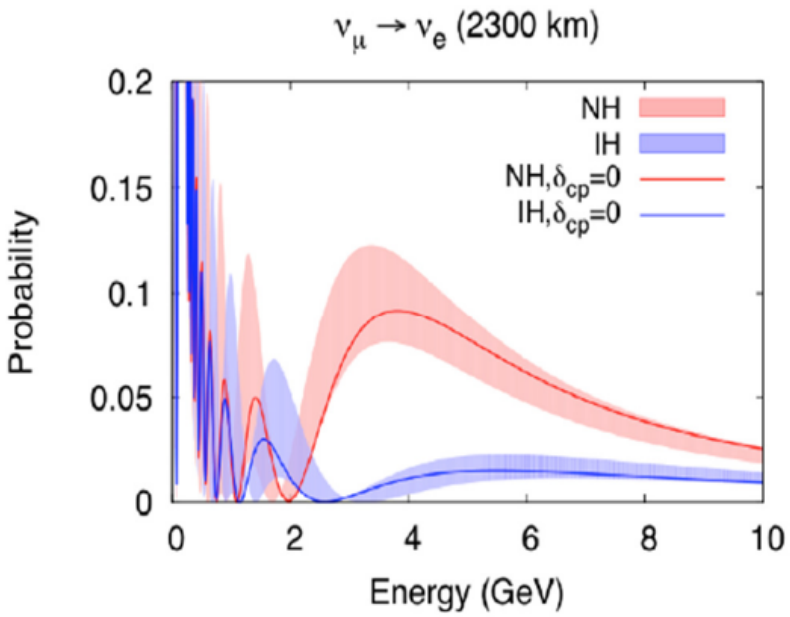

Figure 2.3: The electron neutrino appearance probability for the CERN to Pyhäsalmi beam for the NH (denoted in red) and the IH (denoted in blue) [67].

Backgrounds are the intrinsic beam contamination with $\overset{(-)}{\nu}_e$'s, caused by the suppressed decay mode $\pi^\pm \rightarrow e^\pm + \overset{(-)}{\nu}_e$, the oscillation of muon neutrinos into tau neutrinos and neutral current reactions of muon neutrinos. The NC background is crucial, as π^0's can be produced at these energies, which decay into two gammas and hence have a similar signature as the CC reaction of a $\overset{(-)}{\nu}_e$. By using the small difference of the pulse shape of NC and CC $\overset{(-)}{\nu}_e$ events, the NC background can be suppressed to about 10 % with a signal efficiency of 27 % [62].
Figure 2.4 shows the resulting sensitivity for the mass hierarchy determination. After two years of measuring time, the mass hierarchy can be determined with more than $3\,\sigma$ significance, independent of the value of δ_{CP} and after 10 years the significance increases to more than $5\,\sigma$.

As the dependence of the $\overset{(-)}{\nu}_e$ appearance probability on the δ_{CP} is small compared to the dependence on the mass hierarchy, detecting CP violation is not possible in LENA, unless the signal efficiency and the background suppression is substantially improved.

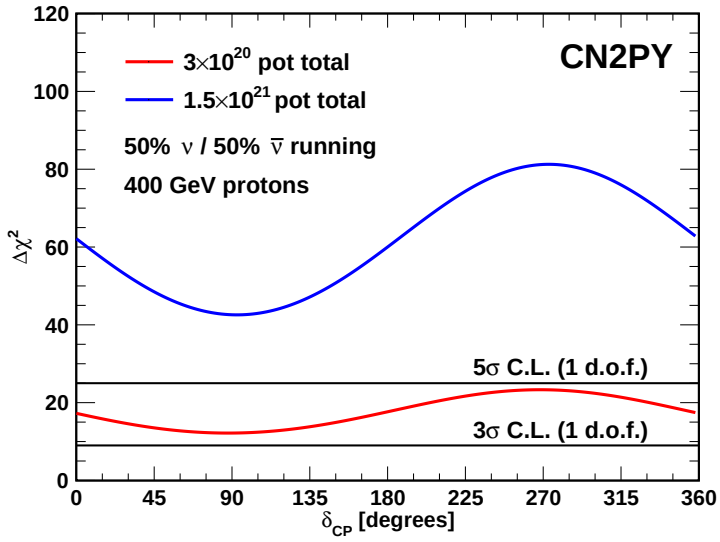

Figure 2.4: The mass hierarchy determination sensitivity in LENA, depending on the value of δ_{CP} [68]. Depicted are the sensitivies after 2 years (red line) and 10 years measuring time (blue line), assuming 50 % measuring time in neutrino and in antineutrino mode.

2.3 Experimental Challenges

As the dimensions of the LENA detector are more than one order of magnitude larger than the currently largest liquid scintillator detector KamLAND, there are several challenges for this project. Furthermore, the broad physics program makes the design of the detector even more complicated.

The requirements for the PMTs are quite stringent, as the energy of the studied physics events ranges from less than 1 MeV (^{7}Be solar neutrinos) to the GeV range (proton decay and LBNO). Thus, the PMTs need to have a large dynamic range, so that they can detect single photons without going into saturation when they detect hundreds of photons. Due to the large pressure at the bottom of the tank, the PMTs needs to be pressure encapsulated. As external gamma background is an important background for solar ^{8}B neutrinos (see Section 4.2.3), every component of the PMT and the pressure encapsulation needs to be designed carefully, so that the amount of ^{40}K, U and Th is minimized as far as possible.

Another challenge is the data acquisition (DAQ). If 12-inch PMTs are used, more than $3 \cdot 10^4$ channels need to be read out after one event. Due to the high energy physcis programm, the complete PMT pulse shape will be read out with a so-called flash analog to digital converter (FADC), to reconstruct the invidual hit time of

every detected photon [56]. Compared to Borexino, this will result in a huge increase of the amount of data per event. Furthermore, as there is only a small buffer volume in front of the PMTs, the trigger rate will be much higher. As the majority of the events are backgrounds events, caused by ^{14}C decays and by the external gamma background, a complex triggering system needs to be developed, to reduce the amount of stored data. A possible solution would be a multilayer trigger system, which combines a first level hardware trigger with several software based triggers.
The DAQ system must also be able to handle a large trigger rate in case of a supernova. The closest supernova candidate is the red supergiant Betelgeuse at a distant of about 200 pc [69]. If Betelgeuse becomes a supernova, about $1 \cdot 10^7$ events are expected during 10 s. As about 100 to 500 kB are written per event[3], the DAQ system must handle 100 to 500 GB per second without going into saturation.
While the mass hierarchy can be determined with LENA as a far detector in a neutrino beam experiment (see Section 2.2.6), detecting CP violating is only possible if the discrimination between NC ν_μ and CC $\bar{\nu}_e$ events is improved. One possible option is the reconstruction of the complete event vertex with every particle track. It was already demonstrated that 500 MeV muon tracks can be reconstructed in LENA [70]. Nevertheless, the reconstruction of multiple tracks is much more complicated and is currently investigated in the LAGUNA-LBNO design study.
Another important issue is the liquid scintillator and the liquid handling system of the detector. The solar neutrino program requires a radioactive background at the level of the Borexino detector, which is very challenging for such a big detector as LENA. Furthermore, due the large dimensions, a very transparent liquid scintillator with an attenuation length of more than 10 m is needed. Otherwise, the number of detected photons would be too small for the low energy physics program. But even with a large attenuation length, the photoelectron yield will still depend on the position of the event (see Chapter 3). Thus, the energy reconstruction of a event is not trivial and requires a precise position reconstruction.
Furthermore, the scintillator needs to have a large scattering length, as scattering smears out the differences between the pulse shapes of the electrons, protons and alphas. These pulse shape difference are necessary to reduce the background from NC reactions of atmospheric neutrinos, which is crucial for the DSNB detection (see Chapter 6).

[3]The exact amount depends on the number of triggered PMTs, which is position and energy dependent.

Chapter 3

Energy Reconstruction

In current liquid scintillator detectors like Borexino or KamLAND, the visible energy of an event is nearly proportional to the number of detected photons[1] (photo electrons). But in LENA, the photo electron yield also depends on the position of the event, due to the large dimensions compared to the attenuation lenght of the liquid scintillator. Hence, it is much more complex to reconstruct the energy of an event, which is a prerequisite for every physics analysis.
Thus, the position dependence of the photoelectron yield was studied during this thesis. For this study, the GEANT4 based LENA Monte Carlo simulation was used (see Section 3.1), which has been developed over the course of this thesis. Based on the simulated photo electron yield, an algorithm was designed that reconstructs the visible energy from the position and the number of detected photons (see Section 3.2). Finally, the performance of the algorithm was tested with simulated data (see Section 3.3).

3.1 The LENA Monte Carlo simulation

The LENA Monte Carlo simulation is based on the widely used GEANT4 simulation framework (Version 4.9.6.p01) [72]. It was originally written by T. Marrodàn Undagoitia [48] and further developed by J. Winter [73]. Over the course of this thesis, the optical model was significantly improved. Furthermore, the code was completely redesigned according to an object-orientated design [74], which increased the maintainability and the performance. Due to this approach, the simulation could be used as general tool for many other studies about the potential of the LENA detector [62, 70, 57, 75].

[1] There are two variables which are used for the energy reconstruction in Borexino. For low energy events, the number of triggered PMTs is used, while for higher energetic events the sum of the PMT charge, which is proportional to number of photoelectrons, is used [71].

3.1.1 Detector Setup

A slightly simplified detector geometry, compared to the one which was presented in Section 2.1 (see Figure 2.1), was implemented in the simulation, to save computation time. In the following, the symmetry axis of the cylinder is referred as the z-axis, and the radius is defined as $r = \sqrt{x^2 + y^2}$. The target consists of a 98 m high cylinder with 28 m in diameter, that is filled with linear alkyl benzene (LAB). A buffer volume with 2.0 m diameter encloses the target volume. The buffer volume is also filled with LAB, but the scintillation process is turned of in this volume.
In the current detector design it is planned to built a 60 cm thick concrete tank. But as cylindrical cavities with 30 cm diameter should be left open to leave space for installation (e.g. cooling or active leak proving), the concrete thickness varies from 30 cm to 60 cm. Thus, the thickness of the tank around the buffer volume was chosen to 30 cm, which is a conservative choice for the simulation of the fast neutron background[2] (see Section 6.3.2). The tank is enclosed by a 2 m thick water mantle, which is surrounded by limestone rock ($CaC0_3$).
The predefined GEANT4 physics list `QGSP_BERT_HP` (including G4MuonNuclearProcess and G4MuonMinusCaptureAtRest) (for details see [76]) was used to simulate hadronic and electromagnetic interactions of particles with energies from the eV to the GeV range. A validation of the models which are used in this physics list can be found in [77] and [78].
For the simulation of the scintillation process and the propagation of the so-called optical photons, which energies are in the visible range, an own optical model was implemented (see Section 3.1.2).

Photon Detection

Several options for the photon detection were implemented, to optimize the simulation for different use cases.

- **Detailed Mode**: In this mode, an optical module consisting of a PMT and a light concentrator (LC) is simulated, which is placed at the egde of the buffer volume, so that the aperture of LC is at a radius of 14 m. The LC was implemented as a full geometrical model, so that the path of the photon is precisely simulated. At the moment, the optical shape of the LCs is still investigated. Thus, a Borexino type LC with 86 % reflectivity [79] was implemented as a temporary solution. Hence, only 8-inch PMTs can be used for this option, as no geometrical LC model is currently available for larger PMTs.

[2]The implication of this approach for the simulation of the external gamma background are discussed in Section 4.2.3.

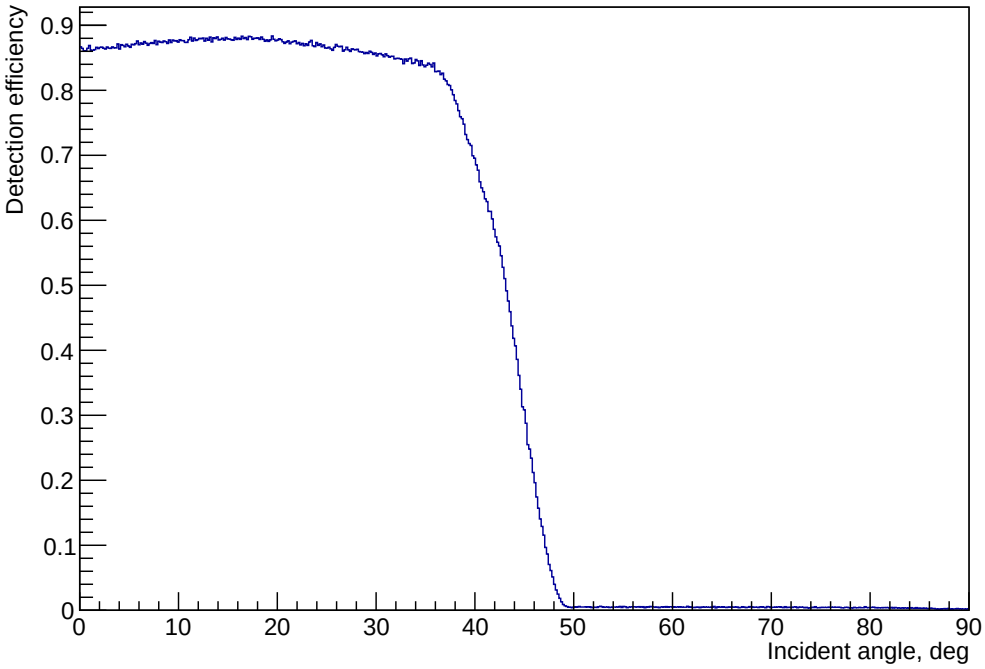

Figure 3.1: The dependence of the photon detection efficiency on the incident photon angle relative to the surface normal of the light concentrator's aperture. The detection efficiency for small a to shield gammas from the PMT glass. Thus, the photons can also be scattered inside the buffer liquid, so that the detection efficiency for large angles is greater than zero.

The LC focuses photons with a small incident angle relative to the surface normal of its aperture onto to photocathode and reflects photons with a large incident angle. Figure 3.1 shows the angle dependent efficiency of the used light concentrators. A large drop in the detection efficiency is visible around the critical angle of acceptance, which is at about 44°. For photons below this critical angle, the effective photosensitive surface of the optical module is enlarged by a factor of ~ 2.7. But as the optical modules are very close to the target volume in LENA, many photons are detected at a larger angle. Thus, averaged over a fiducial volume with 13.5 m radius, the effective photosensitive surface is only increased by a factor of ~ 1.4.

The photons are detected by a light sensitive half sphere (r=10.75 cm) that is placed in the center of the LC at a radius of 14.25 m. The quantum efficiency of a standard PMT is 20 % [44]. Thus, the light yield has to be reduced from 10000 to 2000 photons per MeV, as the quantum efficiency was set to 100 % in the simulation, to save computation time.

- **PMT Mode**: In this mode, the photons are still detected by individual PMTs, but no LCs are simulated. Instead, the PMTs are simulated as simple photosensitive disks. To include the effect of the LCs, the PMTs have an angle dependent detection efficiency, which was calculated by using the full optical module (see Figure 3.1). The size of the PMT is enlarged to the size of the corresponding LC aperture, and it is placed at a radius of 14 m. Thus, the effects of the LCs are included, without the time consuming simulation of the photon path inside the LC, which reduces the computation time by about 50 %.

  The only difference is that photons that are not detected are absorbed instead of being reflected back into target volume. Due to large dimensions of the detector, the probability to detect these photons is rather small. Nevertheless, this effect increases the photoelectron yield by about 4 %, so that the light yield has to be adjusted if no full optical module is simulated. The detected pulse shape also gets slightly distorted, which is an effect that cannot be corrected.

- **Simple Mode**:

  The computation time can be further reduced if no individual PMTs are simulated. Instead, a photosensitive volume is introduced which divides the buffer volume at a radius of 14.25 m, where the PMT cathode would be. The detection efficiency is angle dependent, to include the effects of the LCs. As the optical coverage is increased from 30 % to 100 %, the light yield of the simulation has to be further reduced. Due to angle dependent efficiency,

the new light yield can not be easily calculated, but had to be determined by a comparison between the photo electron yield of this mode and of the detailed mode. The resulting light yield for the simple mode is 1180 photons per MeV, which reduces the computation time by about 60 %, compared to the PMT mode. Furthermore, the simulation of each PMT itself, which is very time consuming, is no longer required so that the complete computation time is reduced by a factor ~ 20.

As no indivual PMTs are simulated, only the integrated pulse shape over all channels is available. Thus, this detection mode is not suitable to study the position reconstruction of low energy events ($E < 100\,MeV$), or the tracking of high energy events ($E > 100\,MeV$). But it can be used for many low energy studies (e.g. solar neutrinos, supernova neutrinos, DSNB) where only the energy and the integrated pulse shape of an event are important. Thus, if not stated otherwise, this detection mode was used for the studies that are presented in this thesis.

For all detection modes, several effects of the PMT were implemented[3]. First of all, the detection time of the photon is smeared with a gaussian ($\sigma = 1\,ns$), to simulate the transit time spread of the PMT. Late pulses, which are photons that are detected with a time delay [80], are also included. Prepulses, which are pulses that are detected too early, were not simulated as their contribution is negligible. Furthermore, fast after pulses, which are additional pulses that are generated in correlation with a primary pulse, are implemented. Pulses that are not correlated to a photon hit, so-called dark counts, were also simulated. A simple algorithm was implemented to reduce the dark count rate. For each detected hit, the distance to the event vertex was calculated and only hits with a distance of less than 30 m were stored. This cut reduced the number of detected photons by about 3 %, while it reduced dark counts by more than 50 %.
The parameters for all these PMT effects are denoted in Table 3.1.

3.1.2 Optical Model

As the scintillation model that is implemented in the GEANT4 code is not precise enough[4], a new model was developed for the simulation. The probability density function (PDF) F(t) of the photon emission process is described by several exponential functions:

$$F(t) = \sum_i \frac{N_i}{\tau_i} e^{-\frac{t}{\tau_i}} \ , \tag{3.1}$$

[3] A complete description of these effects can be found in [80, 2].

[4] In the standard Geant4 model, the PDF of the photon emission process can only be described by two exponential functions. Furthermore, quenching is not included.

Transit time spread (σ)	1 ns
Dark count rate	50 μs^{-1}
Late pulse rate	5 %
Late pulse time delay	50 ns
After pulse rate	5 %
After pulse time delay	40 ns

Table 3.1: The simulated PMT properties according to [80, 2]. The time delays for late and after pulses were smeared with a gaussian with $\sigma = 5$ ns. The dark count rate corresponds to 0.7 kHz per 8-inch PMT.

where τ_i is the time constant of the component i and $\mathrm{N_i}$ is the mean fraction of photons that are emitted with the time constant τ_i (such that $\sum_\mathrm{i} \mathrm{N_i} = 1$). The number of exponential functions is adjustable and a different value for $\mathrm{N_i}$ and τ_i can be set for each particle, which is necessary to reproduce the pulse shape of different particles.

In a liquid scintillator, the number of emitted photons is not proportional to the energy of the particle. The so-called quenching can be described by the emperical Birks formula [81]:

$$\frac{\mathrm{dL}}{\mathrm{dx}} = \frac{\mathrm{A}\frac{\mathrm{dE}}{\mathrm{dx}}}{1 + \mathrm{k_b}\frac{\mathrm{dE}}{\mathrm{dx}}} \,, \tag{3.2}$$

where $\frac{\mathrm{dL}}{\mathrm{dx}}$ is the number of photons emitted per unit path length, A is the light yield and $\mathrm{k_b}$ is a specific parameter for the scintillator, which is different for each particle. For electrons in the MeV range, $\mathrm{k_b}\frac{\mathrm{dE}}{\mathrm{dx}} \ll 1$ and the light output is almost proportional to the deposited energy. But this is not the case for heavier particles, like alpha and protons, at these energies, so that the quenching can not be neglected anymore.

Two different photon scattering processes were included in the simulation. Besides Rayleigh scattering, which is already implemented in GEANT4, there is also the possibility that an absorbed photon is reemitted. This reemission process is not instantaneous, but has a time delay which can be described by an exponential PDF $\frac{1}{\tau_\mathrm{re}}\mathrm{e}^{-\tau_\mathrm{re}}$.

Additionally, the absorption of a photon without reemission was also implemented.

The properties of the optical model are summarized in Table 3.2 and Table 3.3. No wavelength dependent effects were included in the simulation, which saves computation time. Instead, the scattering lengths were set to the measured value at 430 nm [44], which is close to the emission maximum of the scintillator.

Parameter	Electrons	Alphas
N_1	0.71	0.44
N_2	0.22	0.16
N_3	0.07	0.40
τ_1	4.6 ns	3.2 ns
τ_2	18 ns	18 ns
τ_3	156 ns	190 ns
k_b	$0.15 \frac{mm}{MeV}$	$0.11 \frac{mm}{MeV}$

Table 3.2: The photon emission parameters, according to [82, 83]. Note that the values for k_b were taken from a measurement of the Double Chooz veto scintillator, which consists of a mixture of 37.5 % LAB and 62.5 % tretadecane [82].

Parameter	Value
Rayleigh scattering length	40 m
Absorption-reemission length	60 m
τ_{re}	1.2 ns
Absorption length	20 m

Table 3.3: The values for the scattering and absorption lengths [44], as well as for the reemission time constant τ_{re} [48], which were used in the simulation. As the absorption length can not be measured directly, it was set to a value that is in agreement with the attenuation length measurements that were performed in [84].

3.2 The Energy Reconstruction Algorithm

In order develop an energy reconstruction algorithm, the position dependence of the photo electron yield had to be studied first. Therefore, electrons with 1 MeV kinetic energy were simulated at different points in the detector. The points were homogeneously distributed in x and in z direction (y=0 for all events), with 1 m distance between the points. Subsequently, the average photo electron yield was calculated for each simulated position. Figure 3.2 shows the resulting position dependence of the photo electron yield for the simple photon detection mode, where no indivual PMTs were used. The detection times of the photons were corrected for the time of flight between the event position and the detection position, and only photons that were detected in the time interval $[0\,\text{ns}, 600\,\text{ns}]$ were counted. This is the standard time gate for the analysis presented in this thesis, and was chosen such that also the slowest component of the photon emission PDF can be detected (see Section 3.1.2), while minimizing the number of detected dark counts. The dark count and the afterpulse rate were statistically subtracted, so that the photo electron yield correspond to the average number of detected photons per MeV. This substraction can be done as the PMT properties should be well known before the data taking starts, e.g. through an extensive testing of every PMT before it is mounted in the detector[5]. Furthermore, it is possible to directly determine the dark noise by measuring the number of PMT hits in an abitrary time window, where no physical event was detected.
Furthermore, the results without LCs are also depicted (see Figure 3.2 (lower part)). Obviously, the LCs have a big influence on the position dependence of the photo electron yield. Without LCs, the photon electron yield rises with decreasing distance to the edge of the target volume, where the photons are detected, because the probability that they are absorbed in the scintillator is reduced.
With LCs, the position dependence of the photo electron yield is reduced, due to the angle dependent detection efficiency. In the center of the detector ($z < 30\,\text{m}$), the photo electron yield rises also with the radius until $r \approx 10\,\text{m}$, though the increase is smaller than without LCs. But if the distance to the PMTs decreases further, the photo electron yield declines. The reason for this effect is that on average many photons hit the photosensitive area under a large incident angle, and are thus not detected.
As the photo electron yield varies from about 200 to 320 p.e. per MeV, the position of the event has to be reconstructed to determine its energy. The position can be determined with a resolution of about 10 cm (E=1 MeV) from the number of photons that are detected at each PMT and the arrival time of the photons,

[5] Another option is the calibration of every PMT once a week, by using LED light pulses, which are delivered to the PMT through an optical fiber, as it was done for the Borexino Outer Detector PMTs [71].

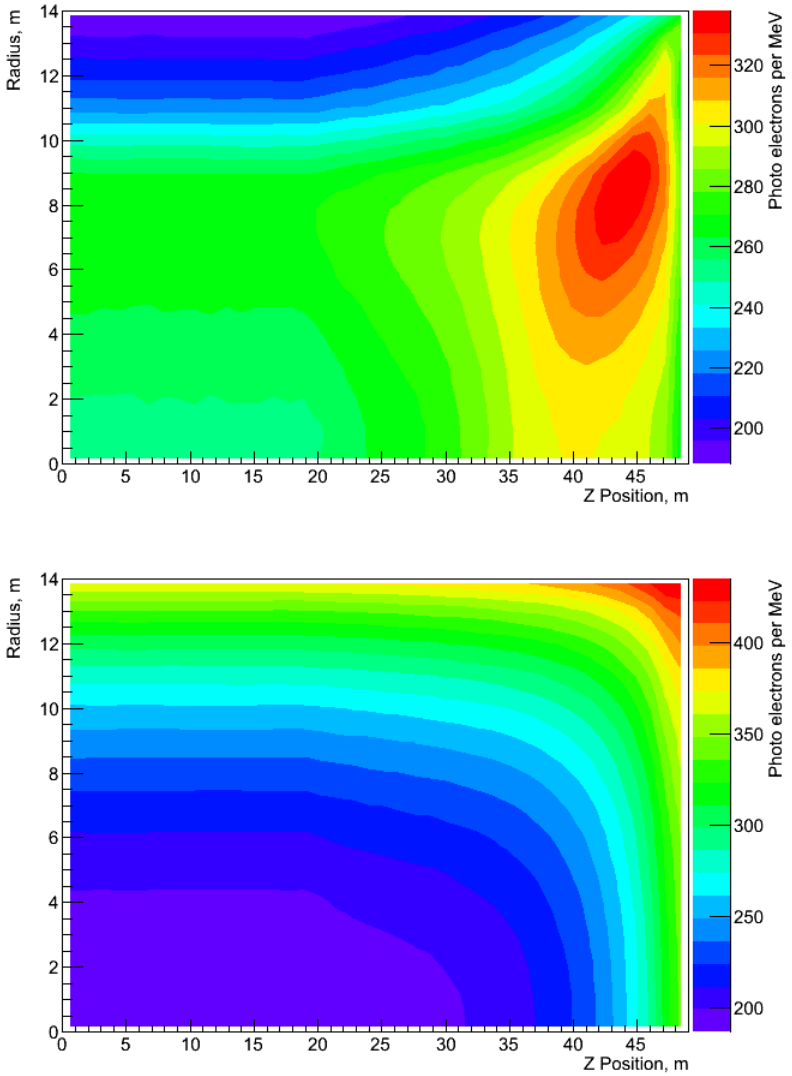

Figure 3.2: The simulated position dependence of the photo electron yield for the simple photon detection mode with (upper Figure) and without (lower Figure) LCs. Note that dark counts and the after pulses were statistically subtracted.

by using a negative logarithmic likelihood (NLL) fit [62]. This NLL fit is very time consuming. Therefore, a simple method was used, which calculates the event position $\vec{p}$ from the vertex positions of all detected photons $\vec{p}_{ph}(i)$:

$$\vec{p} = \sum_{i=0}^{N} \vec{p}_{ph}(i) \ . \tag{3.3}$$

This method uses Monte Carlo truth informations, which are not available in the real detector. Thus, the position resolution is overestimated. But the position resolution of the detector should have a negligible effect on the energy reconstruction, as the changes of the photo electron yield over a distance of 10 cm are always below 2 %.

As the position dependence of the photo electron yield cannot be described analytically, a simple and flexible approach was used to calculate the photo electron yield from the reconstructed position.

In a first step, the simulated LENA detector was calibrated using electrons at three different kinetic energies[6] (0.3 MeV, 0.5 MeV, 1.0 MeV), so that a possible energy dependence of the photo electron yield is also accounted for[7]. In the simulation, the only possible source for such an energy dependence is the quenching, while in the real experiment, non-linearities of the electronics and the PMT charge response could also introduce such an effect.

The calibration points were homogeneously distributed in x and in z direction (y=0 for all events), with 1 m distance between the calibration points. This is sufficient to identify all position dependent effects, as LENA is rotationally symmetric referred to the z-axis. Furthermore, only events in the upper half of the cylinder ($z > 0$) were simulated, as the photo electron yield has the same position dependence in the upper and the lower half of the cylinder. For each simulated energy, 1500 events were simulated at each calibration point and the average photo electron yield was calculated by fitting a gaussian.

Using these calibration data, the energy of an arbitrary event is reconstructed in the following way. First of all, the position of the event is reconstructed and the nearest calibration point is determined. Subsequently, the dark counts are subtracted from the number of detected hits. Due to the dark count suppression cut (see Section 3.1.1), the dark count rate also depends on the position (see Figure 3.3). The dark count rate at the event position $\mathrm{DC(r, z)}$ is calculated by making a linear interpolation of the dark count rate at the adjacent calibration positions:

$$\mathrm{DC(r, z)} = \mathrm{DC(r_c, z_c)} + \frac{\mathrm{r - r_c}}{1\,\mathrm{m}} \Delta\mathrm{DC_r} + \frac{|\mathrm{z}| - \mathrm{z_c}}{1\,\mathrm{m}} \Delta\mathrm{DC_z} \ , \tag{3.4}$$

[6] The calibration energies are not fixed and can be adjusted for different use cases.

[7] For a list of possible calibration sources see [85].

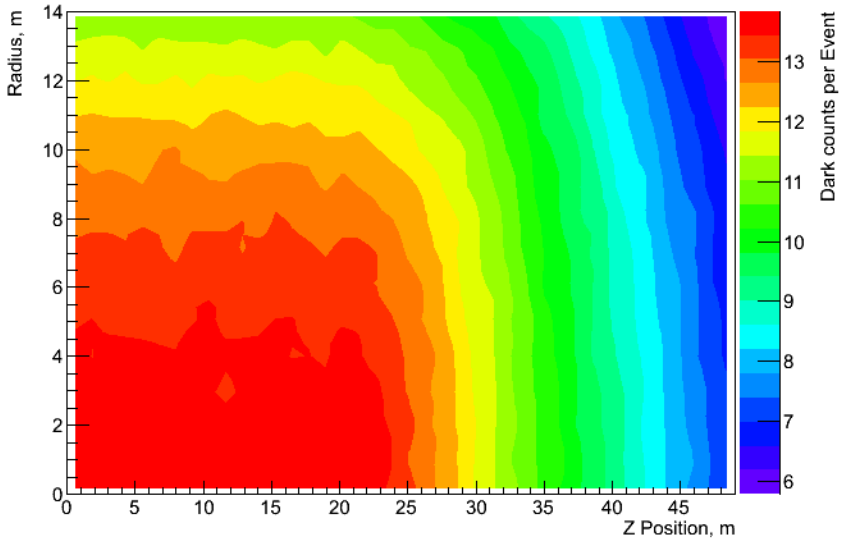

Figure 3.3: The position dependence of the dark count rate.

where $DC(r_c, z_c)$ is the dark count rate at the nearest calibration point, and $\Delta DC_{r/z}$ is the difference between the dark count rate at the adjacent calibration positions:

$$\Delta DC_r = (DC(r_c + 1\,m \cdot \mathrm{sgn}\,(r - r_c)\,, z_c) - DC(r_c, z_c)) \cdot \mathrm{sgn}\,(r - r_c) \tag{3.5}$$

$$\Delta DC_z = (DC(r_c, z_c + 1\,m \cdot \mathrm{sgn}\,(|z| - z_c)) - DC(r_c, z_c)) \cdot \mathrm{sgn}\,(|z| - z_c) \tag{3.6}$$

Afterwards, a first energy estimate E_{est} is calculated:

$$E_{est} = \frac{Ph_{corr}}{PY(r_c, z_c, 300\,keV)}\ , \tag{3.7}$$

where $Ph_{corr} = Ph_{det} - DC(r, z)$ is the dark count corrected number of hits and $PY(r_c, z_c, 300\,keV)$ is the photo electron yield at the closest calibration point for the 300 keV calibration run. Using this energy estimate, the average photo electron yield $PY(r, z, E_{est})$ is calculated by making a linear approximation of the photo electron yield at the adjacent calibration points:

$$PY(r, z, E_{est}) = PY(r_c, z_{cal}, E_c) + \frac{r - r_c}{1\,m}\Delta PY_r + \frac{|z| - z_c}{1\,m}\Delta PY_z + \Delta PY_E\ , \tag{3.8}$$

where $PY(r_c, z_c, E_c)$ is the photo electron yield at the closest calibration position and with the energy E_c, which is closest to the estimated energy. $\Delta PY_{r/z}$ is the

difference between the photo electron yield at the adjacent calibration positions:

$$\Delta \mathrm{PY_r} = (\mathrm{PY}(\mathrm{r_c} + 1\,\mathrm{m} \cdot \mathrm{sgn}\,(\mathrm{r} - \mathrm{r_c})\,, \mathrm{z_c}, \mathrm{E_c}) - \mathrm{PY}(\mathrm{r_c}, \mathrm{z_c}, \mathrm{E_c})) \cdot \mathrm{sgn}\,(\mathrm{r} - \mathrm{r_c}) \tag{3.9}$$

$$\Delta \mathrm{PY_z} = (\mathrm{PY}(\mathrm{r_c}, \mathrm{z_c} + 1\,\mathrm{m} \cdot \mathrm{sgn}\,(|\mathrm{z}| - \mathrm{z_c})\,, \mathrm{E_c}) - \mathrm{PY}(\mathrm{r_c}, \mathrm{z_c}, \mathrm{E_c})) \cdot \mathrm{sgn}\,(|\mathrm{z}| - \mathrm{z_c}) \tag{3.10}$$

and $\mathrm{PY_E}$ accounts for a possible energy dependence of the photo electron yield. Depending on the estimated energy is it either:

$$\mathrm{PY_E} = \frac{\mathrm{E_{est}} - \mathrm{E_c}}{0.2\,\mathrm{MeV}} \cdot (\mathrm{PY}(\mathrm{r_c}, \mathrm{z_c}, 0.5\,\mathrm{MeV}) - \mathrm{PY}(\mathrm{r_c}, \mathrm{z_c}, 0.3\,\mathrm{MeV})) \tag{3.11}$$

if $\mathrm{E_{est}} < 0.5\,\mathrm{MeV}$ or:

$$\mathrm{PY_E} = \frac{\mathrm{E_{est}} - \mathrm{E_c}}{0.5\,\mathrm{MeV}} \cdot (\mathrm{PY}(\mathrm{r_c}, \mathrm{z_c}, 1.0\,\mathrm{MeV}) - \mathrm{PY}(\mathrm{r_c}, \mathrm{z_c}, 0.5\,\mathrm{MeV})) \tag{3.12}$$

In case that the energy of the event is much larger than the calibration energies, equation (3.12) usually overestimates $\mathrm{PY_E}$, due to the statistical fluctuations of the calibrations measurements. Hence, for estimated energies above 2.0 MeV, equation (3.12) is modified to:

$$\mathrm{PY_E} = 2 \cdot (\mathrm{PY}(\mathrm{r_c}, \mathrm{z_c}, 1.0\,\mathrm{MeV}) - \mathrm{PY}(\mathrm{r_c}, \mathrm{z_c}, 0.5\,\mathrm{MeV}))\ . \tag{3.13}$$

Using $\mathrm{PY}(\mathrm{r}, \mathrm{z}, \mathrm{E_{est}})$ and the dark count corrected number of hits $\mathrm{Ph_{corr}}$, the reconstructed energy E is:

$$\mathrm{E} = \frac{\mathrm{Ph_{corr}}}{\mathrm{PY}(\mathrm{r}, \mathrm{z}, \mathrm{E_{est}})}\ . \tag{3.14}$$

The reconstruction algorithm relies on the fact that the position dependence of the photo electron yield is small compared to the position resolution (10 cm at 1 MeV), so that a linear interpolation can be applied. But this is not the case anymore at the edge of the target volume (see Figure 3.4). If a photon is emitted between two optical modules (e.g. at $\mathrm{z} \approx 0.5\,\mathrm{m}$, $\mathrm{r} \gtrsim 13.85\,\mathrm{m}$), the incident angle of the photon to the surface normal of the LC is too large to detect the photon. Thus, the photon can only be detected on the other side of the detector or if it is scattered in the scintillator. But if it is emitted in front of the optical module, the incident angle is low and the aperture of the LC covers a large solid angle. Hence, the photo electron yield changes up to a factor of 5 over $\sim 30\,\mathrm{cm}$.
Due to these large changes over small distances, the energy of an event can not be reconstructed precisely in this part of the detector. Thus, the volume that is suitable for physical analysis is limited to $\mathrm{r} < 13.5\,\mathrm{m}$ and $|\mathrm{z}| < 48.5\,\mathrm{m}$, so that the distance of the event to the nearest optical module is always at least 0.5 m[8]. Thus, the active detector mass is reduced from 50.8 kt to 47.8 kt.

[8] This is only an upper limit. External gamma background (see Section 4.2.3) and fast neutrons (see Section 6.3.2) can further limit the usable volume for the different measurements.

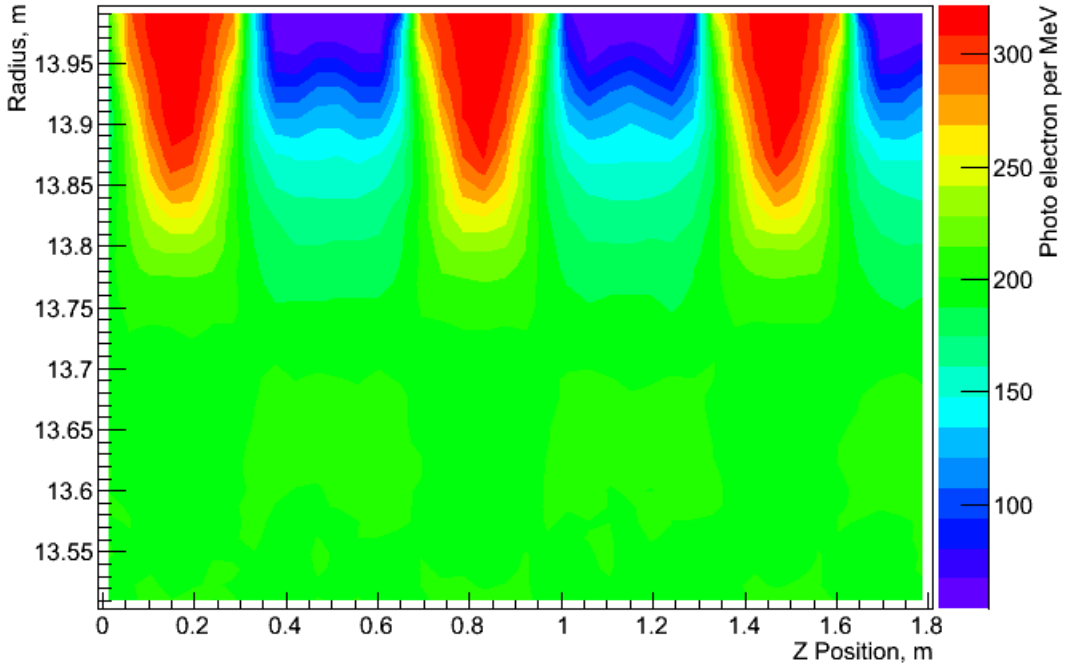

Figure 3.4: The position dependence of the photo electron yield at the egde of the target volume for the detailed photon detection mode. Due to the LCs, the chance to detect photons that were emitted between two optical modules (e.g. at $z \approx 0.5\,\mathrm{m}$, $r \gtrsim 13.85\,\mathrm{m}$) is low compared to the probability to detect photons that were emitted in front a the PMT (e.g. e.g. at $z \approx 0.5\,\mathrm{m}$, $r \gtrsim 13.85\,\mathrm{m}$).

3.3 Results

The energy reconstruction algorithm was validated in the following way: For each calibration point, 1500 electron events with a kinetic energy of 1 MeV were simulated at 0.5 m distance to the calibration point in z and in r direction. For example, if the calibration point was at r=0 m and z=0 m, the events were simulated at the position r=0.5 m and z=0.5 m. Thus, the distance to the nearest calibration point was maximal, as the distance between two calibration point is 1 m. Hence, the algorithm was tested at the positions where the largest deviations between the reconstructed and the true energy are expected. The reconstructed energy was fitted with a gaussian and the shift of the mean reconstructed energy from the true energy was calculated ($E_{rec} - E_{true}$). The results of this simulation are depicted in Figure 3.5.
For the majority of the detection volume, the systematic energy reconstruction error was between -1 % and 1 %. In the volume $r \lesssim 10$ m and $|z| \lesssim 40$ m, the reconstucted energy tends to be too high. This behaviour changes when $r \gtrsim 10$ m and the photo electron yield decreases with the radius (see Figure 3.2). The reason for this effect is that the linear interpolation underestimates the rise of the photo electron yield for $r \lesssim 10$ m, and thus the reconstructed energy is on average too high in this region. Once the photo electron yield decreases with the radius (for $r \gtrsim 10$ m and $|z| \lesssim 40$ m), the linear interpolation returns on average a too large photo electron yield, so that the reconstructed energy is lower than the true one. The small scale structures that can be seen for $|z| \lesssim 40$ m are due to statistical fluctuations, as the statistical error of the mean reconstructed energy is about 0.15 %.
At the corner of target volume ($r > 13$ m and $|z| > 48$ m) the systematic shift of the reconstructed energy rises up to 20 %. This is caused by the large changes in the photo electron yield in this region, so that the linear approximation is not precise enough. Thus, more calibration points are needed in this part of the detector. But as the shift is not too large and as the volume is rather small (less than 0.1 % of the total volume), the effect on the average systematic energy reconstruction error is insignificant.
Figure 3.6 shows the ratio of the reconstructed to the true energy for 1 MeV electrons, which were homogeneously distributed over the whole target volume. One can see that the shifts that are present in Figure 3.5 are not detectable anymore if one averages over the whole detetector volume. The reason for this is that some of the shifts are due to statistical fluctuations and that only positions which were at a maximal distance to the calibration points were tested.
The energy resolution at 1 MeV is about 6.5 %, while an energy resolution of 6.1 % was expected from the averaged photo electron yield of 271. There are two reasons for this deviation. First of all, dark counts worsen the energy resolution, though

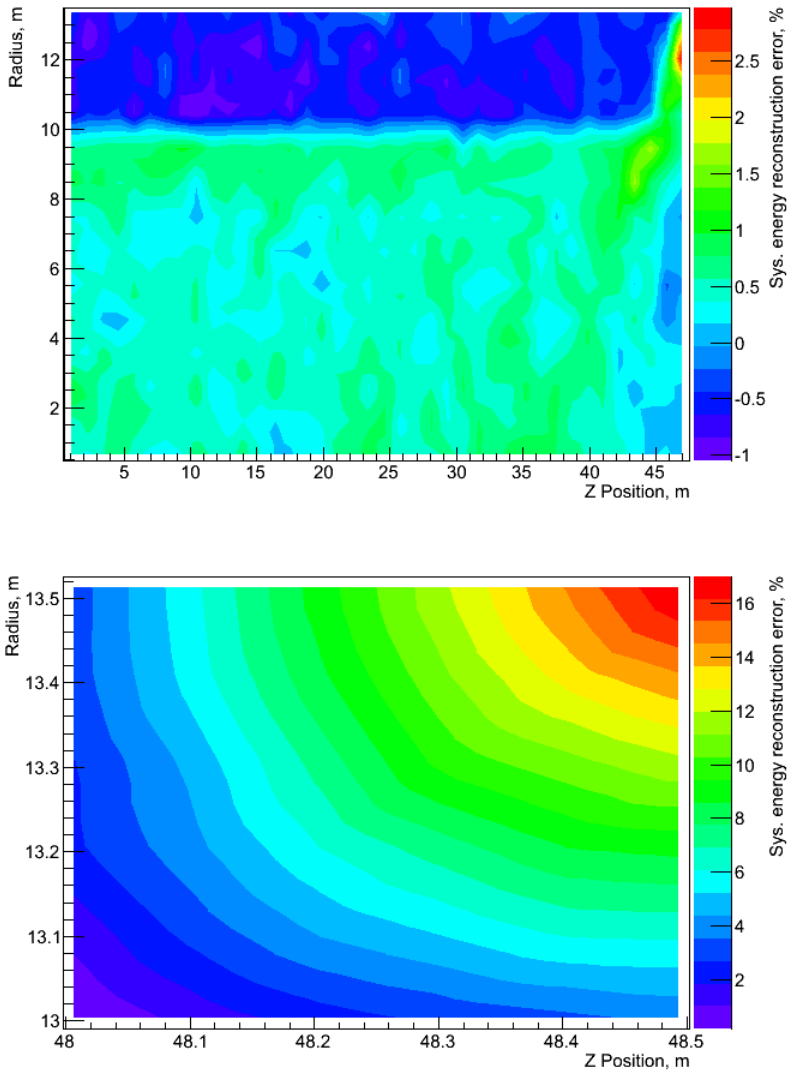

Figure 3.5: The position dependence of the systematic energy reconstruction error for $|z| < 48\,\mathrm{m}$ (upper Figure) and for $r > 13\,\mathrm{m}$ and $|z| > 48\,\mathrm{m}$ (lower Figure).

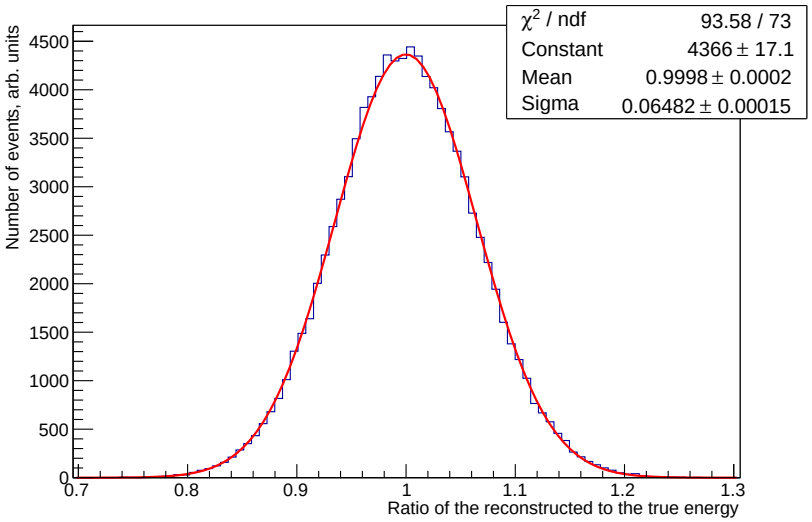

Figure 3.6: The ratio of the reconstructed to the true energy for 1 MeV electrons, which were homogeneously distributed over the whole target volume. Furthermore, a fit with a gaussian (red line) is also depicted.

this effect is not big enough to explain the shift alone. The second reason is that the energy is not reconstructed without a systematic shift at all positions in the target volume (see Figure 3.5). Though these shifts don't have a detectable effect on the average reconstructed energy, they still widen the distribution of the reconstructed energy and thus worsen the energy resolution.
Figure 3.7 shows the energy resolution σ_{E} for energies from 0.5 MeV to 10.0 MeV. The energy dependence of σ_{E} can be approximated with the function

$$\sigma_{\mathrm{E}} = \mathrm{a} \cdot \sqrt{\mathrm{E}/\mathrm{MeV}} + \mathrm{b} \ , \tag{3.15}$$

where the parameter a depends on the average photo electron yield. The parameter b had to be introduced to consider the systematic energy reconstruction deviation at some positions in the target volume. It can be reduced if more calibrations points are used, and if more events are simulated at each calibration point. Though equation (3.15) is a good approximation, is not a completely correct model, as the χ^2/NDF of the fit is 401.7/11.
A small systematic energy reconstruction shift of 0.5 % to 1.0 % was found for energies above 1.5 MeV. The reason for this error is that the calibration runs had only energies up to 1 MeV. While the error is not big, it shows that several sources with a wide distribution of energies are needed for the calibration of the LENA detector.

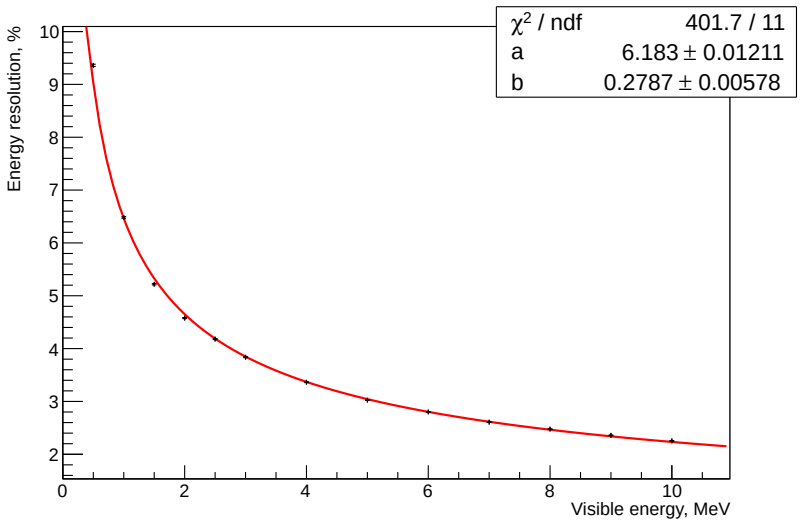

Figure 3.7: The energy dependence of the energy resolution (black points). A fit with the function $\sigma_{\mathrm{E}} = \mathrm{a} \cdot \sqrt{\mathrm{E}/\mathrm{MeV}} + \mathrm{b}$ is plotted in red.

Chapter 4

Test of the MSW-LMA Effect with Solar ^{8}B Neutrinos

There are several measurements that confirm the MSW-LMA effect in the vacuum and in the matter dominated energy region (see Section 1.2). But a precision measurement in the transition region between $\sim 2\,\mathrm{MeV}$ and $\sim 5\,\mathrm{MeV}$ is still missing, as WCDs have a too high energy threshold and current LSDs are too small. A measurement in this region is very important, as any deviation from the MSW-LMA prediction would be a sign for new physics like non-standard neutrino interactions or light sterile neutrinos ($m_{\nu_1} < m_{\nu_0} < m_{\nu_2}$) [19].
Due to its large target mass, a high statistics measurement of the ^{8}B solar neutrino recoil spectrum down to 2 MeV will be possible with LENA. Therefore, the sensitivity of LENA to deviations of P_{ee} from the MSW-LMA prediction was analyzed with a Monte Carlo simulation.
In a first step, the solar neutrino spectra were simulated with the ν_e survival probability P_{ee} calculated according to the MSW-LMA prediction and with a constant P_{ee} (see Section 4.1). Afterwards, the different backgrounds were simulated (see Section 4.2). In the next step, 10^5 measurements were simulated, assuming that the MSW-LMA prediction is correct (see Section 4.3). Finally, for each measurement a spectral fit with the MSW-LMA prediction and with a constant P_{ee} was performed, to analyze how well these two models can be separated (see Section 4.4).

4.1 Simulation of the Solar Neutrino Spectra

There are two detection channels for ^{8}B solar neutrinos in LENA. The elastic neutrino electron scattering (ES) channel and the CC reaction of ν_e on ^{13}C (^{13}C channel). Compared to the ES channel, the ^{13}C channel allows a better background

suppression and an event by event reconstruction of the neutrino energy. The disadvantage of this channel is that the statistics are reduced due to the low isotopic abundance I=1.07 % of ^{13}C.

4.1.1 Elastic Neutrino Electron Scattering

In the elastic scattering (ES) channel, the electron neutrino scatters elastically off an electron:

$$\nu_{\mathrm{x}} + \mathrm{e}^- \rightarrow \nu_{\mathrm{x}} + \mathrm{e}^- \ , \tag{4.1}$$

and the recoil electron is subsequently detected. As it is not possible to detect the scattered neutrino, the energy of the neutrino can not be reconstructed on an event by event basis, as the energy of the electron also depends on the scattering angle. Due to the kinematics of reaction (4.1), the recoil energy T of the electron is limited to[1]:

$$\mathrm{T} \leq \frac{2\mathrm{E}_\nu^2}{\mathrm{m_e} + 2\mathrm{E}_\nu} \ , \tag{4.2}$$

where E_ν is the neutrino energy and $\mathrm{m_e}$ is the electron mass. Thus, a monoenergetic neutrino source, like ^{7}Be neutrinos, has a spectrum with a charactistic compton-like shoulder.
If $\mathrm{E}_\nu \gg \mathrm{m_e}$, the total cross section can be approximated by the following expressions:

$$\sigma_{\nu_{\mathrm{e}}} = 9.2 \cdot 10^{-45} \frac{\mathrm{E}_\nu}{\mathrm{MeV}} \, \mathrm{cm}^2 \tag{4.3}$$

$$\sigma_{\nu_{\mu/\tau}} = 1.5 \cdot 10^{-45} \frac{\mathrm{E}_\nu}{\mathrm{MeV}} \, \mathrm{cm}^2 \tag{4.4}$$

The larger cross section for electron neutrinos is due to the fact that electron neutrinos can also interact via the CC channel.
For this analysis, the complete tree-level differential cross section[2] was used [42]:

$$\frac{\mathrm{d}\sigma}{\mathrm{dT}} = \frac{2\mathrm{G_F^2 m_e}}{\pi \mathrm{E}_\nu^2} \left[\mathrm{A}^2 \mathrm{E}_\nu^2 + \mathrm{B}^2 \left(\mathrm{E}_\nu - \mathrm{T} \right)^2 - \mathrm{AB m_e T} \right] \ , \tag{4.5}$$

where $\mathrm{G_F}$ is the fermi coupling constant and A and B are constants that depend on the weak mixing angle θ_W. For ν_e, $\mathrm{A} = -0.5 - \sin^2\theta_{\mathrm{W}}$ and for $\nu_{\mu/\tau}$, $\mathrm{A} = 0.5 - \sin^2\theta_{\mathrm{W}}$. In contrast, $\mathrm{B} = -\sin^2\theta_{\mathrm{W}}$ is independent of the neutrino flavour[3].

[1] In equation (4.2), the approximation $\mathrm{m}_\nu = 0$ was used.

[2] Loop corrections, which have an effect of about 1 % on the total cross section, are not considered in this analysis.

[3] To calculate the differential cross section for anti neutrinos, A and B needs to be exchanged.

Source	Flux
pp	$6.06 \cdot 10^{10}\,\mathrm{cm^{-2}s^{-1}}$
^{7}Be	$4.34 \cdot 10^{9}\,\mathrm{cm^{-2}s^{-1}}$
pep	$1.45 \cdot 10^{8}\,\mathrm{cm^{-2}s^{-1}}$
^{13}N	$2.01 \cdot 10^{8}\,\mathrm{cm^{-2}s^{-1}}$
^{15}O	$1.45 \cdot 10^{8}\,\mathrm{cm^{-2}s^{-1}}$
^{17}F	$3.25 \cdot 10^{6}\,\mathrm{cm^{-2}s^{-1}}$
^{8}B	$4.51 \cdot 10^{6}\,\mathrm{cm^{-2}s^{-1}}$
hep	$8.25 \cdot 10^{3}\,\mathrm{cm^{-2}s^{-1}}$

Table 4.1: The average solar neutrino fluxes on earth according to the low metallicity BS05(AGS,OP) standard solar model [14].

The electron recoil spectra for the ES channel were simulated in two steps. First of all, the differential event rate for the different solar neutrino types was calculated by integrateing over the neutrino energy:

$$\frac{\mathrm{dR}_{\nu_\mathrm{e}}}{\mathrm{dT}} = \mathrm{n_e} \cdot \Phi \int_0^{\mathrm{E_{max}}} \mathrm{dE}_\nu \, \lambda(\mathrm{E}_\nu) \cdot \mathrm{P_{ee}}(\mathrm{E}_\nu) \cdot \frac{\mathrm{d}\sigma_{\nu_\mathrm{e}}(\mathrm{E}_\nu, \mathrm{T})}{\mathrm{dT}} \tag{4.6}$$

$$\frac{\mathrm{dR}_{\nu_{\mu,\tau}}}{\mathrm{dT}} = \mathrm{n_e} \cdot \Phi \int_0^{\mathrm{E_{max}}} \mathrm{dE}_\nu \, \lambda(\mathrm{E}_\nu) \cdot (1 - \mathrm{P_{ee}}(\mathrm{E}_\nu)) \cdot \frac{\mathrm{d}\sigma_{\nu_{\mu,\tau}}(\mathrm{E}_\nu, \mathrm{T})}{\mathrm{dT}} \tag{4.7}$$

where T is the recoil energy of the electron, $\mathrm{n_e}$ is the number of electrons in the target volume, Φ is the neutrino flux (see Table 4.1), $\mathrm{E_{max}}$ is the maximal neutrino energy, $\lambda(\mathrm{E}_\nu)$ is the normalized spectral shape of the neutrino flux, $\mathrm{P_{ee}}(\mathrm{E}_\nu)$ is the energy dependent electron neutrino survival probability and $\frac{\mathrm{d}\sigma_{\nu_\mathrm{x}}(\mathrm{E}_\nu,\mathrm{T})}{\mathrm{dT}}$ is the differential cross section (see Section 4.1.1) for the corresponding neutrino flavour. Afterwards, 10^6 electron events with a spectrum according to equation (4.6) and (4.7) were simulated for each neutrino source. The event positions were homogeneously distributed over the whole usable target volume ($\mathrm{r} < 13.5\,\mathrm{m}$ and $|\mathrm{z}| < 48.5\,\mathrm{m}$). For each event, the visible energy was reconstructed according to Section 3.2.
Figure 4.1 shows the obtained visible energy spectra for the different neutrino sources. $\mathrm{P_{ee}}(\mathrm{E}_\nu)$ was calculated according to the MSW-LMA prediction (see Section 1.2) and the integral spectrum of the CNO-cycle is shown instead of the spectral components (^{13}N, ^{15}O, ^{17}F). The compton-like shoulders of the monoenergetic ^{7}Be and pep neutrinos are clearly visible around 700 keV and 1.2 MeV, while there is no edge for the continuous ^{8}B spectrum. While the flux of the pp neutrinos is the largest (see Table 4.1), they have also the lowest energy spectrum. Hence, ^{7}Be neutrinos have the largest event rate due to the 200 keV threshold and

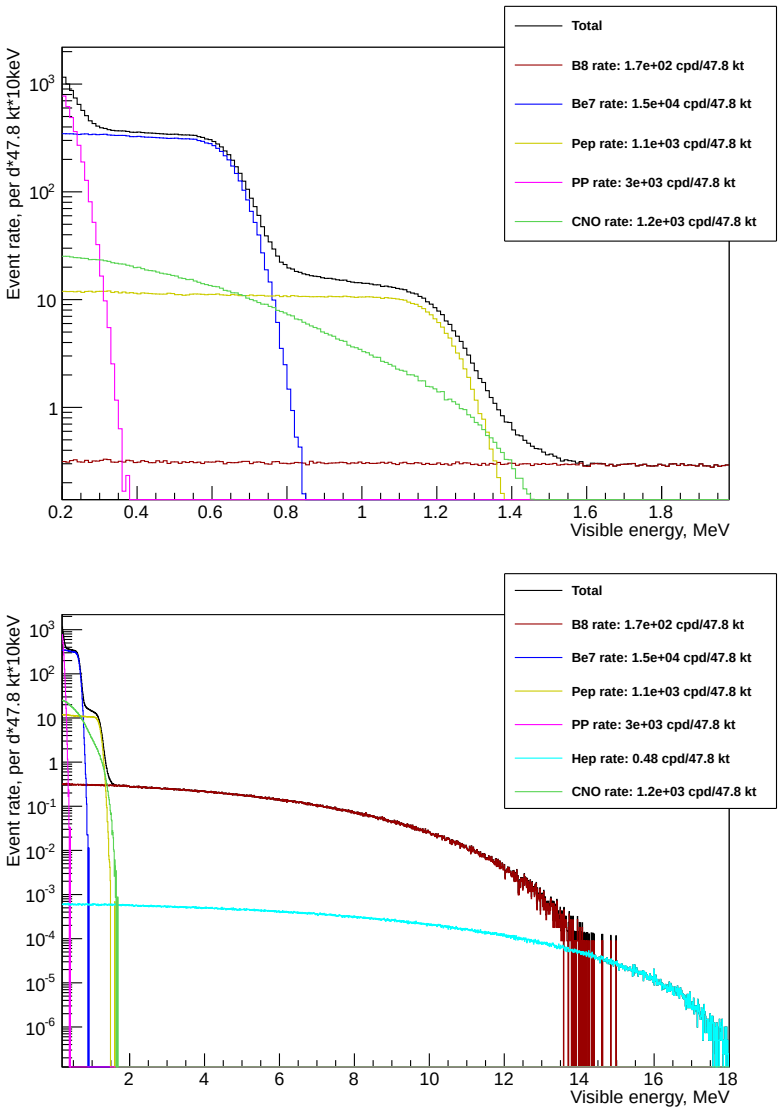

Figure 4.1: The simulated visible energy spectra for solar neutrinos with $P_{ee}(E_\nu)$ according to the MSW-LMA prediction for the ES channel. The spectral shapes of the neutrino fluxes were taken from [86, 87, 88, 89].

the increased cross section at higher energies. Above $\sim 1.5\,\mathrm{MeV}$, the ^{8}B spectrum is the dominant one with more than two orders of magnitude more events than the hep spectrum.

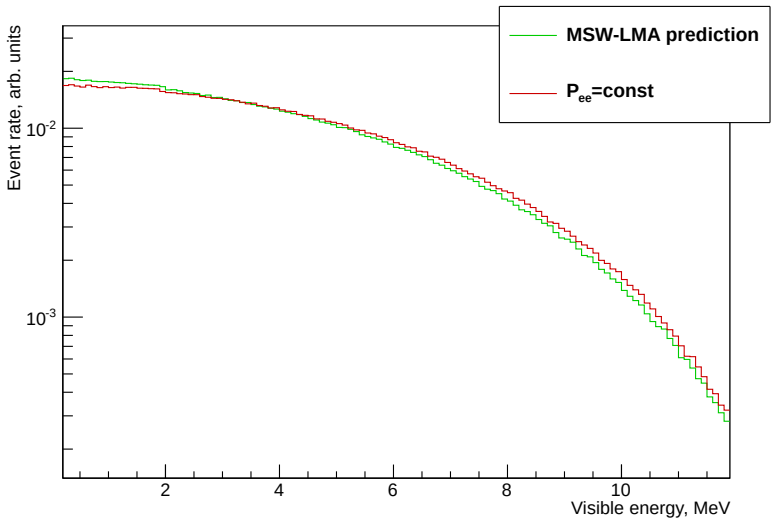

Figure 4.2: The normalized ^{8}B spectrum for P_{ee}=const (denoted in red) and P_{ee} (denoted in green) according to the MSW-LMA prediction for the ES channel.

Figure 4.2 shows the normalized ^{8}B spectrum for $P_{ee}(E_\nu)$=const and $P_{ee}(E_\nu)$ according to the MSW-LMA prediction. The difference between the two spectra is relatively small compared to the difference in $P_{ee}(E_\nu)$ (see Figure 4.3), as the signal at each electron recoil energy is a convolution of different neutrino energies. Thus, large event numbers are necessary to distinguish between the two models for $P_{ee}(E_\nu)$.

4.1.2 Charged Current Reaction on ^{13}C

Another possible detection channel for ^{8}B neutrinos is the CC reaction of electron neutrinos on ^{13}C:

$$\nu_e + {}^{13}\mathrm{C} \rightarrow {}^{13}\mathrm{N} + e^- . \tag{4.8}$$

The recoil energy of the ^{13}N nucleus is of the order of a few keV and is therefore much smaller than the energy of the neutrino. Thus, it was neglected in the following. Hence, the neutrino energy can be reconstructed from the recoil energy of the electron T and the reaction threshold Q=2.22 MeV:

$$E_{\nu_e} = T + Q\ . \tag{4.9}$$

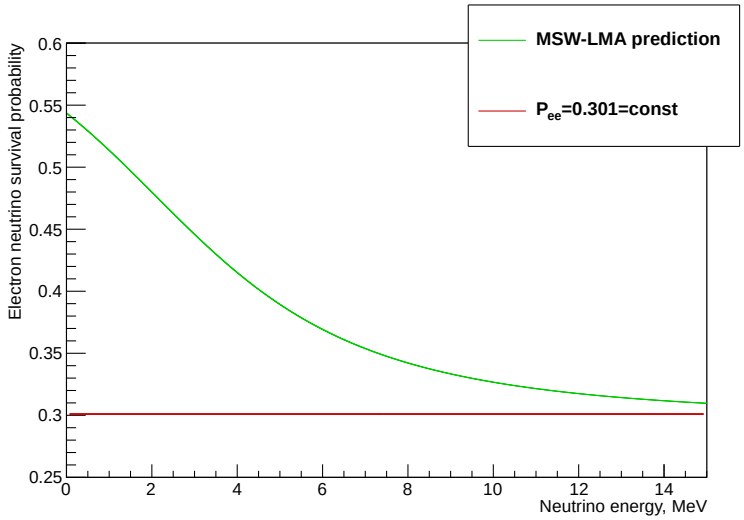

Figure 4.3: Comparison between P_{ee} according to the MSW-LMA prediction (denoted in green) and the $P_{ee} = \text{const}$ model (denoted in red), where $P_{ee} = \frac{\Phi_{CC}(^8B)}{\Phi_{NC}(^8B)} = 0.301 \pm 0.033$, according to the SNO measurements [28]. Note that the $P_{ee} = \text{const}$ model is always below the MSW-LMA prediction due to the uncertainties of the SNO measurements and of the MSW-LMA prediction, which are not depicted here.

The cross section can be precisely calculated from the decay time of ^{13}N [90]:

$$\sigma = 0.2167 \cdot 10^{-43}\,\text{cm}^2\,\frac{p_e E_e}{\text{MeV}^2} F(Z = 7, A = 13, E_e)\ , \tag{4.10}$$

where $E_e = E_\nu - 2.22\,\text{MeV} + m_e$ is the electron energy, p_e is the electron momentum and $F(Z = 7, A = 13, E_e)$ is the Fermi factor for ^{13}N. At 10 MeV, the cross section is $\sigma = 1.76 \cdot 10^{-42}\,\text{cm}^2$, which is about one order of magnitude larger than the cross section of the ES reaction. But the natural isotopic abundance of ^{13}C is only 1.07 % [90] and thus the number of electrons in the target volume is almost three orders of magnitude larger than the number of ^{13}C nuclei. Hence, the event rate of the ^{13}C channel is almost two orders of magnitudes lower than the event rate of the ES channel, which prevented the use of this channel in Borexino.
The ^{13}N nucleus, which was produced in reaction (4.8), decays with a life time of $\tau = 862.6\,\text{s}$ to ^{13}C:

$$^{13}N \rightarrow {}^{13}C + \nu_e + e^+\ . \tag{4.11}$$

The positron will annihilate with an electron after it has lost all its kinetic energy[4], emitting two 511 keV gammas. Hence, including the effects of the gamma

[4]There is also a small probability that the positron will annihilate before it has deposited all its kinetic energy.

quenching and the energy resolution of the detector, the reconstructed energy will be between 0.8 MeV and 2.2 MeV in 99.9 % of all cases.
The delayed coincidence of the prompt electron signal and the delayed positron signal from the ^{13}N decay can be used to suppress the background. As the life time of ^{13}N is quite long, an efficient background reduction is only possible if also the spatial coincidence between the neutrino event and the ^{13}N decay is used. Thus, a candidate event will only be tagged if three conditions are fulfilled:

- The energy of the delayed event is between 0.8 MeV and 2.2 MeV.
- The delayed event was detected within a time interval $\Delta t = a \cdot \tau(^{13}N)$.
- The distance between the prompt and the delayed event is less than $r = b \cdot \sigma_p$, where σ_p is the position resolution of the detector.

The positon resolution increases with the energy and at 1 MeV visible energy $\sigma_p \approx 10$ cm [62]. In order to simplify the analysis, it was assumed in the following that $\sigma_p = 10$ cm for all energies, which is a conservative assumption. The parameters a and b are free and can be varied for an optimal performance.
The detection efficiency $\epsilon(a, b)$, depends on the efficiency for the time ($\epsilon_t(a)$) and space cut ($\epsilon_s(b)$). Furthermore, the energy cut efficiency ($\epsilon_E = 99.9\,\%$) also needs to be considered, as the reconstructed energy can be outside of the delayed energy window, due to the finite energy resolution of the detector. Assuming that $\epsilon_t(a)$, $\epsilon_s(b)$ and ϵ_E are independent of each other, the detection efficiency can be expressed as:

$$\epsilon(a, b) = \epsilon_t(a) \cdot \epsilon_s(b) \cdot \epsilon_E \ . \tag{4.12}$$

The efficiency for the time cut is the probability that the ^{13}N nucleus decays within the time $\Delta t = a \cdot \tau(^{13}N)$:

$$\epsilon_t(a) = 1 - e^{-a} \ , \tag{4.13}$$

and the efficiency for the spatial cut is the probability that the distance between the prompt and the delayed event is less than $r = b \cdot \sigma_p$ [90]:

$$\epsilon_s(b) = \mathrm{erf}\left(\frac{b}{2}\right) - \sqrt{\frac{1}{\pi}} e^{-\frac{b^2}{4}} \ . \tag{4.14}$$

For a=3 and b=3, the detection efficiency is about 75 %. The resulting background suppression will be discussed in Section 4.2.
As the neutrino energy can be reconstructed from the kinetic energy of the electron (see equation (4.9)), the differential event rate is given by:

$$\frac{dR_{\nu_e}}{dE_\nu} = n(^{13}C) \cdot \Phi \cdot \lambda(E_\nu) \cdot P_{ee}(E_\nu) \tag{4.15}$$

where n(^{13}C) is the number of ^{13}C nuclei in the target volume, Φ is the solar neutrino flux, $\lambda(E_\nu)$ is the normalized spectral shape of the neutrino flux and $P_{ee}(E_\nu)$ is the energy dependent electron neutrino survival probability.
Due to the 2.2 MeV reaction threshold, the ^{13}C channel is only sensitive to ^{8}B and hep neutrinos. As the flux of the hep neutrinos is more than two orders of magnitude lower than the flux of the ^{8}B neutrinos, the contribution of the hep neutrinos to the ^{13}C channel is neglected in the following.
Analogous to the ES channel, 10^6 electron events were simulated with a differential event rate according to equation (4.15) and the event positions were homogeneously distributed over the whole usable target volume ($r < 13.5$ m and $|z| < 48.5$ m). Afterwards, the visible energy was reconstructed for each event, using the algorithm which was described in Section 3.2. Finally, the neutrino energy was determined from the visible energy by using equation (4.9).

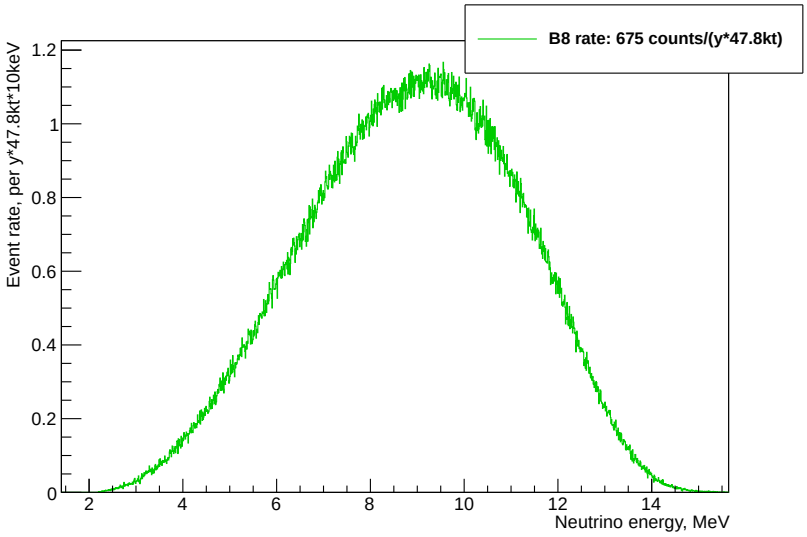

Figure 4.4: The reconstructed ^{8}B solar neutrino energy spectrum with $P_{ee}(E_\nu)$ according to the MSW-LMA prediction for the ^{13}C channel.

Figure 4.4 shows the resulting ^{8}B solar neutrino spectrum with $P_{ee}(E_\nu)$ according to the MSW-LMA prediction for the ^{13}C channel. Compared to the spectrum for the ES channel, a clear peak around ~ 10 MeV is visible. Due to the strong energy dependence of the cross section, the lower part of the ^{8}B spectrum is suppressed. About 675 events per year are expected in the target volume, which is almost two orders of magnitude less than for the ES channel, due to the low ^{13}C abundance. Thus, a high statistic measurement is not possible with this channel, but there are still enough events to measure the unconvoluted shape of the oscillated ^{8}B

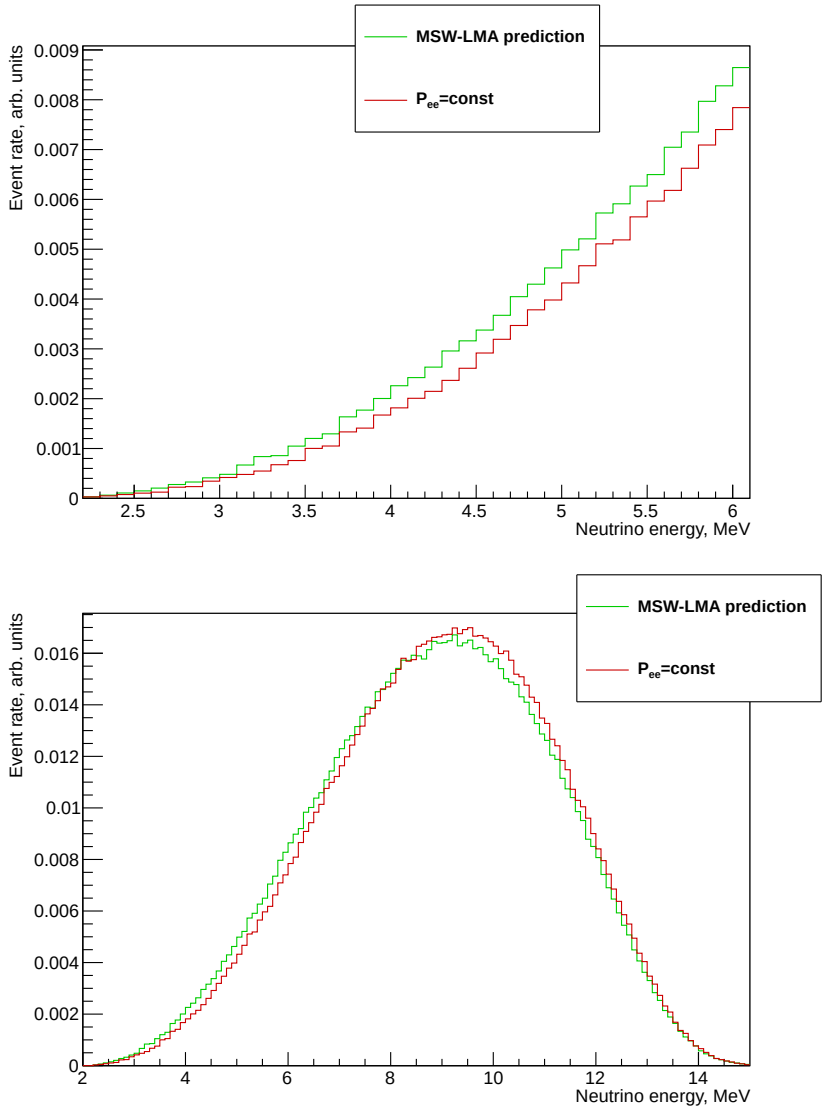

Figure 4.5: The normalized ^{8}B spectrum for P_{ee}=const (denoted in red) and P_{ee} (denoted in green) according to the MSW-LMA prediction for the ^{13}C channel. The upper plot shows a zoom into the low energy region, where the difference between P_{ee}=const model and the MSW-LMA prediction is maximal.

spectrum. Hence, using the known ^{8}B flux from the SNO measurements (see Section 1.5.2), an energy dependent measurement of P_{ee} is possible.
Figure 4.5 shows the normalized ^{8}B spectrum for $P_{ee}(E_\nu)$=const and $P_{ee}(E_\nu)$ according to the MSW-LMA prediction. Compared to the ES channel, the difference between the two spectra is larger at low energies, as the ^{8}B spectrum is unconvoluted[5]. But due to the higher statistics, the ES channel is still better suited to distinguish between the two models (see Section 4.4).

4.2 Simulation of Background Spectra

Due to the low expected ^{8}B event rate and because there is no distinctive event signature for the ES channel, backgrounds are a crucial issue for the study of ^{8}B neutrinos. Furthermore, although the delayed coincidence signature of the ^{13}C channel allows a suppression of the background, the accidental coincidences can not be neglected because of the long life time of ^{13}N.
For the ES channel, there are three different types of background sources: cosmogenic radioisotopes, which are produced by cosmic muons traversing the target volume, intrinsic radioactive background and external gamma rays from the tank, the PMTs and the LCs (see Section 4.2.1, 4.2.2, 4.2.3).
The accidental coincidence of these backgrounds and of ES interactions of solar neutrinos provide a background for the ^{13}C channel (see Section 4.2.4).

4.2.1 Cosmogenic Radioisotopes

Cosmogenic radioisotopes are produced inside the target volume by muon-induced spallation reactions on the carbon nuclei. The subsequent decays of these radioisotopes pose a background for the ^{8}B neutrino detection. As the majority of these radioisotopes have a lifetime of $\sim 1\,$s or shorter [29, 51], they can be easily tagged by looking for the coincidence with a cosmic muon, without introducing a large dead time. The remaining cosmogenic radioistopes are ^{11}C (β^+, $\tau = 29.4\,$min), ^{10}C (β^+, $\tau = 27.8\,$s) and ^{11}Be (β^-, $\tau = 19.9\,$s) (see Table 4.2).
The spectra of these radioisotopes were determined in two steps. First of all, the spectral shapes were simulated with the GEANT4 based Monte Carlo simulation. Therefore, 10^6 decays of each radioisotope were simulated in the target volume, using the G4Radioactive module [76]. Afterwards, the rates observed in the Borexino experiment (R_B) [29, 27][6] were scaled to obtain the expected rates

[5] The spectrum is of course still convoluted with the detector resolution.

[6] After the analysis which is presented in this Chapter was finished, new results for Borexino were published [47]. As the new results are in agreement with the old ones, they would not alter the results of the study which is presented here.

Isotop	Decay Type	Q-Value [MeV]	Life time	Rate [cpd/ kt]
^{11}C	β^+	2.0	29.4 min	54
^{10}C	β^+	3.7	27.8 s	1.0
^{11}Be	β^-	11.5	19.9 s	$6.4 \cdot 10^{-2}$

Table 4.2: List of the cosmogenic radioisotopes with life times above 2 s.

for the Pyhäsalmi location (R_P):

$$R_P = R_B \cdot \frac{\Phi_P^\mu}{\Phi_B^\mu} \ , \tag{4.16}$$

where $\Phi_P^\mu = 0.235\,m^{-2}h^{-1}$ is the expected muon flux at 4 km w.e. depth [53] and $\Phi_B^\mu = 1.22\,m^{-2}h^{-1}$ is the muon flux at the location of the Borexino detector [44]. No scaling was applied for the different mean muon energies and scintillator compositions as they have a negligible effect on the rates [71].

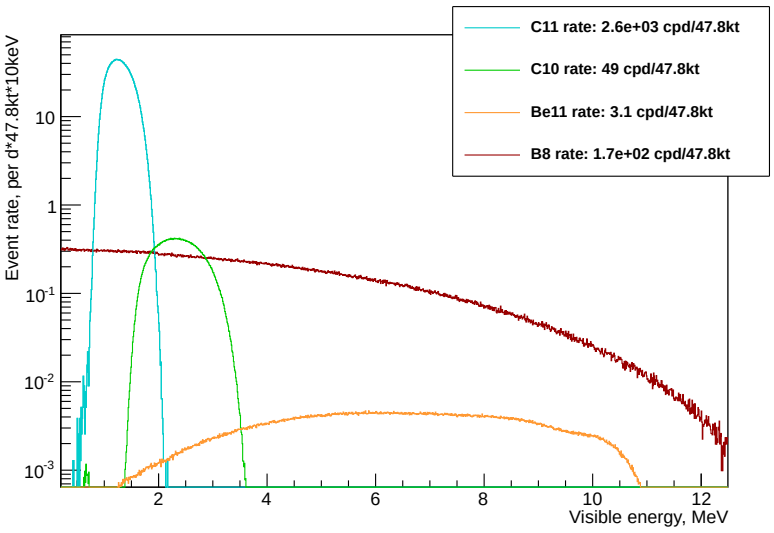

Figure 4.6: The simulated background spectra for the cosmogenics isotopes ^{11}C, ^{10}C and ^{11}Be. Furthermore, the expected ^{8}B spectrum is shown for comparison.

Figure 4.6 shows the resulting cosmogenic background spectra. The largest contribution is from ^{11}C which surpasses the ^{8}B rate by almost two orders of magnitude. Due to the long life time of ^{11}C, an efficient tagging of ^{11}C based only on a time coincidence with the parent muon would introduce a too large dead time. It has been shown in Borexino that the ^{11}C background can be reduced by a factor of

Isotop	Decay Type	Q-Value [MeV]	Life time	Rate [cpd/ kt]
^{214}Bi	β^- (99.98 %)	3.3	28.7 min	17.2
^{214}Bi	α (0.02 %)	5.6	28.7 min	$3.4 \cdot 10^{-3}$
^{208}Tl	β^-	5.0	4.4 min	0.16

Table 4.3: List of the intrinsic radioisotopes with Q-Values above 2.0 MeV.

10 based on a Three-Fold Coincidence (TFC) of cosmic muons, neutrons and ^{11}C decays that uses both time and spatial information [17]. But as the ^{11}C signal would still be one order of magnitude larger than the ^{8}B signal, this reduction is not enough. Thus, the ^{8}B spectrum can not be measured below 2 MeV.
The second largest background is caused by ^{10}C, which surpasses the ^{8}B signal between $\sim$ 2 MeV and $\sim$ 3 MeV by almost a factor of two. As there is a small probability that the ^{10}C nucleus decays via an electron capture instead of a β^+ decay, a small side peak around 0.7 MeV is also visible. Due the different spectral shape of ^{10}C and ^{8}B, this background could be reduced statistically by a spectral fit. But it is also possible to tag ^{10}C on an event by event basis. ^{10}C is produced either directly by a cosmic muon, or in an electromagnetic or hadronic shower that was induced by a muon. Thus, the ^{10}C event can not be far away from the muon track. Hence, it is sufficient to veto a cylinder with 2 m radius around a muon track for $\Delta t = 4 \cdot \tau(^{10}\mathrm{C}) = 111.2\,\mathrm{s}$ to reduce the ^{10}C rate by a factor of 50, so that the ^{10}C spectrum is always at least one order of magnitude below the ^{8}B spectrum. Furthermore, by analyzing the vetoed data it is possible to determine the remaining ^{10}C rate. Hence, the ^{10}C background can be further reduced by a statistical subtraction. As only a small volume around each muon is vetoed, the dead time amounts to an acceptable level of about 9.1 %. This cut also reduces the ^{11}Be background by more than two orders of magnitude to a negligible level of 0.01 counts per day.
Figure 4.7 shows the final cosmogenic background spectra after this cut is applied.

4.2.2 Instrinsic Radioactive Background

Besides cosmogenic radioisotopes, there is also an intrinsic background from radioactive impurities in the scintillator. The level of radiopurity that will be reached in LENA depends on many factors and is hard to predict. Hence, in the following it will be assumed that the radiopurity levels of Borexino are reached[7].

[7]Note that the radiopurity levels of the first data taking phase of Borexino are used and that the current radioactive background rates are much lower due to the several purification campaigns.

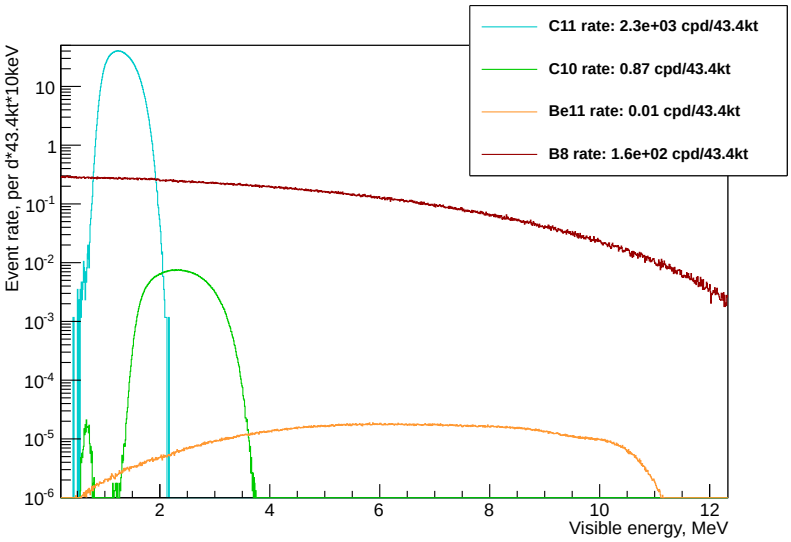

Figure 4.7: The simulated background spectra for the cosmogenics isotopes ^{11}C, ^{10}C and ^{11}Be after a time and space cut around each cosmic muon track is applied. Furthermore, the expected ^{8}B spectrum is shown for comparison.

The only intrinsic radioisotopes in the Borexino detector with a Q-Value above 2 MeV are ^{214}Bi (^{238}U chain, Q=3.3 MeV) and ^{208}Tl (^{232}Th chain, Q=5.0 MeV) (see Table 4.3) [29]. ^{214}Bi decays with 99.98 % branching ratio to ^{214}Po, which subsequently decays with a life time of $\tau = 237\,\mu$s to ^{210}Pb [91]. This delayed coincidence between the ^{214}Bi and the ^{214}Po decay can be used to tag the ^{214}Bi events. Therefore, this background can be reduced to a negligible level and is not considered anymore in the following. As the lifetime of ^{214}Po is below 1 ms, this cut reduces the detection efficiency only by an insignificant amount.

Figure 4.8 shows the simulated ^{208}Tl spectrum. As it was done for the simulation of the cosmogenic background, 10^6 events were simulated in the target volume, using the G4Radioactive module [76]. ^{208}Tl β^- decays under the emission of at least two gammas with a minimum combined energy of 3.2 MeV [91]. Thus, the typical β spectrum is shifted by $\sim$ 3.2 MeV. Due to the large range of the gammas, there is a small chance they do not deposite their whole energy in the target volume. This creates the small side peak, that is visible between $\sim$ 1 MeV and $\sim$ 3 MeV and vanishes when ^{208}Tl is simulated in the center of the detector, so that all gammas are detected.

The ^{208}Tl background surpasses the ^{8}B signal between about 3.5 MeV and 4.5 MeV by up to 50 %. Due to the different shapes, it is possible to separate the ^{208}Tl spectrum from the ^{8}B spectrum by a spectral fit. But there is also another, more

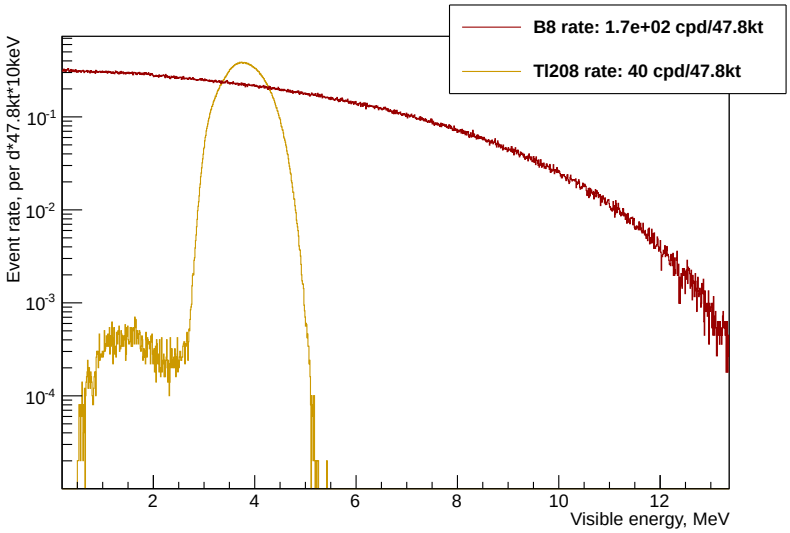

Figure 4.8: The simulated ^{208}Tl spectrum. Furthermore, the expected ^{8}B spectrum is shown for comparison.

precise possibility. ^{208}Tl is produced by the α decays of ^{212}Bi. ^{212}Bi also decays with a branching ratio of 64 % into ^{212}Po, which subsequently decays with a life time of $\tau = 0.4\,\mu$s to ^{208}Pb. This delayed coincidence can be used to measure the amount of ^{212}Bi and therefore also the ^{208}Tl rate. As more than $2 \cdot 10^4$ Bi-Po coincidences are expected per year, the ^{208}Tl background can be determined with less than 1 % uncertainty. Thus, ^{208}Tl can be subtracted statistically from the measured spectrum.

4.2.3 External Gamma Background

Gamma rays from radiactive impurities outside of the target volume can enter the scintillator volume and provide a background. The dominating contributions come from the concrete tank, the PMTs and the LCs.

Gamma Sources

The main sources for gamma decays outside of the target volume are ^{40}K, ^{238}U, ^{232}Th and the corresponding daugther nuclides of ^{238}U and ^{232}Th [92, 52].
^{40}K decays with 10.7% probability to ^{40}Ar (β^+, EC) and emits a 1.46 MeV gamma, otherwise it decays to ^{40}Ca (β^-) without emitting a gamma [91]. Above 250 keV, only ^{228}Ac, ^{212}Pb, ^{212}Bi and ^{208}Tl contribute to the background from the ^{232}Th

chain, with ^{208}Tl being the dominant one with a gamma energy of 2.6 MeV. From the ^{238}U chain, only ^{234}Pa, ^{214}Pb and ^{214}Bi contribute to the background [93].

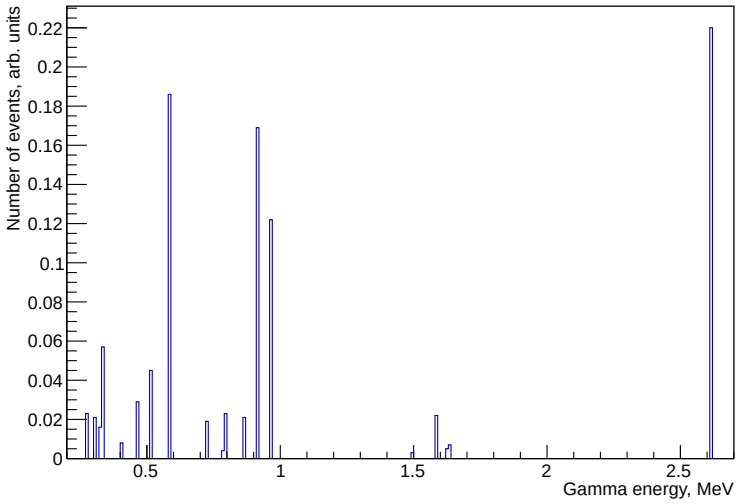

Figure 4.9: Normalized gamma spectrum of the ^{232}Th chain above 250 keV.

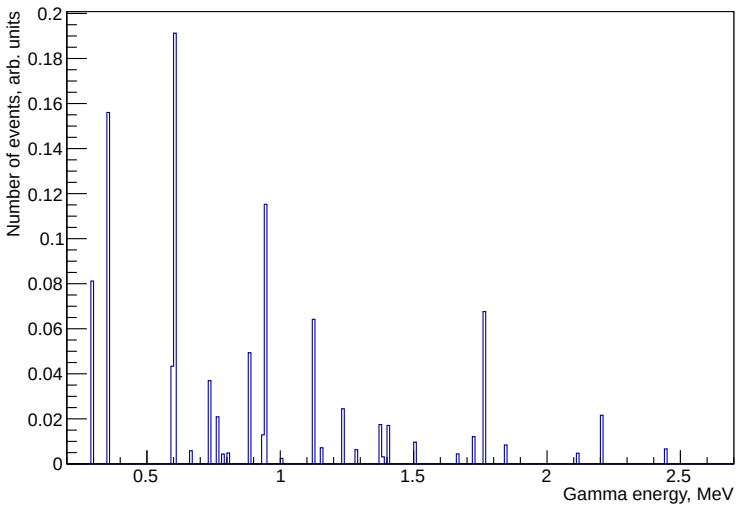

Figure 4.10: Normalized gamma spectrum of the ^{238}U chain above 250 keV.

Figure 4.9 and 4.10 show the gamma spectrum for the ^{232}Th chain and the ^{238}U chain, assuming that the decay chains are in equilibrium. While the majority

	^{40}K	^{238}U chain	^{232}Th chain
Tank	13 MBq	1.1 GBq	178 MBg
PMTs	14 kBq	229 kBq	24 kBg
LCs	0.86 kBq	13 kBq	41 kBg

Table 4.4: The gamma rates above 250 keV of the different sources.

of the gammas are below 2 MeV, there is also a small fraction above the 2 MeV detection threshold for ^{8}B neutrinos (ES channel). These gammas are a dangerous background as they have large range. Furthermore, they provide a background in the transition region between vacuum and matter dominated oscillations (see Section 1.2).

Additionally, the gammas below 2 MeV pose a background for the ^{13}C channel, and need to be considered for the calculation of the accidental background rate (see Section 4.2.4). Thus, for a test of the MSW-LMA prediction and a possible detecton of new physics it is crucial to suppress the external gamma background.

Table 4.4 shows the integral gamma rates above 250 keV for the different sources. For the tank, the radioactive impurity level of the concrete that was used at the LNGS was assumed [52]. A tank mass of $7.21 \cdot 10^6$ kg was assumed, which corresponds to a 100 m height tank with 32 m diameter, 30 cm wall thickness and a concrete density of $2.37 \frac{\mathrm{g}}{\mathrm{cm}^3}$. In reality, the tank wall will be 60 cm thick and cylindrical cavities with 30 cm diameter will be left open to leave space for installation (e.g. cooling or active leak proving). Thus, the tank mass and therefore the gamma activity will be larger than what was assumed for this study. But due to the self-shielding of the concrete tank, the resulting gamma rate in the target volume is only underestimated by a few percents. Furthermore, this effect is at least partly compensated because the stainless steel sheets, which are welded to the tank walls, are not included in the simulation.

For the PMTs and LCs, it was assumed that 71642 8-inch PMTs are used and the radioactive impurity levels were taken from the Borexino experiment[8] [92].

Due to the large mass, the gamma activity from the concrete tank is about four orders of the magnitude larger than the gamma activity from the PMTs and the LCs. In the current design of LENA, this is the reason to install the PMTs 2 m in front of the tank walls and to optically separate the volume behind the PMTs from the detection volume (see Section 2.1). The gamma activity of the PMTs and the LCs is comparable, though the ^{232}Th activity is larger for the LCs.

[8]Note that materials with a higher radiopurity level can possibly be used for the LCs in LENA, as LAB is used as liquid scintillator instead of pseudocumene.

Simulation Setup

Because of the large gamma activity, computation time is a critical issue. A full simulation of all gammas that are emitted from the tank during one day would take years of computation time, even if no scintillation light is simulated.

Thus, the simulation was splitted into two parts to save computation time. In the first step, the gammas were started at their corresponding source and tracked until they reached the target volume or were absorbed in the buffer volume. If gammas from the tank were simulated, they were started at a random position in the tank, to include the self-shielding effect of the tank. For the simulation of the gamma background from the PMTs, a random PMT was chosen and the gammas were started at the photocathode, as it is the dominating radioactive source in the PMT. If gammas from the LCs were simulated, a random LC was chosen and the gammas were started at a random position in the corresponding LC.

The gamma energy was chosen according to the gamma spectrum of ^{40}K, ^{232}Th or ^{238}U. The gamma was emitted isotropically, but it was not tracked when it was directed outwards to the water tank, as the probability to reach the target volume is very low in this case. Thus, the simulation was speed by up a factor of two. To further reduce the computation time, the produced secondary particles were not tracked.

If the gamma reached the target volume, the simulation of the event was stopped and the position, energy and momentum direction of the gamma were saved. Furthermore, the initial position, energy and momentum direction of every produced secondary particle were also saved.

In the second step, the gamma and the secondary particles were started at the saved positions, and both were tracked until they were stopped. The visible energy of the event was reconstructed (see Chapter 3) and the photon barycenter was also calculated. Afterwards the photon barycenter position was smeared with a gaussian with a standard deviation according to the energy dependent position resolution [62]. Including the position resolution of the detector is important, as the number of background events decreases with the radius. Thus, the spill-in effect of gammas, which were produced outside of a certain fiducial volume but were reconstructed inside of the volume, is greater than the spill-out effect of gammas, which were produced inside of a certain fiducial volume but were reconstructed outside of the volume. Hence, the position resolution has an effect on the effective gamma range.

As only gammas which reached the target volume were simulated in the last step, the computation time was reduced by up to four orders of magnitude, depending on the gamma source.

Results

Figure 4.11 shows the resulting external gamma background spectrum for 13.5 m fiducial volume radius ($|z| < 48.5$ m) and the contribution of the indivual sources. Below ~ 2 MeV, the background from the PMTs dominates, due to the large ^{238}U activity and the short distance to the target volume.
Above ~ 2.3 MeV, the LCs have the largest contribution, because of the larger ^{232}Th activity. The decay of ^{208}Tl, which is part of the ^{232}Th chain, causes the peak at about 2.5 MeV, although the gamma energy is 2.6 MeV. The reason for this effect is that the gamma loses its energy mainly via multiple compton scatters. Thus, the energy is transferred to multiple electrons, which have a low energy and are therefore quenched (see Section 3.1.2).
Contrary to the PMTs and LCs, only the ^{208}Tl peak at about 2.5 MeV is visible in the background spectrum from the tank. The reason for this is that there is a large probability that the gammas compton scatter in the buffer liquid before they enter the scintillator volume. Thus, the gamma peaks, except the ^{208}Tl peak, are smeared out and are no longer visible. The ^{208}Tl peak is visible because it has the largest energy and is therefore not covered by compton scattered gammas. Furthermore, it also has the largest range due its high energy. This loss of energy in the buffer volume is also responsible for the rise of the gamma background rate below ~ 0.4 MeV.
Compared to the ^{8}B rate, the gamma background is almost six orders of magnitude larger. Thus, a fiducial volume cut has to be applied to reduce the external gamma background. As the simulated statistics were limited for smaller fiducial volumes, another simulation with a further optimized setup was performed. In the first step, the gammas were tracked until they reached a fiducial volume with 13 m radius ($|z| < 48.0$ m) and no scintillation light was generated in the target volume. Again, only the gammas which reached the fiducial volume were simulated in the second step. As the produced secondary particles were also simulated in the second step, the scintillation of the event is simulated correctly. But as a full detector simulation was only performed for the gammas that reached the fiducial volume, the computation time could be further reduced by more than two orders of magnitude.
Figure 4.12 shows the external gamma background spectrum for 12 m fiducial volume radius. Compared to Figure 4.11, the gamma background below ~ 1 MeV ist strongly supressed and the ^{208}Tl peak at 2.5 MeV is clearly dominating. The reason for this is that the mean free path length of the gamma increases with the energy. Thus, low energetic gammas are stronger suppressed by the additional 1.5 m shielding. Overall, the gamma background rate was reduced by about three orders of magnitude, which is still too high to detect ^{8}B neutrinos below 3 MeV.
Figure 4.13 shows the external gamma background rate for different fiducial vol-

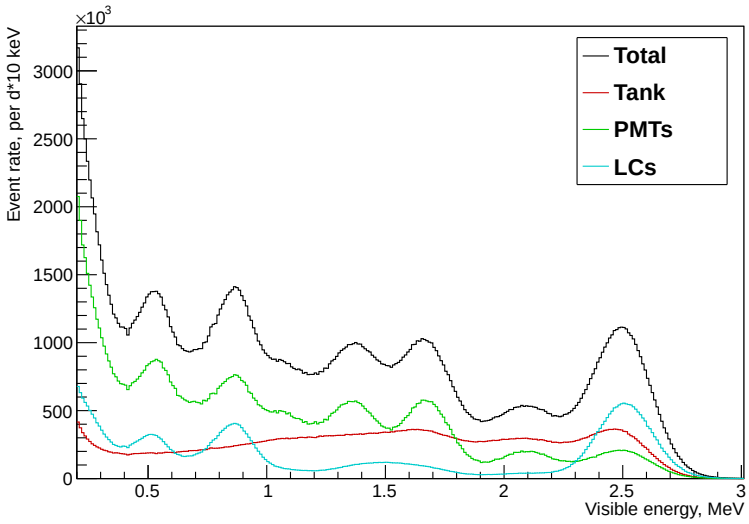

Figure 4.11: The external gamma background spectrum for 13.5 m fiducial volume radius. Besides the total background (denoted in black), the individual contributions from the tank (denoted in red), the PMTs (denoted in green) and the LCs (denoted in cyan) are also depicted.

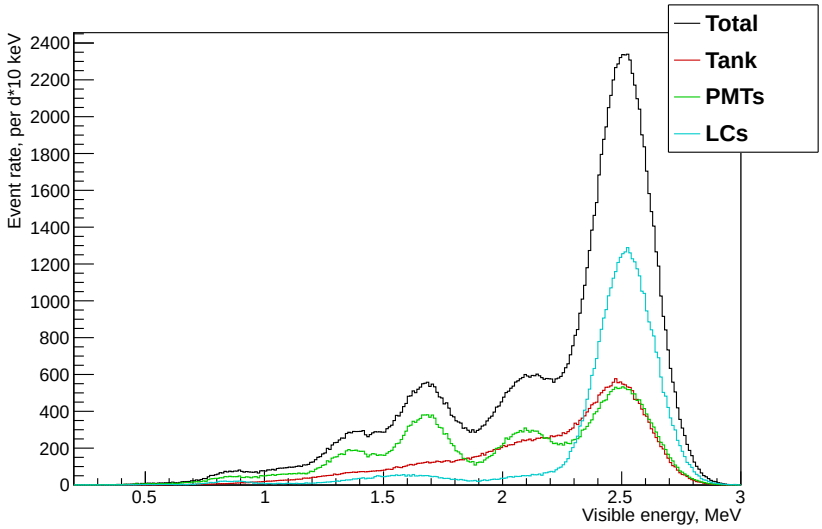

Figure 4.12: The external gamma background spectrum for 12 m fiducial volume radius. Besides the total background (denoted in black), the individual contributions from the tank (denoted in red), the PMTs (denoted in green) and the LCs (denoted in cyan) are also depicted.

umes, ranging from 10.5 m to 12 m radius. Even at 10.5 m fiducial volume radius, the gamma background is still higher than the ^{8}B signal. Below 10.5 m, the statistics was too small to calculate the gamma background rate precisely. Thus, the gamma background rate was fitted with an exponential function, so that the rate can be extrapolated to smaller fiducial volume radii. The goodness of the fit was $\chi^2/\text{ndf} = 6.336/5$, which shows that this is a good approximation. Using this extrapolation, the external gamma background rate at 9 m fiducial volume radius was calculated to be below 1 count per day.

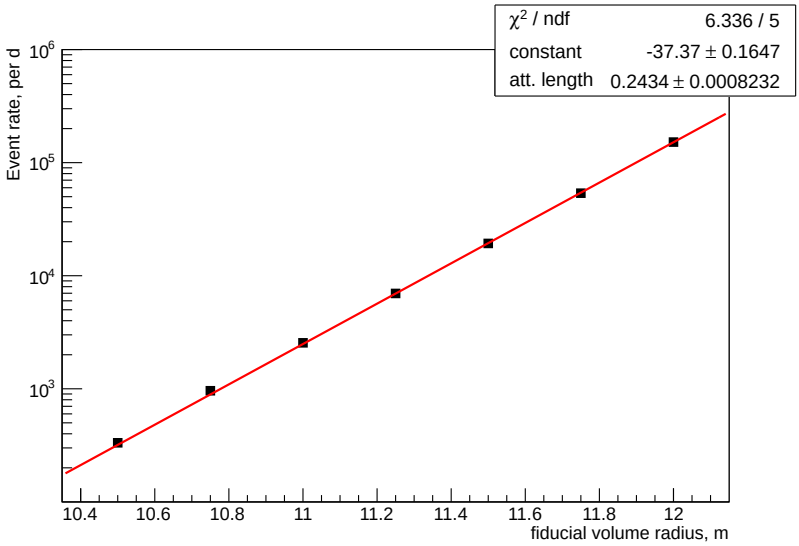

Figure 4.13: The external gamma background rate, depending on the fiducial volume radius. Furthermore, a fit with an exponential function is depicted in red.

This is more than one order of magnitude less than the ^{8}B signal. Thus, the fiducial volume radius was chosen to be 9 m for the analysis of the ^{8}B spectrum below 3.5 MeV and the external gamma background was neglected in the following. This cut reduced the fiducial mass from 47.8 kt to 19.3kt. Above 3.5 MeV, the fiducial volume radius can be increased to 13.5 m[9], as no external gamma background is present at these energies.

4.2.4 Accidental Coincidences

The ^{13}C channel has a destinctive event signature of a prompt signal which is followed by the decay of ^{13}N with $\tau = 862.6$ s. Thus, the background can be

[9] At larger radii, the photoelectron yield is too inhomogenous (see Section 3.2) to reconstruct the energy precisely.

suppressed by looking for the coincidence in space and time of the prompt and the delayed signal. But due to the low event rates and the long life time of ^{13}N, accidental coincidences of the different background sources can not be neglected. Background source are cosmogenic radioisotopes (see Section 4.2.1), radioactive impurities in the scintillator (see Section 4.2.2), external gamma rays (see Section 4.2.3) and the ES interactions of solar neutrinos. Two background events are tagged as an ^{13}C candidate event if the time between the events is less than $3\tau(^{13}\mathrm{N}) = 0.72\,\mathrm{h}$, the distance between the reconstructed positions is less than $3\sigma_\mathrm{p} = 30\,\mathrm{cm}$ and energy of the delayed event is between 0.8 MeV and 2.2 MeV. If the position of the prompt and the delayed event is uncorrelated, the probability for an accidental coincidence is[10]:

$$\mathrm{P_{uncorr.}} = \mathrm{R_{del.}} \frac{4}{3}\pi \left(3\sigma_\mathrm{p}\right)^3 \rho \cdot 3\tau(^{13}\mathrm{N}) \;, \tag{4.17}$$

where $\mathrm{R_{del.}}$ is the rate in the delayed energy window and $\rho = 0.86\,\mathrm{g/cm^3}$ is the density of the scintillator. If the prompt event is not a gamma background event, the position of the prompt and the delayed event is always uncorrelated[11]. Using a fiducial volume with a radius of 11 m, the background rate in the delayed energy window can be calculated from the individual background sources:

$$\mathrm{R_{del}} = \mathrm{R_{del}^{ext.\gamma}} + \mathrm{R_{del}^{int.rad.}} + \mathrm{R_{del}^{cosm.}} + \mathrm{R_{del}^{\nu,ES}} = 99.3\,\frac{\mathrm{cpd}}{\mathrm{kt}} \;, \tag{4.18}$$

where $\mathrm{R_{del}^{ext.\gamma}}$ is the external gamma rate, $\mathrm{R_{del}^{int.rad.}}$ instrinsic radioactive background rate, $\mathrm{R_{del}^{cosm.}}$ is the cosmogenic radioisotopes rate and $\mathrm{R_{del}^{\nu,ES}}$ is the ES rate of solar neutrinos in the delayed energy window (see Table 4.5). Using equation (4.17), the probability for an accidental coincidence is $\mathrm{P_{uncorr.}} = 2.89 \cdot 10^{-4}$. Thus, the intrinsic radioactive background, the cosmogenic background and the background from ES interactions of solar neutrinos are suppressed by almost four orders of magnitude.
If the prompt event is a gamma background event, one has to distinguish between two cases. If the delayed event is not a gamma, the background rate in the delayed energy window is:

$$\mathrm{R_{del}} = \mathrm{R_{del}^{int.rad.}} + \mathrm{R_{del}^{cosm.}} + \mathrm{R_{del}^{\nu,ES}} = 85.4\,\frac{\mathrm{cpd}}{\mathrm{kt}} \;, \tag{4.19}$$

and the probability for an accidental coincidence can be calculated with equation (4.17) to be $\mathrm{P_{uncorr.}}(\gamma) = 2.49 \cdot 10^{-4}$.

[10] In the following, the approximation $\mathrm{e^{-x}} \approx 1 - \mathrm{x}$ was used.

[11] It is also possible to have a correlated background if two cosmogenic isotopes are produced close to each other by one traversing cosmic muon. But as the probability for this case is very low, it was neglected in the following.

Background source	Rate [cpd/kt]
Cosmogenic radioisotopes	53.9
Intrinsic radioactivity	17.7
External gammas	13.9
ES of solar neutrinos	13.8

Table 4.5: The background rates in the delayed detection window between 0.8 MeV and 2.2 MeV.

In case that both events are due to gamma background, the probability for an accidental coincidence $P_{corr.}(\gamma)$ is much higher, as the gamma events are not homogenously distributed over the target volume (see Figure 4.13). Hence, $P^{\gamma}_{corr.}(\vec{x})$ depends on the position $\vec{x}$ of the prompt event:

$$P^{\gamma}_{corr.}(\vec{x}) = 4\pi\rho \cdot 3\tau(^{13}N) \cdot \int R^{ext.\gamma}_{del}(\vec{r})\Theta(3\sigma_p - |\vec{x} - \vec{r}|)d\vec{r} \qquad (4.20)$$

where $R^{ext.\gamma}_{del}(\vec{r})$ is the simulated position dependent gamma background rate and $\Theta(x)$ is the heavyside function. Averaging over all positions inside a fiducial volume with 11 m radius, the probability for an accidental coincidence between two gamma events was calculated to be $P_{corr.}(\gamma) = 2.62 \cdot 10^{-3}$. Thus, the external gamma background is only suppressed by a factor of about 400, which is almost one order of magnitude less than for the other backgrounds.
Figure 4.14 shows the total accidental background spectrum for the ^{13}C channel. Note that the energy was reconstructed according to Section 4.1.2. Below about 5 MeV neutrino equivalent energy, the accidental background is more than two orders of magnitude larger than the ^{8}B signal, which dominates above $E_\nu \approx 5$ MeV. The dominating background source between $E_\nu \approx 3$ MeV and $E_\nu \approx 5$ MeV are external gammas. This background could be suppressed by using a smaller fiducial volume, which would also reduce the background above $E_\nu \approx 5$ MeV, as the background rate in the delayed energy window and thus the probability for an accidental coincidence would be reduced. But this would reduce the already limited statistics of the ^{13}C channel even further. Thus, the fiducial volume was set to 11 m for the following analysis, as a compromise between background level and signal statistics. Below $E_\nu \approx 3$ MeV, ES interactions of ^{7}Be solar neutrinos and the alpha decays of ^{210}Po are the largest background. The small peak at $E_\nu \approx 6$ MeV is due to intrinsic decays of ^{208}Tl. Apart from this background, the ES interactions of ^{8}B solar neutrinos and ^{11}Be cosmogenic radioisotopes are the largest backgrounds above $E_\nu \approx 5$ MeV.
Above about 5 MeV neutrino equivalent energy, the ^{8}B signal is at least one order of magnitude larger than the accidental background. Hence, a measurement of the

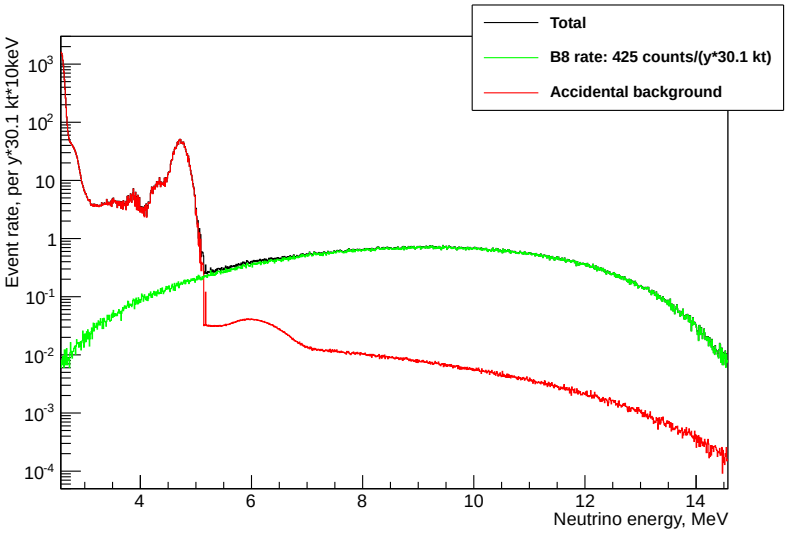

Figure 4.14: The accidental background spectrum for the ^{13}C channel, using a fiducial volume with 11 m radius. Furthermore, the expected ^{8}B spectrum is shown for comparison. Note that the energy of both the background and the ^{8}B events was reconstructed according to Section 4.1.2.

^{8}B neutrinos with the ^{13}C channel is possible above 5 MeV, but is prevented at lower energies by the accidental background.

4.3 Analysis Procedure

Using the simulated neutrino and background spectra according to the MSW-LMA prediction (see Section 4.1 and 4.2), 10^5 five year long measurements of the ^{8}B neutrino spectrum were simulated with the ROOT package [94]. Afterwards, the simulated data was analyzed independently for the ^{13}C channel (see Section 4.3.1) and the ES channel (see Section 4.3.3). Finally, the results for both channels were combined (see Section 4.3.3) to maximize the sensitivity of the analysis.

4.3.1 ^{13}C Channel

The fiducial volume radius was set to 11 m to suppress the external gamma background to an acceptable level, without reducing the already limited statistics too much. For each simulated measurement, the expected accidental background spectrum was substracted from the simulated spectrum of the ^{13}C channel to get the ^{8}B spectrum. This subtraction is possible as the accidental background spectrum

can be measured independently by looking for events which do not fulfill the space and time coincidence requirement. While systematic errors of the background measurement cancel, the statistical error of the background measurement introduces a systematic error to the measurement of the ^{8}B spectrum. But as the statistics is much larger for the events which are off coincidence, this systematic error is much smaller than the statistical error of the ^{8}B measurement. Hence, it is neglected in the following.
Subsequently, the measured ^{8}B spectrum is divided by the expected unoscillated spectrum to get the energy dependent survival probability, without considering the uncertainty of the expected ^{8}B rate. In the last step, the survival probility is fitted with the MSW-LMA prediction and with a constant, using a χ^2 minimization. The MSW-LMA prediction was scaled with a free parameter, which was determined by the fit and the value of the constant was also not restricted. Thus, the analysis is only sensitive to the shape of P_{ee} and not to the absolute value. Hence, the uncertainty of the expected ^{8}B rate does not have any effect on the sensitivity of this analysis.
Figure 4.15 shows the results for one example measurement. While an indication for an upturn at 5 MeV is visible, it is statistically not significant enough to exclude the $P_{ee} = \text{const}$ hypothesis, due to the low statistics of the ^{13}C channel. Overall, the average exclusion significance is below $1\,\sigma$.

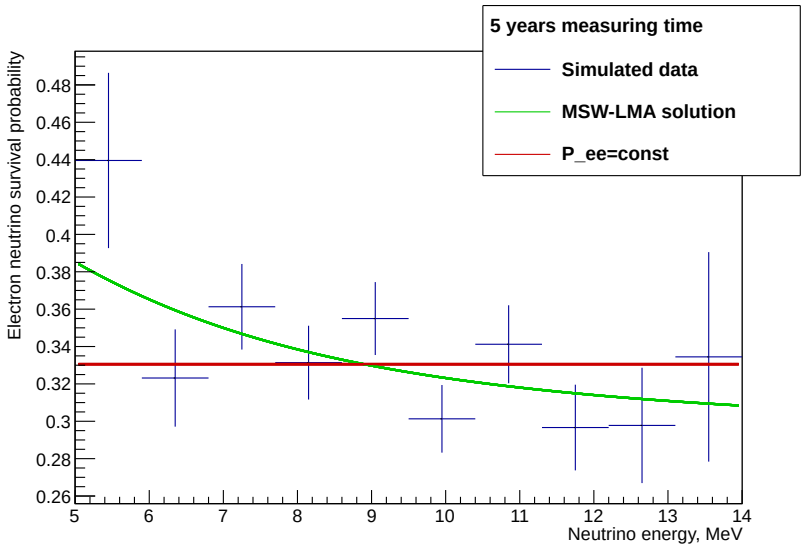

Figure 4.15: The measured electron neutrino survival probability after 5 years, using the ^{13}C channel. Furthermore, a fit with the MSW-LMA prediction (depicted in green) and with $P_{ee} = \text{const}$ (depicted in red) is shown.

4.3.2 Elastic Scattering Channel

Two different fiducial volumes were used in the analysis of the simulated data. For electron recoil energies between 1.9 MeV and 3.5 MeV, the fiducial volume radius was set to 9 m to reduce the external gamma background (see Section 4.2.1) and for higher energies the full fiducial volume with a radius of 13.5 m was used to maximize the statistics[12].

For the ES channel, it is not possible to directly calculate P_{ee} from the measured ^{8}B spectrum, as the neutrino energy can not be reconstructed on an event per event basis. Thus, the simulated spectrum was fitted with the expected spectrum according to the MSW-LMA prediction and the $P_{ee} = \text{const}$ hypothesis, using a χ^2 minimization, to distinguish between the two models. For both fits, the ^{8}B rate and the corresponding background rates were left as fit parameters.

As the contributions of the different background can be measured independently (see Section 4.2.1 and 4.2.2), this information was included into the χ^2 function by adding so-called pull terms [95]:

$$\chi^2_{\text{tot}} = \chi^2 + \chi^2_{\text{pull}} \tag{4.21}$$

$$\chi^2_{\text{pull}} = \sum_{\text{j=1}}^{\text{k}} \frac{(\lambda_{\text{j}} - \mu_{\text{j}})^2}{\sigma^2_{\lambda_{\text{j}}}} \ , \tag{4.22}$$

where k is the number of parameters with prior information, λ_j is the value of the parameter j, μ_j is the expected value of the parameter j and σ_{λ_j} is the uncertainty of the parameter j.

The expected uncertainties of the background rates are shown in Table 4.6. The uncertainties of the cosmogenic radioisotope rates were taken from the KamLAND (^{10}C and ^{11}Be) [51] and the Borexino experiment (^{11}C) [27]. The uncertainty of the hep rate was taken from [23] and the uncertainty of the ^{208}Tl background was estimated from expected number of Bi-Po coincidences (see Section 4.2.2).

Figure 4.16 shows the results of the fit for one example measurement. Above $\sim$ 3 MeV visible energy, the data is consistent with both the MSW-LMA prediction and with the $P_{ee} = \text{const}$ hypothesis. But below $\sim$ 3 MeV, the MSW-LMA prediction is clearly favored, which shows the importance of measuring the ^{8}B spectrum below 3 MeV, which is not possible with current WC and LS detectors.

[12] The other part of the target volume can not be used for physics analysis, as the photo electron yield changes to much over short distances in this part of the detector, which prevents a precise energy reconstruction (see Section 3.2).

Background	Rel. uncert. of the rate
hep	20 %
^{208}Tl	1 %
^{10}C	10 %
^{11}C	0.7 %
^{11}Be	20 %

Table 4.6: The expected uncertainties of the background rates for the ^{8}B measurement.

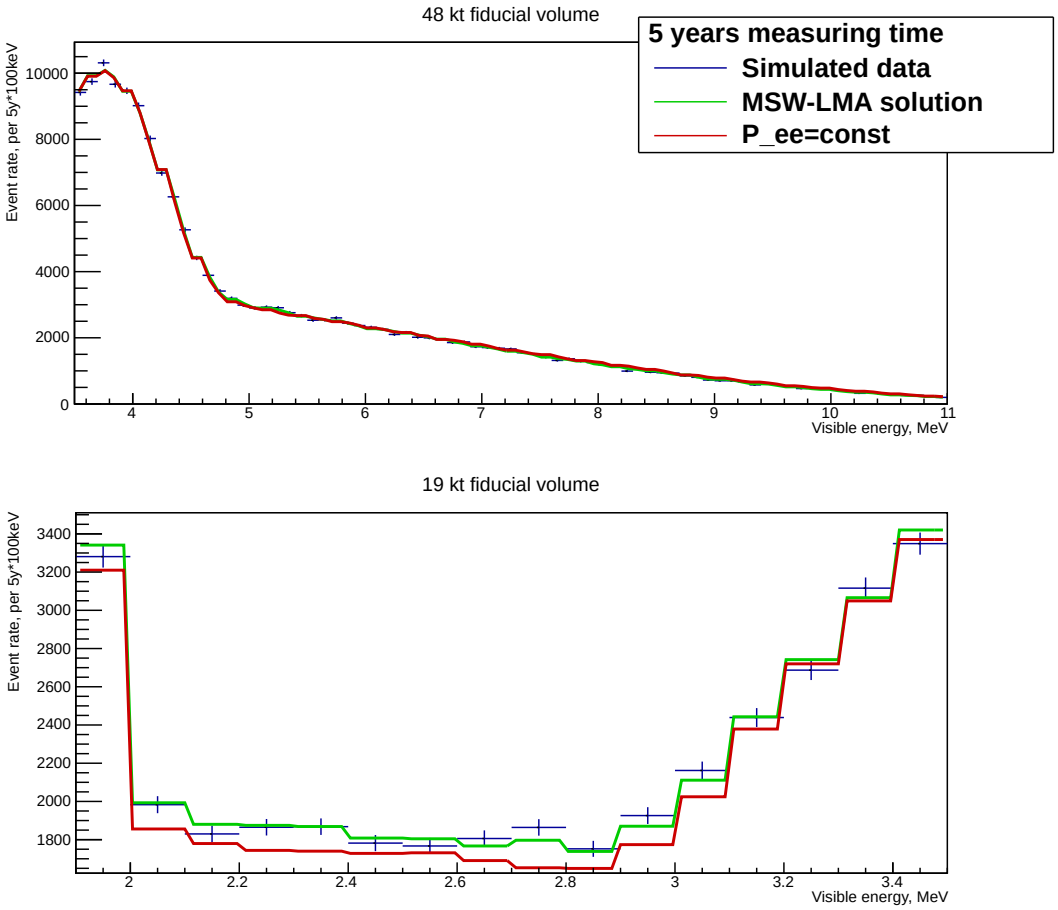

Figure 4.16: The total spectrum for the ES channel after 5 y measuring time. Furthermore, a fit according to the MSW-LMA prediction (depicted in green) and according to P_{ee} = const (depicted in red) is shown.

4.3.3 Combined Analysis

After the simulated data from the ^{13}C channel and the ES channel were analyzed, the χ^2 values of the corresponding fits were added for both P_{ee} models. From this χ^2 value and from the corresponding number of degrees of freedom, the probability that the MSW-LMA prediction and the $P_{ee} = \text{const}$ model is consistent with the data was calculated[13]. To exclude the effects of statistical fluctuations of the simulated data, this process was repeated for each of the 10^5 measurements. Finally, the probability that the $P_{ee} = \text{const}$ hypothesis can be excluded with $3\,\sigma$ and $5\,\sigma$ significance was calculated, assuming that the MSW-LMA prediction is correct.

4.4 Results

4.4.1 ^{8}B Rate

Figure 4.17 shows the distribution of the reconstructed ^{8}B rate, using the spectral fit of ES channel data after 5 years measuring time. The deviation from the expected rate is 0.06 %, which shows that the fit method works and produces correct results. The statistical error of the ^{8}B rate measurement is $\sim 0.2\,\%$ which is about a factor of 5 better than the current Super-Kamiokande results [41].
Thus, the precision of the ^{8}B flux measurement is not limited by the statistics, but will depend on the systematic errors, which are unknown at the moment (see [29] for a list of possible systematic errors). A high precision measurement of the ^{8}B flux would allow to distinguish between the low and high metallicity model (see Section 1.3) if the theoretical uncertainties of the solar neutrino fluxes are reduced in the next decade.
Even if the theorectical uncertainty of the ^{8}B flux is too large to distinguish between the two metallicity models, the measured ^{8}B flux could still have an impact on the significance of a combined analysis with the CNO flux, which is more sensitive to the metallicity, but which is also more challenging to measure. Thus, it is important to have an extensive calibration campaign at the beginning of the data taking, to reduce the systematic errors as much as possible.

4.4.2 Detection of the ^{8}B Upturn

Figure 4.18 shows the probability distribution of the χ^2 test with the MSW-LMA prediction for 5 y measuring time. As the data was generated according to the MSW-LMA prediction one would expect a flat probability distribution with 0.5

[13] Contrary to the Bayesian approach, the χ^2 test does not calculate the probability that the tested model is correct.

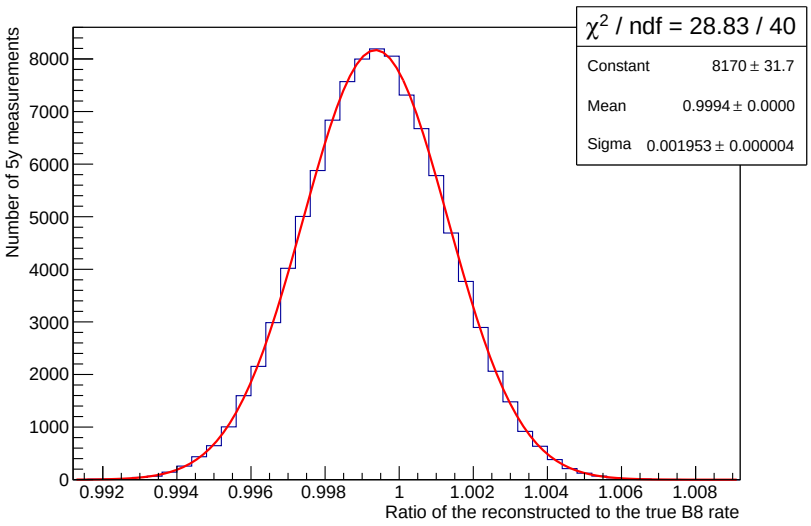

Figure 4.17: The ratio of the reconstructed to true ^{8}B rate for 10^5 independent 5 year long measurements. Additionally, a fit with a gaussian is shown in red.

mean probability. The fact that the distribution rises slightly to higher probabilities shows that the calculated χ^2 value has some deviation from a χ^2 distribution. A possible explanation is that the χ^2 distribution assumes that the entries in each bin have a gaussian error, which is only a good approximation if the number of entries per bin is large. The lowest number of entries per bin is about 200 for the fit of the ES channel and 50 for the fit of ^{13}C channel, which could explain the small deviation. Nevertheless, because the deviation from the χ^2 distribution is small, the effect on calculated signifance of the exclusion of the P_{ee} hypothesis should be negligible[14].

While the systematic errors are important for the ^{8}B flux measurement, they have a negligible effect on the exclusion significance of the $P_{ee} = \text{const}$ hypothesis, as the fits are only sensitive to the shape of the ^{8}B spectrum and not to the detected rate. Hence, systematic errors can be neglected unless they are energy dependent, which emphasises the importance of a precise energy calibration up to 10 MeV (see [29] for description of possible calibration sources).

Table 4.7 shows the results of the χ^2 test for the $P_{ee} = \text{const}$ hypothesis. After two years measuring time, the $P_{ee} = \text{const}$ hypothesis can be excluded with $5\,\sigma$ significance for 43.4 % of all simulated measurements. Assuming that the MSW-

[14]Note that the mean probability for the true model is shifted to a higher value. Thus, the calculated signifance of the exclusion of the $P_{ee} = \text{const}$ hypothesis should be lower than the true one. Hence, the assumption that the calculated χ^2 value follows an ideal χ^2 distribution is conservative.

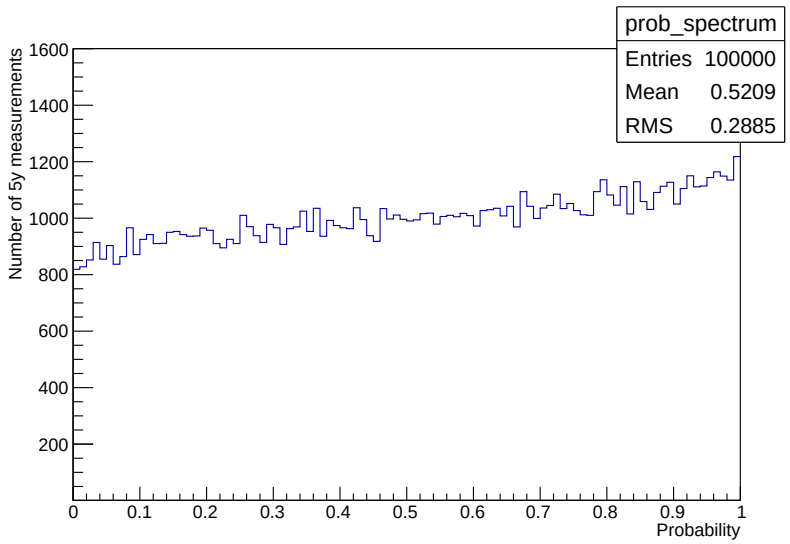

Figure 4.18: The probability distribution of the χ^2 test with the MSW-LMA model for 5 y measuring time and 10^5 independent measurements.

measuring time	prob. for a $3\,\sigma$ excl.	prob. for a $5\,\sigma$ excl.
1 years	40.5 %	2.5 %
2 years	94.9 %	43.4 %
3 years	99.9 %	92.5 %
4 years	100 %	99.8 %
5 years	100 %	100 %

Table 4.7: The significance of the exclusion of the $P_{ee} = \text{const}$ hypothesis, for measuring times ranging from 1 y to 5 y.

measuring time	prob. for a $3\,\sigma$ excl.	prob. for a $5\,\sigma$ excl.
1 years	23.6 %	0.8 %
2 years	90.4 %	34.6 %
3 years	99.8 %	86.7 %
4 years	100 %	99.4 %
5 years	100 %	100.0 %

Table 4.8: The significance of the exclusion of the $P_{ee} = \text{const}$ hypothesis, for measuring times ranging from 1 y to 5 y and for a two orders of magnitude larger intrinsic radioactive background than in Borexino.

LMA prediction is correct, the upturn of the ^{8}B spectrum at low energies can be detected with $5\,\sigma$ significance after 5 years measuring time for each simulated measurement. If the upturn is not detected after 5 years this would rule out the MSW-LMA prediction and show that new physics influence the electron neutrino survival probability in the transition region between vaccum and matter dominated oscillations.
While the cosmogenic background only depends on the detector location and can be precisely estimated, it is much harder to estimate the amount of intrinsic radioactive background, untill the detector is filled[15]. Thus, the analysis was repeated with a two orders of magnitude larger intrinsic radioactive background than Borexino, which is a very pessimistic scenario.
Table 4.8 shows the resulting significance for the detection of the ^{8}B upturn. While the significance is decreased, the effect is not very strong and after 5 years measuring time the $P_{ee} = \text{const}$ hypothesis can still be excluded, assuming that the MSW-LMA prediction is correct.
The reason for this small effect is that only the part of the ES channel spectrum between ~ 3 MeV and ~ 5 MeV visible energy is affected by the larger background. But the important region below 3 MeV has still the same background and thus the effect on the exclusion significance is tolerable. Hence, even for a much higher instrinsic radioactive background, a precise test of the MSW-LMA prediction is possible with LENA, and new physics could be detected if the upturn of the ^{8}B spectrum is not found.

[15] While there is also some uncertainty concerning the external gamma background, this background can be suppressed by using a smaller fiducial volume. Thus, if the external gamma background was two orders of magnitude larger than expected, the measuring time just needs to be increased from 5 y to 6 y.

Chapter 5

Pulse Shape Discrimination

The photon emission process in a liquid scintillator can be described by the exponential decays of a fast and several slow components (see Section 3.1). Heavier particles have a larger energy deposition per unit path length $\frac{dE}{dx}$, and thus emit a larger fraction of photons by the slow components (see Table 3.2) [48]. Hence, it is possible to distinguish between different particle types by analyzing their observed pulse shape.
In Section 5.1, two different pulse shape discrimination (PSD) methods are presented. Afterwards, the potential to discriminate ^{210}Po α background events from electron (β) events, like neutrino recoils (see Section 4.1.1), was studied (see Section 5.2). Therefore, the position dependence of the pulse shape was analyzed (see Section 5.2.1), which is mainly caused by the scattering of the emitted photons. Finally, the position dependent α-β discrimination efficiency was determined (see Section 5.2.2).

5.1 Methods

Over the past decades, several methods have been developed to distinguish between different particles in a LSD by analyzing the pulse shape. For the study of pulse shape discrimination in LENA, two different methods have been used. The simple tail-to-total method (see Section 5.1.1) and the more advanced gatti method (see Section 5.1.2).

5.1.1 Tail-to-total Method

Figure 5.1 shows a comparison between the average normalized pulse shape of α and β events in the center of LENA, after the time of flight (TOF) correction was applied (see Section 3.2). As expected, the pulse decreases much slower for alpha

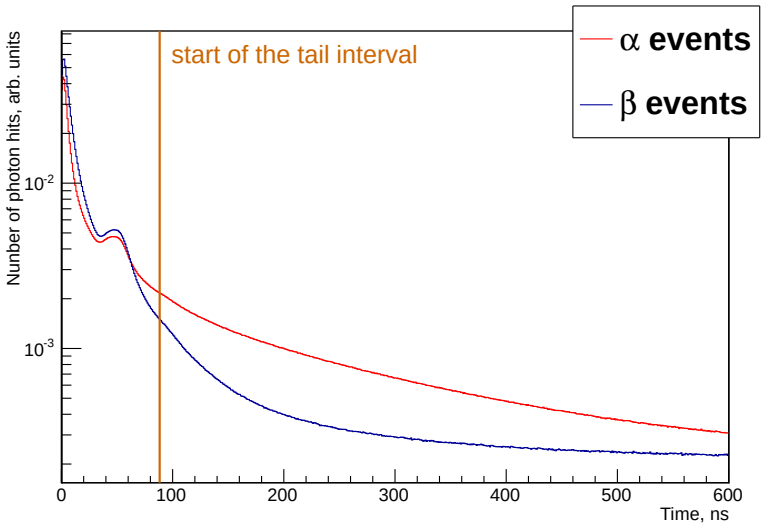

Figure 5.1: Comparison between the average normalized pulse shape of α (denoted in red) and β (denoted in blue) events in the center of LENA with $E_{vis} = 365\,keV$. The small peak around 50 ns is caused by late pulses and after pulses.

particles than for electrons. This difference is used in the tail-to-total method to discriminate α from β events.

In this method, the photon signal is integrated over two different intervals. One interval includes the complete pulse, the so called total interval, and the other one encompasses the last part of the signal, the tail interval. Subsequently, the ratio between the tail and the total interval is calculated.

From Figure 5.1 it is obvious that on average α events have a larger tail-to-total ratio than β events. Thus, the tail-to-total method can be used to distinguish between alpha and beta events.

The optimal size of the tail interval depends mainly on the PDF of the photon emission process. For α and β events, the strongest separation was achieved if the start of the tail interval was set to 90 ns. The reason for this is that after 90 ns the majority of the detected photons are emitted by the third PDF component. Hence, the fraction of photon hits in the tail interval is directly connected to the strength of the third PDF component N_3, which is very different for alpha and beta events (see Table 3.2).

Overall, the tail-to-total method can be used to distinguish between any different particle types, as long as the fraction of photons which are emitted by the third PDF component is different for each particle.

The advantage of the tail-to-total method is that it is very easy to implement and that the average pulse shapes do not need to be known. But the disadvantage is that only the integral information is used. Thus, the tail-to-total method is often not as powerful as other, more complex methods.

5.1.2 Gatti Method

A more sophisticated method to discriminate between two different particle types is the gatti method [96]. First of all, the average pulse shapes for the two particles is calculated from events where the particle type is known. Subsequently, a set of weights P_i is calculated from the two pulse shapes:

$$P_i = \frac{\alpha_i - \beta_i}{\alpha_i + \beta_i} , \tag{5.1}$$

where α_i/β_i are the normalized number of photons detected in bin i of the α/β signal. Due to the assumed $\sigma = 1\,\text{ns}$ resolution of the PMTs, the bin size was chosen to be 1 ns in the following. In the last step the so called gatti parameter G_S for a normalized signal from an unknown particle is calculated:

$$G_S = \sum_i P_i S_i . \tag{5.2}$$

Due to the weigths P_i, that are determined by the average pulse shapes of the two particles, the value of the gatti parameter depends on the particle type.
Figure 5.2 shows the gatti parameter distribution for α and β events in the center of LENA. The kinetic energy was 365 keV for the β events and 5.3 MeV for the alpha events, but due to the quenching of the heavy alpha particles (see Section 3.1.2), they both have a visible energy of 365 keV.
The difference between the two distributions is clearly visible, which shows that the gatti parameter can be used to distinguish between two particle types. Note, that the separation of α and β events is not perfect and that there is a small overlap around $G_S = 0$, which is due to statistical fluctuations. Thus, the cut efficiency for α events will depend on the chosen acceptance for the β events.
Compared to the tail-to-total method, the gatti method is generally more powerful, as the complete pulse is compared over many bins and not just the integral over two different intervals. The disadvantage is that this method is more complex and that the average pulse shapes of the particles needs to be known to calculate the gatti parameter G_S, while the tail-to-total ratio can be determined without any prior knowlegde about the average pulse shapes[1]. For the discrimination of α from

[1]Note that the cut values for the tail-to-total method can be determined by fitting the sum of two gaussians to the measured tail-to-total ratio distribution if the differences between the two pulse shapes are large enough.

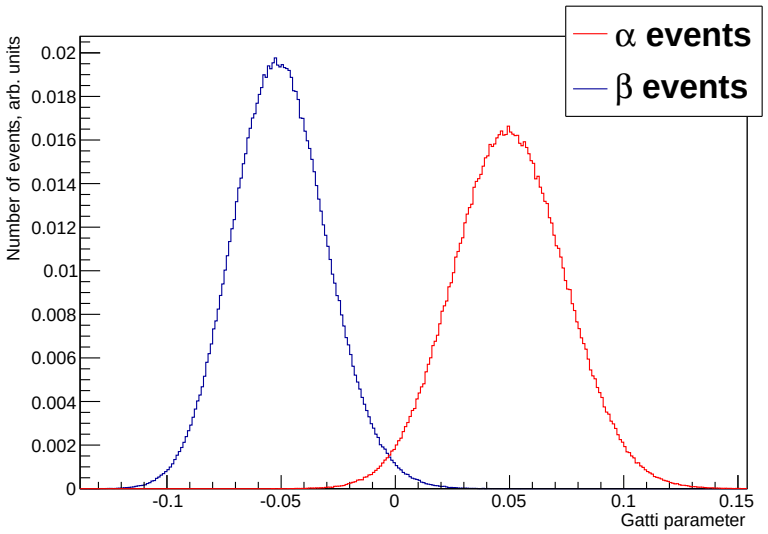

Figure 5.2: The distribution of the gatti parameter for α (denoted in red) and β events (denoted in blue) in the center of LENA with $E_{vis} = 365\,keV$.

β events, the averaged pulse shapes can be measured by using calibration sources. Another option is to use the coincidence of the ^{214}Bi β-decay and the ^{214}Po α-decay to indentify α and β events for the calculation of the average pulse shape.

But for other cases, like the distinction between inverse beta decay events and neutral current reactions of atmospheric neutrinos (see Section 6.4), one has to rely on Monte Carlo simulations to determine the average pulse shapes.

5.2 Alpha Beta Discrimination

The discrimination of α from β events is important for the solar neutrino detection in LENA. The dominant α background is ^{210}Po, which emits 5.3 MeV α particles. Due to the quenching of the scintillation light for heavy particles, the signal of a 5.3 MeV alpha corresponds to the signal of an electron with about 0.36 MeV kinetic energy and is therefore a background for the detection of ^{7}Be neutrinos.

But the identification of ^{210}Po α events is not only important for the measurement of ^{7}Be neutrinos. Futhermore, it can be used to measure the ^{210}Bi rate, which is a crucial background for the detection of CNO and pep neutrinos [17], once ^{210}Bi and ^{210}Po are in equilibrium.

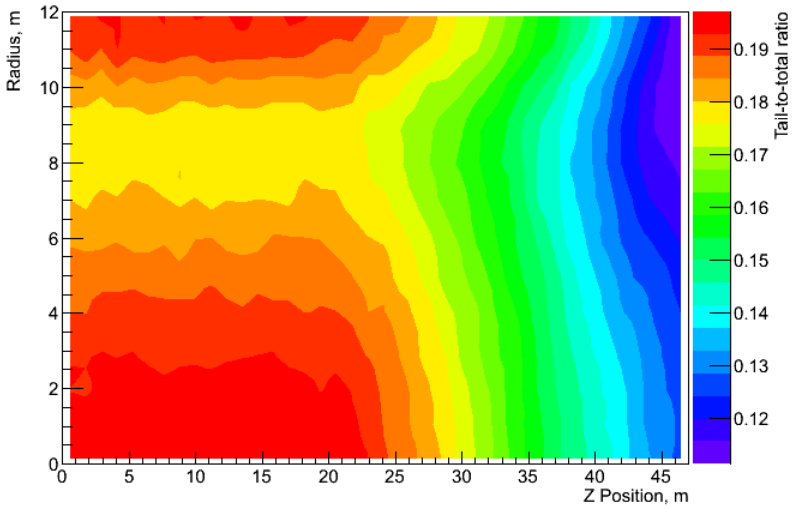

Figure 5.3: The position dependence of the average tail-to-total ratio for electrons with 300 keV kinetic energy.

5.2.1 Position Dependence of the Pulse Shape

Figure 5.3 shows the position dependence of the average tail-to-total ratio for electrons with 300 keV kinetic energy. The mean tail-to-total ratio varies from ~ 0.19 at the center (r=0 m, z=0 m) to ~ 0.11 at the egde (r=12 m, z=47 m). As the tail-to-total ratio depends on the detected pulse shape, this shows that the pulse shape is not uniform over the detector volume.
There are several reasons for this effect. First of all, the fraction of scattered photons depends on the event position. For example, at the center of the detector about 37 % of all detected photons were scattered, while at the egde only ~ 16 % of all detected photons were scattered. Scattered photons are detected later than unscattered photons, as the real time of flight of a scattered photon is bigger than the assumed one[2]. Thus, the TOF corrected emission time of a scattered photon is delayed, and therefore the tail-to-total ratio rises with the amount of scattered photons.
Additionally, the dark count rate is position dependent, due to the dark count supression cut (see Section 3.3). As the dark counts are equally distributed over the 600 ns long detection gate, an increase in the dark count rate also leads to an

[2]In case of the absorption and subsequent reemission of a photon on a PPO molecule, the detection time is further delayed, because the reemission process is not instantaneous (see Section 3.1.2). But as $\tau_{\mathrm{re}} = 1.2\,ns$ is on average much smaller than the delay due to the longer path length, this effect has only a minor contribution.

increase of the average tail-to-total ratio.
Furthermore, the photoelectron yield also has an effect on the tail-to-total ratio. If the photoelectron yield is large, the relative contribution of the dark counts is reduced and thus the average tail-to-total ratio is smaller.
As the pulse shape depends on the event position, an additional calibration of the simulated detector was necessary for the PSD. In the calibration runs, electrons with kinetic energies of 300 keV and 500 keV, as well as alpha particles with the same visible energy, were simulated. The calibration points were homogeneously distributed in x and in z direction (y=0 for all events), with 1 m distance between the calibration points, as it was done for the energy calibration (see Section 3.2). At each calibration point, the tail-to-ratio was calculated as the ratio of the detected photons in the time intervals [90 ns, 600 ns] and [0 ns, 600 ns] for each event. The gatti weights were calculated according to equation (5.1) from the averaged α and β pulse shapes at each calibration point, using 1 ns wide bins ranging from 0 ns to 600 ns.
Using the gatti weights, the gatti parameter was calculated according to equation (5.2) for each event. Afterwards, the tail-to-total ratio and the gatti parameter distribution were fitted with a gaussian at each calibration point and the corresponding average values and standard deviations were saved. For an arbitrary event position, the average tail-to-total ratio, gatti parameter and the corresponding standard deviations can be calculated by using a linear approximation of the expected values at the adjacent calibration points, analogous to the calculation of the average photo electron yield (see Section 3.2).

5.2.2 Discrimination Efficiency

In order to determine the $\alpha - \beta$ discrimination efficiency, which is defined as the fraction of vetoed α events for a certain acceptance of β-events, $5 \cdot 10^5$ 5.3 MeV alpha events were simulated, corresponding to the alpha energy of the ^{210}Po decay. The events were distributed homogeneously over a fiducial volume with 12 m radius ($|z| < 47$ m), which is the expected fiducial volume for the ^{7}Be measurement.
For each event, the tail-to-total ratio and the gatti parameter were calculated. In the next step, the cut values were calculated by using a linear approximation of the expected standard deviations and mean values of the tail-to-total ratio and gatti parameter distributions at the adjacent calibration points. Finally, the tail-to-total ratio and the gatti parameter were compared with the corresponding cut values for these two parameters. For each parameter, several cut values were used to get different β-acceptances. The β-acceptance was determined for each cut value by simulating electron events with 365 keV kinetic energy, which were homogeneously distributed over the fiducial volume. Hence, the β-acceptance is correct even if tail-to-total ratio and gatti parameter distribution have non-gaussian tails.

β-acceptance	discrimination efficiency tail-to-total method	discrimination efficiency gatti method
95.0 %	99.3 ± 0.1 %	99.7 ± 0.1 %
99.0 %	96.7 ± 0.1 %	98.0 ± 0.1 %
99.9 %	87.5 ± 0.1 %	90.0 ± 0.1 %

Table 5.1: The α-β discrimination efficiency at 5.3 MeV α energy (^{210}Po peak), which corresponds to $E_{vis} = 365$ keV, of the tail-to-total and the gatti method for various β acceptances.

Table 5.1 shows the resulting α-β discrimination efficiency of the tail-to-total and the gatti method. Both methods allow an efficient reduction of the alpha background, though the performance of the gatti method is as expected slightly better. Thus, only the results of the gatti method are discussed in the following.

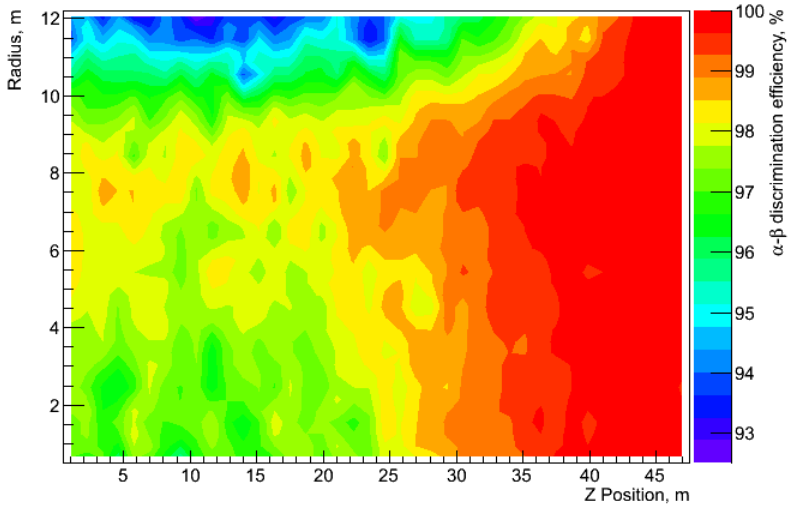

Figure 5.4: The simulated position dependence of the α-β discrimination efficiency at 5.3 MeV, using the gatti method with 99.0 % β-acceptance.

Figure 5.4 shows the position dependence of the α-β discrimination efficiency at 5.3 MeV, using the gatti method with 99.0 % β-acceptance. The discrimination efficiency ranges from $\sim$ 93 % (r=12 m, z=0 m) to almost 100 % at the egde of the fiducial volume (r=12 m, z=47 m).
There are several reasons for this position dependence. First of all, the photo electron yield is not uniform over the fiducial volume (see Figure 3.2). At positions

where the photo electron yield is low, the statistical fluctuations of the detected pulse shapes are larger. Thus, the discrimination efficiency is reduced.
Another reason is that the ratio of scattered photons depends on the event position. If a photon is scattered, it will be detected at a later time compared to an unscattered photon and the time delay will depend on exact path of the photon. Hence, the statistical fluctuation of the photon detection time is increased due to the scattering. As this statistical fluctuation does not have a symmetric distribution, it also changes the average pulse shapes such that the α and the β pulse shape become more similar. Hence, the differences between the mean values of the gatti parameter distributions of both particles gets smaller and the widths of both distributions become larger. Thus, the discrimination efficiency deteriorates with an increasing ratio of scattered photons.
Furthermore, the dark count rate also depends on the event position, due to the dark count suppression cut (see Section 3.2). A larger dark count rate decreases the discrimination efficiency, as the homogeneously distributed dark counts reduce the differences between the α and the β pulse shape.
In order to quantify this effect, the simulations were repeated with higher dark count rates. If the dark count rate is increased to 2 kHz per PMT, the discrimination efficiency is reduced to less than 90 % at 99.0 % β acceptance. A further increase to 4 kHz per PMT reduces the discrimination efficiency to less than 80 % at 99.0 % β acceptance. Thus, the dark noise rate should not be higher than 0.7 kHz per 8-inch PMT[3], to allow an effective reduction of the ^{210}Po α background[4].
Contrary to the dark noise rate, the late and the after pulse rates have almost no effect on the discrimination efficiency. Even if both are increased to an unrealistic high rate of 20%, the discrimination efficiency stays above 97 % at 99.0 % β acceptance. The reason for this is that the late and after pulses are correlated to the detected photons. Hence, while an increased late and after pulse rate changes the pulse shape, the difference between the α and the β events remains almost unaltered.
Besides discriminating α background events for the ^{7}Be detection, the PSD can also be used to make a low background measurement of ^{210}Po α events. A precise measurement of the ^{210}Po rate can be used to make an indirect measurement of the ^{210}Bi rate, because ^{210}Po is produced by the β^- decay of ^{210}Bi. This indirect measurement of ^{210}Bi is important for the detection of CNO and pep neutrinos, as ^{210}Bi has a similar energy spectrum as the CNO neutrinos and is thus a crucial background.
The requirement for the indirect measurement is that the ^{210}Po and ^{210}Bi decays

[3]In Borexino, the average dark noise rate per 8-inch PMT is less than 100 Hz [97].

[4]Note that for other applications of the PSD, where the visible energy is higher, the dark count rate does not have such a strong effect.

are in equilibrium. At the beginning of the data taking this will probably not be the case, as small amounts of ^{210}Po will be inserted into the scintillator during the filling and the calibration campaign. But as ^{210}Po decays with a half-life of 138 d, an equilibrium between ^{210}Po and ^{210}Bi should be reached after a few years.
In order to precisely measure the ^{210}Po rate, an efficient discrimination of the β events from the alpha events is necessary. But due to the large statistics, it is not important to have a large α acceptance. If the same radiopurity level as in Borexino is reached and if ^{210}Po and ^{210}Bi are in equilibrium, more than $5 \cdot 10^5$ ^{210}Po events are detected per year. Hence, an α acceptance of 50 % is sufficient to reduce the statistical error well below 1 %. Using such a strong cut, the β events can be discriminated with more than 99.99 % efficiency at every position in the fiducial volume. Hence, the residual β events which pass this cut will introduce a negligible error on the ^{210}Po rate.
Thus, if the systematic error, which is caused by the uncertainty of the α cut efficiency, is kept below 1 %, a statistical reduction of the ^{210}Bi background by two orders of magnitude is possible. The uncertainty of the α cut efficiency can be reduced by inserting an encapsulated ^{210}Po calibration sources into the detector. Assuming that the same radiopurity level as in Borexino is reached, this would open the window for the first measurement of the CNO flux.

Chapter 6

The Diffuse Supernova Neutrino Background

The cumulative neutrino emission of core-collapse supernovae throughout the universe has created the so-called Diffuse Supernova Neutrino Background (DSNB), which contains information about the average supernova neutrino spectrum and about the redshift dependent supernova rate R_{SN} (see Section 1.4).
Due to the low flux, a measurement of the DSNB requires a large target mass and a good background suppression. In Super-Kamiokande, about 2-4 inverse beta decay (IBD) events per year are expected, but as the 2.2 MeV gamma of the neutron capture on hydrogen is below the detection threshold, the delayed coincidence of the prompt positron signal and the delayed neutron capture could not be used to reduce the background. Hence, only an upper limit on the $\bar{\nu}_e$ flux of $3.1\,\bar{\nu}_e\,cm^{-2}s^{-1}$ (90 % C.L.) for $E_{\bar{\nu}_e} > 17.3$ MeV was obtained [39].
Contrary to Super-Kamiokande, LENA can detect the 2.2 MeV gamma of the neutron capture on hydrogen and has therefore a much better background suppression. Furthermore, the target mass of LENA is about twice as large as Super-Kamiokande. Hence, the potential of LENA to detect the DSNB was studied with a Monte Carlo simulation.
In a first step, the DSNB spectra were simulated for several different predicted supernova neutrino spectra (see Section 6.1). Afterwards, the indistinguishable $\bar{\nu}_e$ background from reactor and atmospheric neutrinos was studied (see Section 6.2). Subsequently, the backgrounds from cosmogenic radioisotopes and fast neutrons were analyzed (see Section 6.3). In Section 6.4, the background which is caused by neutral current (NC) reactions of atmospheric neutrinos was simulated. In the next step, the possibility to suppress the atmospheric NC and fast neutron background by pulse shape discrimination (PSD) was analyzed (see Section 6.5). Finally, the detection potential was calculated, using the simulated signal and background rates (see Section 6.6).

6.1 Simulation of the Diffuse Supernova Neutrino Background Spectrum

The DSNB contains neutrinos of all flavours and the corresponding antineutrinos. Due to the low flux, the only possible detection channel is the IBD reaction of $\bar{\nu}_e$ on free protons:

$$\bar{\nu}_\mathrm{e} + \mathrm{p} \rightarrow \mathrm{e}^+ + \mathrm{n} \ , \tag{6.1}$$

as it has the largest cross section at low energies. Furthermore, the delayed coincidence of the prompt positron signal and delayed neutron signal (see Section 2.2.3) can be used to suppress the background.
Due to the kinematics of the IBD reaction, the kinetic energy of the neutron is insignificant [98]. Hence, the kinetic energy of the positron $\mathrm{E_{kin}}(\mathrm{e}^+)$ can be approximated by:

$$\mathrm{E_{kin}}(\mathrm{e}^+) = \mathrm{E}_\nu - \mathrm{Q_{IBD}} \ , \tag{6.2}$$

where $\mathrm{Q_{IBD}} = 1.80\,\mathrm{MeV}$ is the Q-Value of the IBD reaction. After the positron has deposited its kinetic energy[1], it annihilates with an electron and produces two 511 keV gammas. Due to the quenching, these gammas deposite only $\approx 0.93\,\mathrm{MeV}$ visible energy. Hence, the neutrino energy can be reconstructed from the visible energy of the prompt positron signal by the following formula:

$$\mathrm{E}_\nu \approx \mathrm{E_{vis}} + 0.87\,\mathrm{MeV}. \tag{6.3}$$

Assuming that the supernova neutrino spectrum and the luminosity is independent of the neutrino flavour such that:

$$\langle \mathrm{E}_{\bar{\nu}_\mathrm{e}} \rangle = \langle \mathrm{E}_{\bar{\nu}_\mu} \rangle = \langle \mathrm{E}_{\bar{\nu}_\tau} \rangle \tag{6.4}$$

and

$$\mathrm{L}_{\bar{\nu}_\mathrm{e}} = \mathrm{L}_{\bar{\nu}_\mu} = \mathrm{L}_{\bar{\nu}_\tau} \ , \tag{6.5}$$

neutrino oscillations can be neglected. Hence, the DSNB spectrum for the IBD reaction is given by:

$$\frac{\mathrm{dR}_\nu}{\mathrm{dE}_\nu} = \frac{\mathrm{dF}_\nu}{\mathrm{dE}_\nu} \cdot \sigma_\nu(\mathrm{E}_\nu) \cdot \mathrm{N_p} \ , \tag{6.6}$$

where $\frac{\mathrm{dF}_\nu}{\mathrm{dE}_\nu}$ is the DSNB flux (see Section 1.4), $\sigma_\nu(\mathrm{E}_\nu)$ is the energy dependent cross section of the IBD reaction and $\mathrm{N_p} = 3.67 \cdot 10^{33}$ is the number of protons in the target volume ($\mathrm{r} < 13.5\,\mathrm{m}$, $|\mathrm{z}| < 48.5\,\mathrm{m}$) [48].

[1] There is also a small probability, that the positron annihilates with an electron before it is stopped.

The energy dependent cross section of the IBD reaction can be approximated by [98]:

$$\sigma_\nu(\mathrm{E}_\nu) \approx \mathrm{p_e E_e} \left(\frac{\mathrm{E}_\nu}{\mathrm{MeV}}\right)^{-0.07056+0.014321\ln(\mathrm{E}_\nu/\mathrm{MeV})} \cdot 10^{-43} \frac{\mathrm{cm}^2}{\mathrm{MeV}^2} \ , \qquad (6.7)$$

where $\mathrm{p_e}$ is the positron momentum and $\mathrm{E_e} = \mathrm{E}_\nu - 1.293\,\mathrm{MeV}$ is the total energy of the positron.
Using equation (6.6) and (6.2), four different DSNB spectra with $\langle \mathrm{E}_\nu \rangle$ ranging from 12 MeV to 21 MeV were simulated, according to the predicted range of $\langle \mathrm{E}_\nu \rangle$ (see Section 1.4). The events were homogeneously distributed over a fiducial volume with 13.5 m radius and only the prompt positron signal was simulated. To reconstruct the visible energy, a new set of calibration runs was performed (see Section 3.2), using positrons with energies ranging from 8.2 MeV to 28.2 MeV. As there are no pure β calibration sources with $\mathrm{Q} > 5\,\mathrm{MeV}$, the energy reconstruction of DSNB events in the real detector has to rely on Monte Carlo simulations, which are validated by calibration sources at lower energies. After reconstructing the visible energy, the neutrino energy was calculated by using equation (6.3).

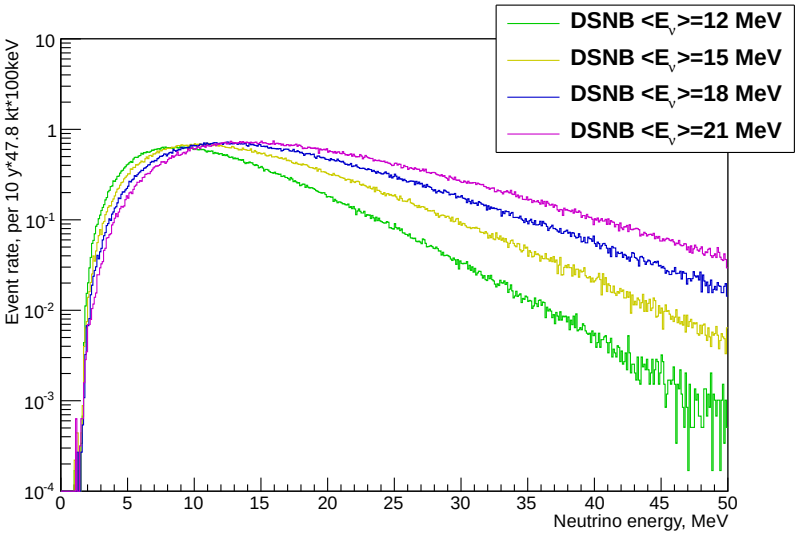

Figure 6.1: The DSNB spectra in LENA for different supernova neutrino spectra with mean energies ranging from 12 MeV to 21 MeV.

Figure 6.1 shows the resulting DSNB spectra. Depending on $\langle \mathrm{E}_\nu \rangle$, the DSNB spectra peak around 8 MeV to $\sim$ 16 MeV and then decrease exponentially. The position of the peak is at lower neutrino energies than what one would expect from a Maxwell-Boltzmann distribution. The reason for this is that the neutrinos are redshifted and thus the effective mean energy is lowered.

After 10 years of measuring time, about 85 to 156 DSNB events are expected below 50 MeV. Therefore, it is clear that backgrounds are a crucial issue for the detection of the DSNB.

6.2 $\bar{\nu}_e$ Charged Current Background

The most dangerous background for the DSNB detection are other $\bar{\nu}_e$ sources in the same energy range as the DSNB, as these events are indistinguishable from the DNSB signal. Hence, these events can only be suppressed by an energy cut which limits the detection window for the DSNB. Possible $\bar{\nu}_e$ sources are reactor neutrinos, atmospheric neutrinos and geoneutrinos. In the following, only the reactor $\bar{\nu}_e$ and atmospheric $\bar{\nu}_e$ background will be discussed, as the geoneutrino flux is limited to $E_{\bar{\nu}_e} < 3.2\,\mathrm{MeV}$, where the reactor $\bar{\nu}_e$ flux surpasses the DSNB signal by several orders of magnitude.

6.2.1 Reactor Neutrinos

The differential reactor neutrino rate $\frac{dR_R}{dE}$ is given by

$$\frac{dR_R}{dE} = \frac{d\Phi_R}{dE} \cdot \sigma_\nu(E_\nu) \cdot N_p \ , \tag{6.8}$$

where $\frac{d\Phi_R}{dE}$ is the differential reactor neutrino flux for the Pyhäsalmi site, which was calculated in [44][2]. Using equation (6.8), $1 \cdot 10^6$ reactor neutrino events, which were homogeneously distributed over the fiducial volume ($r < 13.5\,\mathrm{m}$, $|z| < 48.5\,\mathrm{m}$), were simulated.
Figure 6.2 shows the resulting reactor neutrino spectrum. The spectrum peaks at about 4 MeV, where it surpasses the DSNB signal by several orders of magnitude. Hence, a detection of the DSNB signal is not possible in this energy region. Thus, the reactor neutrino background sets a lower limit on the DSNB detection window. Above $\sim 6\,\mathrm{MeV}$, the reactor neutrino spectrum decreases almost exponentially and drops below the DSNB signal at about 9.5 MeV. Thus, the lower limit of the DSNB detection window was set to 9.5 MeV in the following analysis.
Due to the low statistics of the simulated reactor neutrino background above 9.5 MeV, a second simulation with 7.5 MeV threshold for the initial reactor neutrino energy was performed. Figure 6.3 shows the resulting reactor neutrino spectrum above 8 MeV neutrino energy.

[2]Note that the shutdown of eight nuclear power plants in Germany after the disaster at the fukushima daichi nuclear power plant in 2011 are not included in these calculations. Furthermore, the building of additional nuclear power plants in Finland in the next decade could increase the reactor neutrino background.

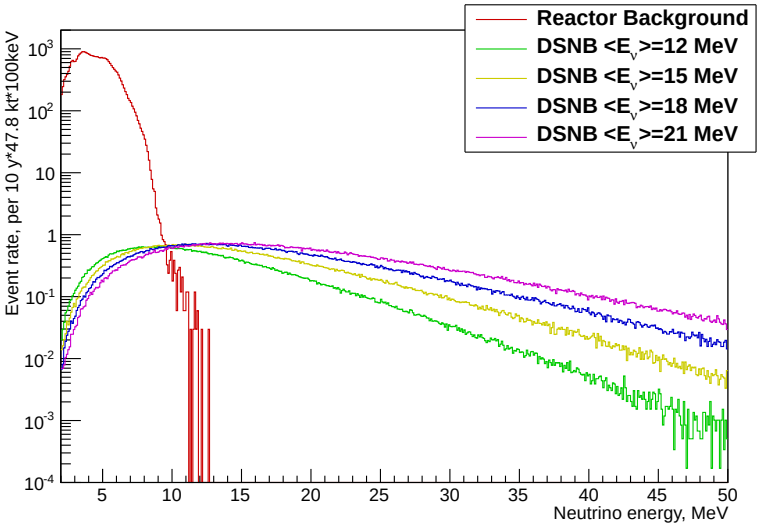

Figure 6.2: The simulated reactor neutrino spectrum. For comparison, the DSNB spectra with $\langle E_\nu \rangle$ ranging from 12 MeV to 21 MeV are also depicted.

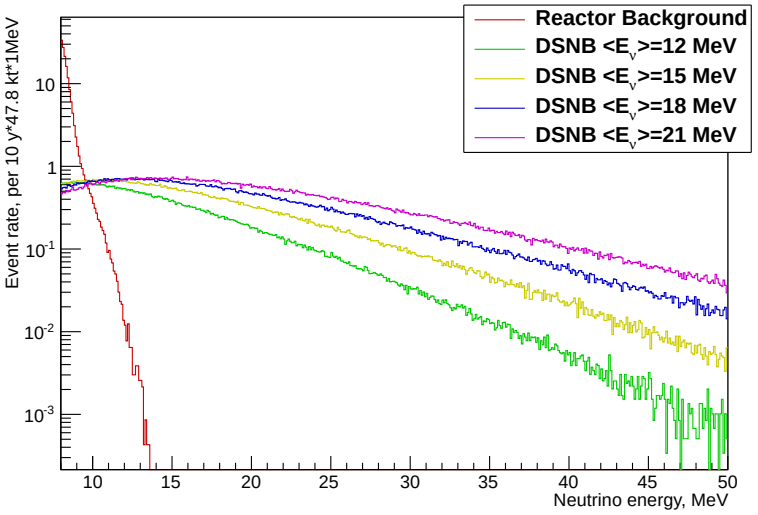

Figure 6.3: The simulated reactor neutrino spectrum above 8 MeV. For comparison, the DSNB spectra with $\langle E_\nu \rangle$ ranging from 12 MeV to 21 MeV are also depicted.

By restricting the DSNB detection window to $E_\nu > 9.5\,\mathrm{MeV}$, the reactor $\bar{\nu}_e$ background is reduced from $2.2 \cdot 10^4$ events per 10 y to 5.3 events per 10 y, which is about one order of magnitude below the DSNB signal. But this energy cut also reduces the DSNB signal. If $\langle E_\nu \rangle = 12\,\mathrm{MeV}$, the signal is reduced by almost 40 % from 85 to 53 events per 10 y. The effect of the energy cut on the signal rate decreases if the supernova mean neutrino energy increases. But even for the optimal case of $\langle E_\nu \rangle = 21\,\mathrm{MeV}$, the DSNB signal is still reduced by $\sim 15\,\%$ from 156 to 136 events.

6.2.2 Atmospheric Neutrinos

Besides reactor neutrinos, atmospheric antielectron neutrinos are another indistinguishable background. The atmospheric $\bar{\nu}_e$ spectrum can be calculated analogously to the reactor neutrino spectrum by using equation (6.8) and the atmospheric $\bar{\nu}_e$ flux for the Pyhäsalmi site, which was calculated in [44].

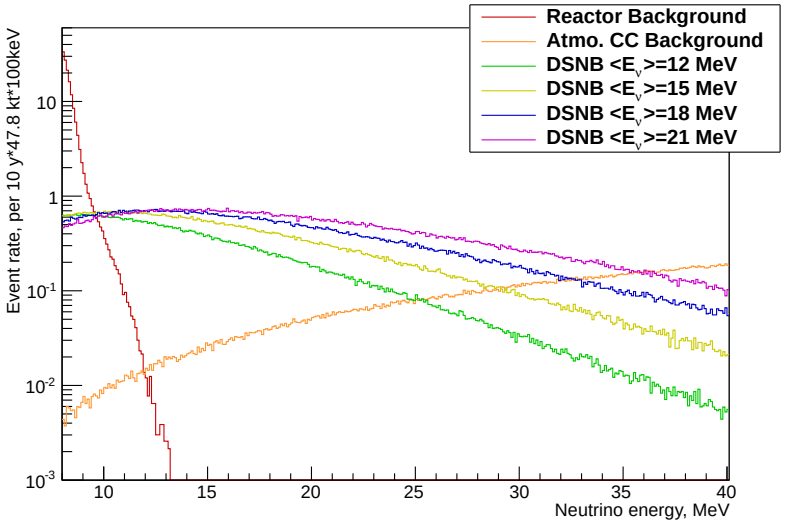

Figure 6.4: The simulated atmospheric $\bar{\nu}_e$ spectrum in LENA at Pyhäsalmi. For comparison, the DSNB spectra with $\langle E_\nu \rangle$ ranging from 12 MeV to 21 MeV and the reactor neutrino spectrum are also depicted.

Figure 6.4 shows the resulting atmospheric $\bar{\nu}_e$ spectrum for $5 \cdot 10^4$ simulated events, which were homogeneously distributed over a fiducial volume with 13.5 m radius. Contrary to the reactor neutrino spectrum, the atmospheric $\bar{\nu}_e$ is suppressed at low energies and rises with increasing energy. At 25 MeV, the atmospheric $\bar{\nu}_e$ spectrum surpasses the DSNB spectrum with $\langle E_\nu \rangle = 12\,\mathrm{MeV}$. For $\langle E_\nu \rangle > 12\,\mathrm{MeV}$,

$\langle E_\nu \rangle$	Expected DSNB events per 10 y
12 MeV	48.2
15 MeV	69.2
18 MeV	85.1
21 MeV	95.1

Table 6.1: The DSNB event rates between 9.5 MeV and 25 MeV reconstructed neutrino energy with $\langle E_\nu \rangle$ ranging from 12 MeV to 21 MeV.

the DSNB signal ist still above the atmospheric $\bar{\nu}_e$ background at $E_\nu = 25$ MeV, so that a larger detection window could be used.
But in order to avoid any experimental bias, the detection window should be chosen before the start of the data taking. Due to the low statistics and the large uncertainty about the DSNB spectrum, it is not possible to determine the background and the DSNB rate by a spectral fit. Instead, it is assummed in the following analysis that the background rate in the detection window is known, so that it can be statistically subtracted from the number of detected events. Thus, if the used detection window is too large, this would deteriorate the sensitivity to detect the DSNB. Hence, in order to maximize the detection potential for low supernova neutrino mean energies, the upper limit of the detection window was set to 25 MeV. This energy cut reduces the atmospheric $\bar{\nu}_e$ background to 6.0 events per 10 y, which is almost one order of magnitude below the DSNB signal for $\langle E_\nu \rangle = 12$ MeV.
Hence, 11.3 background events are expected in the DSNB detection window, which ranges from 9.5 MeV to 25 MeV. Table 6.1 shows the DSNB event rates in this energy window. Due to the two energy cuts, the event rate is reduced by about 40 %. Nevertheless, the expected event rate is at least four times larger than the indistinguishable background from atmospheric and reactor antielectron neutrinos. Hence, while the $\bar{\nu}_e$ background reduces the already limited event rate, it does not make the detection of the DSNB impossible.

6.3 Muon-induced Backgrounds

There are two types of muon induced backgrounds which can mimic the IBD event signature. A cosmic muon which traverses the target volume can produce radioisotopes through spallation reactions on carbon. While the majority of these radioisotopes can be vetoed by the delayed coincidence condition, ^{8}He and ^{9}Li can β^- decay into an excited state, leading to the emission of a neutron. Hence, these two isotopes can mimic the IBD event signature and are thus a background for

the DSNB detection (see Section 6.3.1).
Another muon induced background are fast neutrons, which are produced in the surrounding rock around the muon veto. These neutrons have a large range and are usually invisible for the muon veto. Inside the target volume, the prompt signal due to neutron scattering reactions and the delayed signal due to the neutron capture can mimic the DSNB event signature (see Section 6.3.2).

6.3.1 Cosmogenic Radioisotopes

^{8}He ($Q_{\beta^-} = 10.6\,\mathrm{MeV}$) and ^{9}Li ($Q_{\beta^-} = 13.6\,\mathrm{MeV}$) are β^- unstable radioisotopes, which are produced in-situ by traversing cosmic muons. When these isotopes decay into the ground state, they do not pose a background for the DSNB detection as they do not fulfill the delayed coincidence condition.
^{8}He decays with 16 % branching ratio into an excited state, leading to the subsequent emission of a neutron [91]:

$$^{8}\mathrm{He} \rightarrow \mathrm{e}^- + \bar{\nu}_\mathrm{e} + {}^{8}\mathrm{Li}^* \tag{6.9}$$

$$^{8}\mathrm{Li}^* \rightarrow \mathrm{n} + {}^{7}\mathrm{Li} \tag{6.10}$$

In this case, the electron from the β^--decay and the neutron scattering reactions cause the prompt signal and the subsequent capture of the neutron on a free proton or on carbon causes the corresponding delayed signal.
The neutron separation energy of ^{8}Li is 2.0 MeV [91]. Hence, the Q-Value is reduced to 8.6 MeV. Furthermore, the emitted neutron is strongly quenched. Thus, the maximum visible energy is 7.6 MeV which corresponds to 8.5 MeV reconstructed neutrino energy and is outside the DSNB detection window (see Section 6.2). Thus, ^{8}He is no background for the DSNB detection.
Analogous to ^{8}He, ^{9}Li decays with 50.8 % branching ratio into an excited state, which leads to the emission of a neutron and two alphas:

$$^{9}\mathrm{Li} \rightarrow \mathrm{e}^- + \bar{\nu}_\mathrm{e} + {}^{9}\mathrm{Be}^* \tag{6.11}$$

$$^{9}\mathrm{Be}^* \rightarrow \mathrm{n} + 2\,\alpha \tag{6.12}$$

The first excited state of ^{9}Be is at 2.43 MeV and thus the maximum kinetic energy of the emitted electron is 11.2 MeV. Hence, the maximum reconstructed neutrino energy is above the 9.5 MeV DSNB detection threshold.
Analogous to Section 4.2.1, the ^{9}Li β^--n spectrum was determined in two steps. In the first step, the spectral shape was simulated with the Monte Carlo simulation. As the G4Radioactive module does not describe the decay of ^{9}Li into excited states correctly, an own module was developed, which simulates the decay according to [99]. While there is a non-vanishing probability that the first excited state emits

a gamma instead of a neutron, it was assumed in the simulation that it always emits a neutron, which is a conservative assumption. For each simulated event, the visible energy was reconstructed and the neutrino equivalent energy was calculated according to equation (6.3).
Afterwards, the ^{9}Li rate $R_B(^9Li)$ that was measured by Borexino [47] was scaled to obtain the expected rate for the Pyhäsalmi location:

$$R_P(^9Li) = R_B(^9Li) \cdot \frac{\Phi_P^\mu}{\Phi_B^\mu} \ , \tag{6.13}$$

where $\Phi_P^\mu = 0.235\,m^{-2}h^{-1}$ is the expected muon flux at 4 km w.e. depth [53] and $\Phi_B^\mu = 1.22\,m^{-2}h^{-1}$ is the muon flux at the location of the Borexino detector [44]. No scaling was applied for the different mean muon energies and scintillator compositions as they have a negligible effect on the ^{9}Li rate.
Using the branching ratio $Br(^9Li_{\beta n}) = 50.8\,\%$, the ^{9}Li β^-n rate was calculated to be:

$$R_P(^9Li_{\beta n}) = R_P(^9Li) \cdot Br(^9Li_{\beta n}) = 1.5 \cdot 10^3 \frac{\text{events}}{\text{year}} \ . \tag{6.14}$$

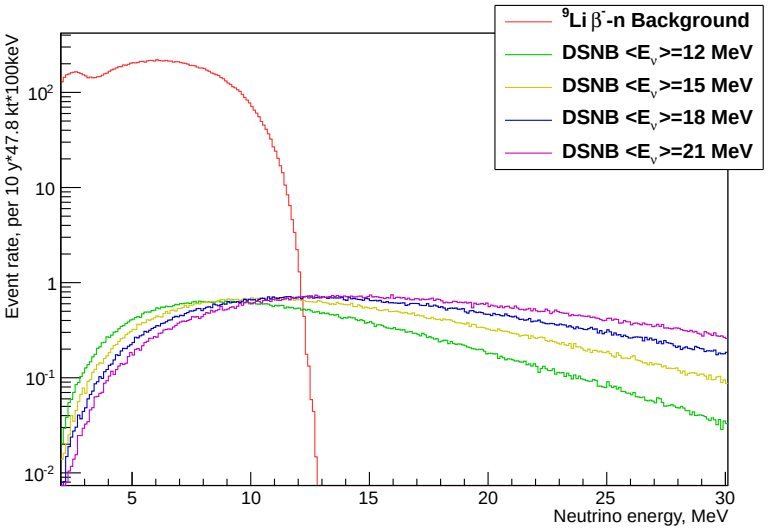

Figure 6.5: The simulated ^{9}Li β^-n background spectrum. For comparison, the DSNB spectra with $\langle E_\nu \rangle$ ranging from 12 MeV to 21 MeV are also depicted.

Figure 6.5 shows the resulting ^{9}Li β^--n background spectrum. About 10^3 ^{9}Li β^--n events above 9.5 MeV are expected per 10 y, which is more than one order of magnitude above the DSNB signal for $\langle E_\nu \rangle = 12$ MeV.

The DSNB signal surpasses the ^{9}Li β^--n spectrum at about 12 MeV. Hence, the ^{9}Li β^--n background could be reduced to less than 4 events per 10 y if the lower limit of the detection window would be increased from 9.5 MeV to 12 MeV. But this would also reduce the expected DSNB event rate by up to 30 %.
As ^{9}Li is always produced close to a muon track, the ^{9}Li β^-n background can also be suppressed by vetoing a cylinder with 2 m radius around each muon track for 2.5 s. In this case, the DSNB event rate is only reduced by 0.2 % due to the introduced dead time. The life time of ^{9}Li is 257.2 ms and the ^{9}Li β^--n background is therefore suppressed to a negligible amount of 0.01 events per 10 y. Hence, this background is not considered anymore in the following.

6.3.2 Fast Neutrons

Cosmic muons traversing the surrounding rock around the muon veto can produce fast neutrons. These neutrons have a broad energy spectrum which extends into the GeV range. Hence, it is possible that they propagate from the rock into the target volume without triggering the muon veto. Inside the target volume, the neutron causes a prompt signal due to scattering reactions on protons and carbon. Afterwards it thermalizes and captures on a free proton with a mean capture time of $\tau \approx 250\,\mu$s, emitting a 2.2 MeV gamma[3]. Thus, it has the same event signature as a $\bar{\nu}_e$ and is therefore a dangerous background for the DSNB detection.
As the simulation of cosmic muons is very time consuming, the simulation was performed in two steps. In the first step, the production of the neutrons in the surrounding rock was simulated, while the propagation of the neutrons into the detector was simulated in the second step.

Fast neutron production

The neutron production yield at a certain depth can be approximated by assuming that all muons have the corresponding mean energy. Hence, the muon energy was set to 300 GeV, corresponding to the mean muon energy at 4 km w.e. depth [53]. Only a small fraction of the neutrons ($< 10\,\%$) are produced directly by muon induced spallation reactions. The majority of the neutrons are produced in muon induced electromagnetic and hadronic cascades. Hence, the simulated muon track has to be long enough, so that these cascades have enough space to develop. But the muon track also must not be too long, so that the muon energy loss over the track can be neglected. Thus, the muons were propagated through 15 m of limestone rock ($CaC0_3$, $\rho = 2.73 \frac{\mathrm{g}}{\mathrm{cm}^3}$), so that the average energy loss along the track was less than 3 %.

[3] About 1% of the neutrons are captured on ^{12}C, resulting in the emission of a 4.9 MeV gamma, or multiple gammas with 4.9 MeV total energy.

For every produced neutron, the vertex position, the kinetic energy and the momentum direction were saved. If a neutron scatters inelastically, GEANT4 terminates the primary neutron track and creates a new neutron track. Hence, in order to avoid double counting of neutrons, the first neutron in the list of secondary particles was considered as the incident neutron and was therefore not counted.

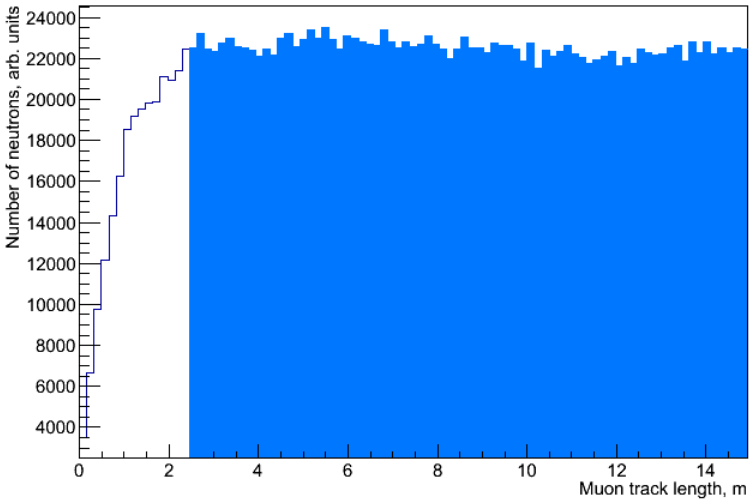

Figure 6.6: The simulated neutron production along a 15 m long muon path. Only neutrons that were produced after 3 m (blue region) were used to calculate the neutron production yield.

Figure 6.6 shows the average neutron production along the muon path for $1 \cdot 10^6$ simulated muons. After a steep rise on the first $\sim$ 3 meters of the muon track, the neutron production rate is almost constant. The reason for the rise at the beginning of the track is that electromagnetic and hadronic cascades, which are responsible for more than 90 % of the generated neutrons, need some space to develop. Hence, only neutrons that were produced after 3 m were used for the following analysis.
Using the simulation results, the neutron production yield per unit path length was calculated to be:

$$Y_n = 5.0 \cdot 10^{-4} (\mu g/cm^2)^{-1}, \tag{6.15}$$

which is about 50 % more than the yield that Borexino measured in pseudocume [47]. The reason for this difference is that the neutron production yield per unit path length also depends on the mean atomic weight [53], which is larger for limestone rock than for pseudocumene[4].

[4]Note that the mean muon energy at the LNGS is with 283 GeV slightly smaller, which also

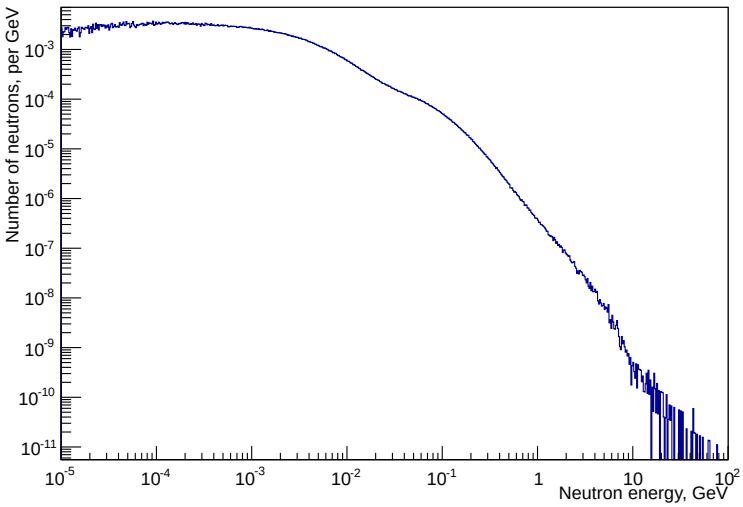

Figure 6.7: The simulated normalized energy spectrum of muon induced fast neutrons.

Figure 6.7 shows the energy spectrum of the generated neutrons. The energy spectrum is very broad and ranges from the keV to the GeV region. It peaks between $\sim 100\,\mathrm{keV}$ and $\sim 1\,\mathrm{MeV}$ and decreases afterwards with rising energy. The decrease is non exponential and has a complex structure, which is due to the fact that there are many different production processes. About 45 % of all neutrons are below 10 MeV and are thus too low energetic to produce a signal in the DSNB detection window. Hence, these neutrons do not need to be considered in the following and the effective neutron production yield is reduced to:

$$\mathrm{Y_n}(\mathrm{E} > 10\,\mathrm{MeV}) = 2.8 \cdot 10^{-4} (\mu\mathrm{g/cm^2})^{-1}. \tag{6.16}$$

Fast neutron propagation

In order to the simulate the propagation of fast neutrons into the target volume, the neutrons were started at a random position in a 4 m thick cylinder around the muon veto. Neutrons that were produced farther away from the muon veto do not need to be considered, as the mean free path length of these neutrons is below 1 m [100] and thus a large majority of them will be absorbed in the rock. When the neutron is produced close to the muon veto by an electromagnetic or hadronic shower, it is possible that a part of the shower is detected by the

causes a difference in the neutron production yield. But compared to the difference of the mean atomic weight, this effect can be neglected.

muon veto. Nevertheless, the conservative assumption was made that this shower will never be detected. The neutron energy and momentum direction was chosen randomly according to the results of the previous simulation. Only neutrons that were directed towards the target volume (2π solid angle) were simulated in order to save computation time, as previous simulation have shown that neutrons which were directed outwards contribute less than 2 % to the fast neutron rate in the target.
For each event, the visible energy was reconstructed by using the algorithm which was described in Section 3.2. Subsequently, the neutrino equivalent energy was calculated by using equation (6.3). Analogously to the simulation of the gamma background (see Section 4.2.3), the calculated photon barycenter position was smeared with a gaussian with a standard deviation according to the energy dependent position resolution [62]. Furthermore, the number of neutrons that were captured inside the target volume and the corresponding capture times were saved.
A neutron event was only considered as an IBD candidate event if exactly one neutron was captured inside the target volume and if it was captured at least 600 ns after the prompt signal, so that the energy reconstruction of the prompt signal is not disturbed by the 2.2 MeV gamma from the neutron capture. Although only one neutron was simulated per event, there is the possibility that this neutron produces secondary neutrons so that two or more neutrons are captured inside the target volume. But this is not possible in a IBD event, as the energy of the produced neutron is too low. Hence, multiple neutron capture events are indentified as fast neutron background events and are thus not considered in the following analysis.
The muon flux at 4 km w.e. depth is $\Phi_{\mathrm{P}}^{\mu} = 0.235\,\mathrm{m}^{-2}\mathrm{h}^{-1}$. Assuming that all muon tracks are vertical[5], about $1.1 \cdot 10^6$ muons per year traverse through the 4 m thick cylinder around the muon veto. The cylinder is 100 m long and thus one crossing muon produces on average 7.6 neutrons above 10 MeV in this volume. Hence, about $7.9 \cdot 10^6$ neutrons are produced in this volume per year. 2.5 billion neutrons above 10 MeV were simulated. Thus, the statistics of the simulation corresponds to about 316 years.
Figure 6.8 shows the resulting fast neutron background spectrum. The fast neutron background rate is with 492 events per 10 y in the DSNB detection window more than one of magnitude larger than the DSNB event rate for $\langle \mathrm{E}_{\nu} \rangle = 12\,\mathrm{MeV}$. Hence, the fast neutron background needs to be suppressed in order to measure the DSNB. One option is to reduce the fiducial volume, as the fast neutron background decreases with increasing distance to the production region in the surrounding rock. Table 6.2 shows the fast neutron background rate for different fiducial volume radii ranging from 11.0 m to 13.5 m. At 11.0 m fiducial volume radius, the fast neutron background is reduced to 4.9 ± 0.4(stat.) events per 10 y, which is well below the

[5]Due to the large and homegeneous overburden of the mine, this is a good assumption.

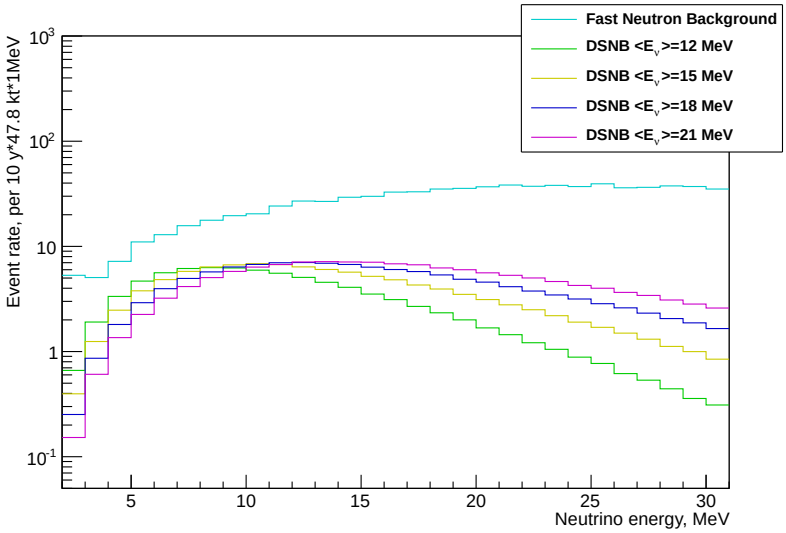

Figure 6.8: The simulated fast neutron background spectrum. For comparison, the DSNB spectra with $\langle E_\nu \rangle$ ranging from 12 MeV to 21 MeV are also depicted.

Fiducial Volume Radius [m]	Fast Neutron Background [10 y]	DSNB Signal $\langle E_\nu \rangle = 12$ MeV [10 y]
13.5	492 ± 4(stat.)	48.2
13.0	169 ± 2(stat.)	44.7
12.5	62 ± 1(stat.)	41.3
12.0	26 ± 1(stat.)	38.1
11.5	11 ± 1(stat.)	35.0
11.0	4.9 ± 0.4(stat.)	32.0

Table 6.2: The fast neutron background rates and the DSNB signal for $\langle E_\nu \rangle = 12$ MeV depending on the fiducial volume radius (9.5 MeV $< E_\nu <$ 25 MeV).

DSNB signal. But this cut also reduces the DSNB signal by $\sim 34\,\%$, so that only 32.4 events are expected for $\langle E_\nu \rangle = 12\,\mathrm{MeV}$.
Another possibility is to suppress the fast neutron background by a pulse shape analysis, which will be discussed in Section 6.5.

6.4 Neutral Current Atmospheric Neutrino Background

While the CC reactions of atmospheric $\bar{\nu}_e$ are an indistinguishable background (see Section 6.2.2), the NC reactions of atmospheric neutrinos and antineutrinos of all flavours also pose a background for the DSNB detection. This atmospheric NC background was discovered by the KamLAND experiment [101] and was not included in previous analyses [102, 44].
There are several possible reactions which contribute to the atmospheric NC background. In the reaction with the largest branching ratio, the atmospheric neutrino knocks out a neutron of a ^{12}C nucleus in the target volume:

$$\nu_x + {}^{12}C \rightarrow \nu_x + n + {}^{11}C \ , \tag{6.17}$$

which subsequently mimics the IBD event signature (see Section 6.3.2).
The reaction with the second largest branching ratio is the knock out of a neutron and a proton:

$$\nu_x + {}^{12}C \rightarrow \nu_x + n + p + {}^{10}B \ , \tag{6.18}$$

which also causes a delayed coincidence signal.

6.4.1 Simulation Setup

In order to simulate the atmospheric NC background, the interactions of the atmospheric neutrinos inside the target volume need to be simulated as a first step. As this is not possible within the GEANT4 framework, a new Monte-Carlo simulation was developed for this task. It is based on the GENIE Neutrino Monte-Carlo Generator (Version 2.6.6) [103], that is used by several other neutrino experiments like T2K [104] or IceCube [105]. The simulation used the Bartol atmospheric neutrino fluxes [106] as input, which were calculated for the location of the Super-Kamiokande experiment. As the atmospheric neutrino flux depends on the latitude, the resulting event rates need to be scaled by a factor of two to get the atmospheric neutrino NC event rate at the Pyhäsalmi location [44]. Using the simulated data, the atmospheric neutrino NC event rate R_{atmo}^{NC} was calculated to be:

$$R_{atmo}^{NC} = 5.07 \cdot 10^3 \, \frac{\mathrm{events}}{47.8\,\mathrm{kt} \cdot \mathrm{y}}. \tag{6.19}$$

For each simulated neutrino event in the target volume, the energy, the momentum direction and the vertex position of every produced final state particle was saved. Subsequently, the results were read into the GEANT4 based LENA Monte-Carlo simulation.
When an atmospheric neutrino interacts with a ^{12}C nucleus, the residual nucleus is often produced in an excited state. Unfornately, the deexcitation of an excited nucleus is not implemented in the GENIE neutrino event generator.

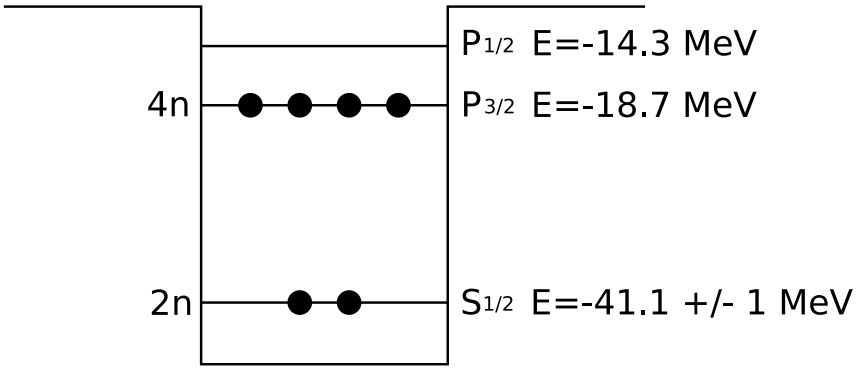

Figure 6.9: The occupation of the energy levels by neutrons in the simple shell model for ^{12}C [107].

The probability that the residual nucleus is in an excited state can be approximated, using the simple shell model. Figure 6.9 shows the occupation of the energy levels by neutrons for ^{12}C in the ground state. There are two neutrons in the $S_{1/2}$ shell at $E(S_{1/2}) = -41.7 \pm 1\,\text{MeV}$ and four neutrons in the $P_{3/2}$ shell at $E(P_{1/2}) = -18.7\,\text{MeV}$. The situation for protons is basically the same, with the difference that the energy levels are shifted upwards by 2.7 MeV due to the Coulomb repulsion. As the energy of an atmospheric neutrino is usually large compared to the binding energies of the nucleons, it is assumed in the following that the probability to interact with an atmospheric neutrino is the same for each nucleon[6]. After the neutrino has interacted with a nucleon, the nucleon can scatter with other nucleons before it leaves the nucleus. Due to these so-called intranuclear scattering reactions, further nucleons can be emitted. In the following, it was assumed that only nucleons from the $P_{3/2}$ shell are emitted in these reactions. Thus, there is a $\frac{2}{6} \cong 33\,\%$ chance that the residual nucleus has a hole in the $S_{1/2}$ neutron or proton shell.

[6]The coherent scattering of the neutrino with the whole nucleus can be neglected, as the transferred energy is too low in this case.

The excitation energy of the residual nucleus is $E^* = 23 \pm 1\text{MeV}$ and has a width of $\Gamma = 12\,\text{MeV}$ [108]. As the excitation energy is above the neutron separation energy $S_n = 18.7\,\text{MeV}$ and above the proton separation energy $S_p = 16.0\,\text{MeV}$, the nucleus will deexcite mainly via the emission of protons, neutron and heavier nuclear particles like deuterons or alphas [107]. Using the nuclear reaction program TALYS (Version 1.4) [109], the branching ratios for the different possible deexcitation channels were calculated for each possible residual nucleus and read into the GEANT4 Monte Carlo simulation.
Afterwards, the atmospheric neutrino NC events were simulated with the GEANT4 simulation, using the results of the neutrino interaction simulation. For 33 % of all simulated events, the residual nucleus was assumed to be in an excited state and the final state particles of the corresponding deexcitation channel were also simulated in this case. Analogous to the simulation of the fast neutron background (see Section 6.3.2), the neutrino equivalent energy was reconstructed and the number and times of the neutron captures in the target volume were saved. Again, only events with exactly one neutron capture which was at least 600 ns after the prompt signal were considered as background events for the DSNB detection.

6.4.2 Background Rates

Figure 6.10 shows the simulated background spectrum from the NC reactions of atmospheric neutrinos. The atmospheric neutrino NC background surpasses the DSNB signal by more than one order of magnitude over the whole detection window. The spectrum rises with the energy till it peaks around $5 - 10\,\text{MeV}$ and decreases slowly afterwards. Overall, $3.27 \cdot 10^3$ background events per 10 y are expected in the DSNB detection window between 9.5 MeV and 25 MeV for a fiducial volume with 13.5 m radius. Hence, the NC reactions of atmospheric neutrino are a dangereous background, which needs to be suppressed in order to measure the DSNB.
The KamLAND experiment has measured $3.26^{+1.28}_{-1.19}$ atmospheric neutrino NC events per $\text{kt} \cdot \text{y}$ between 8.3 MeV and 30.8 MeV neutrino equivalent energy [101]. The simulated event rate for LENA in this energy window is $9.00\,\frac{\text{events}}{\text{kt}\cdot\text{y}}$. Considering that the assumed atmospheric neutrino flux was twice as large as in KamLAND, this result is in agreement with the KamLAND data, which shows that this complex simulation returns reliable results.
A possible background suppression method is to look for the coincidence of atmospheric neutrino NC event with the subsequent decay of any produced radioactive isotope. Table 6.3 shows the branching ratios of the different atmospheric NC background channels in the DSNB detection window. Note that although two neutrons are produced in reaction (7), only one neutron is captured on hydrogen or carbon after 600 ns. The other neutron is absorbed by carbon in an inelastic

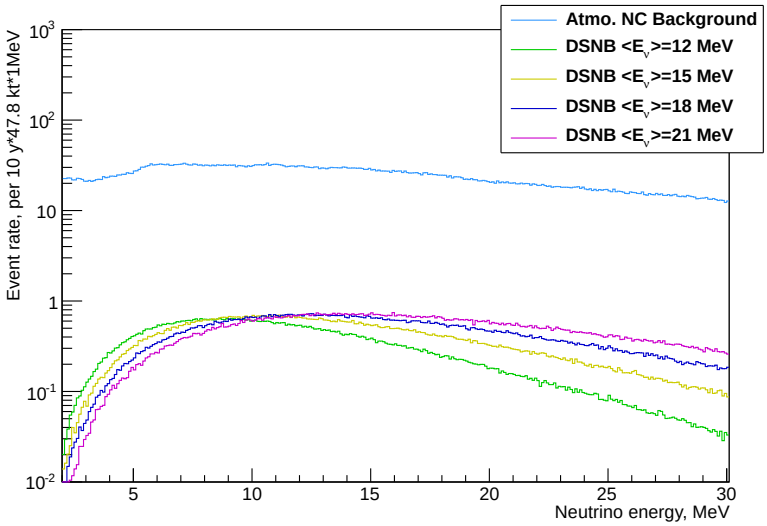

Figure 6.10: The simulated atmospheric neutrino NC background spectrum. For comparison, the DSNB spectra with $\langle E_\nu \rangle$ ranging from 12 MeV to 21 MeV are also depicted.

Reaction channel	Branching ratio
(1) $\nu_x + {}^{12}C \rightarrow \nu_x + n + {}^{11}C$	38.8 %
(2) $\nu_x + {}^{12}C \rightarrow \nu_x + p + n + {}^{10}B$	20.4 %
(3) $\nu_x + {}^{12}C \rightarrow \nu_x + 2p + n + {}^{9}Be$	15.9 %
(4) $\nu_x + {}^{12}C \rightarrow \nu_x + p + d + n + {}^{8}Be$	7.1 %
(5) $\nu_x + {}^{12}C \rightarrow \nu_x + \alpha + p + n + {}^{6}Li$	6.6 %
(6) $\nu_x + {}^{12}C \rightarrow \nu_x + 2p + d + n + {}^{7}Li$	1.3 %
(7) $\nu_x + {}^{12}C \rightarrow \nu_x + 3p + 2n + {}^{7}Li$	1.2 %
(8) $\nu_x + {}^{12}C \rightarrow \nu_x + d + n + {}^{9}B$	1.2 %
(9) $\nu_x + {}^{12}C \rightarrow \nu_x + 2p + t + n + {}^{6}Li$	1.1 %
(10) $\nu_x + {}^{12}C \rightarrow \nu_x + \alpha + n + {}^{7}Be$	1.1 %
(11) $\nu_x + {}^{12}C \rightarrow \nu_x + 3p + n + {}^{8}Li$	1.1 %
other reaction channels	4.2 %

Table 6.3: The branching ratios of the different atmospheric NC background channels in the DSNB detection window.

reaction without emitting any characteristic gammas, e.g.:

$$\mathrm{n} + {}^{12}\mathrm{C} \rightarrow {}^{12}\mathrm{B} + \mathrm{p} \ . \tag{6.20}$$

^{11}C (β^+, $\tau = 29.4\,\mathrm{min}$) is produced in 38.8 % of all atmospheric NC events (reaction (1)). The Q-Value of the ^{11}C β^+ decay is 1.0 MeV and therefore it can be detected with a high efficiency. Thus, more than 99 % of all atmospheric NC events with ^{11}C in the final state can be rejected if the following cut is applied. After each IBD candidate event a volume with 0.5 m radius around the reconstructed event position is vetoed for $\Delta\mathrm{t} = 7 \cdot \tau(^{11}\mathrm{C})$. If an event with a visible energy between 0.8 MeV and 2.2 MeV is detected in this volume during this period of time, the IBD candidate event will be tagged as atmospheric NC background. For 13.5 m fiducial volume radius, the probability for an accidental coincidence of an IBD event with an external gamma event is too large to apply this cut. But if the fiducial volume radius is set to 11 m, the gamma background is suppressed so that only 0.9 % of the IBD events are wrongly tagged as atmospheric NC background.
A similar cut can be applied to tag ^{8}Li that is produced in reaction (11). But the other isotopes that can be produced in the NC reaction of an atmospheric neutrino are either stable (^{10}B, ^{9}Be, ^{7}Li, ^{6}Li), have a too long life time (^{7}Be, $\tau = 76.9\,\mathrm{d}$) or decay almost instantly (^{9}B, ^{8}Be).
Hence, the atmospheric NC background can only be reduced by about 40 % by looking for the coincident decay of a radioactive isotope. But as the atmospheric NC background is more than one order of magnitude larger than the DSNB signal, this is not enough to detect the DSNB.
Thus, a better background suppression method is needed. A possible option is to reject atmospheric neutrino NC events by analyzing their pulse shape, as protons, neutrons and alphas have a different typical pulse shape than positrons. This method will be discussed in detail in the next Section.

6.5 Pulse Shape Discrimination of Background Events

Heavier particles, like protons, neutrons[7] or alphas, have a different pulse shape than positrons. This can be used to discriminate fast neutron and atmospheric neutrino NC events from IBD events. It was already demonstrated in Chapter 5 that alphas can be discriminated from electron recoil events with a high efficiency.

[7]Neutrons do not directly emit scintillation light, as they do not carry any electric charge. Instead, they scatter elastically on protons, which subsequently emit scintillation light. Futhermore, they can produce gammas and nuclear fragments in inelastic scattering reactions on carbon.

Parameter	Electrons/Positrons	Protons
N_1	0.669	0.612
N_2	0.188	0.213
N_3	0.143	0.175
τ_1	6.8 ns	7.0 ns
τ_2	26.5 ns	27.3 ns
τ_3	152.3 ns	140.3 ns
k_b	$0.15 \frac{mm}{MeV}$	$0.12 \frac{mm}{MeV}$

Table 6.4: The photon emission parameters for electrons and protons [110]. The k_b value for protons was taken from a calibration measurement in the Borexino experiment, which uses PC as scintillator [111].

But discriminating neutrons and protons, which are mainly emitted in an atmospheric neutrino NC event (see Table 6.3), from positrons is more challenging as they have a lower mass than alphas and thus the difference to the positron pulse shape is smaller.

Table 6.4 shows the parameters of the photon emission PDF (see Section 3.1.2) that were used for the simulation of electrons, positrons and protons. The PDF for deuterons was not measured up to now, but as deuterons are heavier than protons, the difference between the electron and deuteron PDF should be larger than for protons. Hence, the proton PDF was also used for deuterons, which is a conservative assumption. For alphas, the PDF according to Table 3.2 was used.

Figure 6.11 shows a comparison between the average pulse shapes of neutron and IBD events in the center of the detector, after the TOF correction was applied (see Section 3.2). The average visible energy of the events was 9.2 MeV, which corresponds to a $\bar{\nu}_e$ with 10 MeV. While a clear difference between the two pulse shapes is visible, it is much smaller than the difference between the electron and alpha pulse shapes (see Figure 5.1). But the visible energy is also much higher compared to the ^{210}Po alpha background (see Section 5.2), so that the statistical fluctuations of the pulse shapes are smaller. Hence, even a small difference between the two pulse shapes can be sufficient to distinguish between neutron and IBD events.

Figure 6.12 shows the tail-to-total ratio distribution (see Section 5.1.1) for IBD and neutron events in the center of LENA with $E_{vis} = 9.2$ MeV. While a clear difference between the two distributions is visible, there is also large overlap. Hence, it is not possible to discriminate neutron background events with a high effficiency, without reducing the detection efficiency for IBD events. Nevertheless, it shows the potential of the pulse shape discrimination to reduce the fast neutron and the

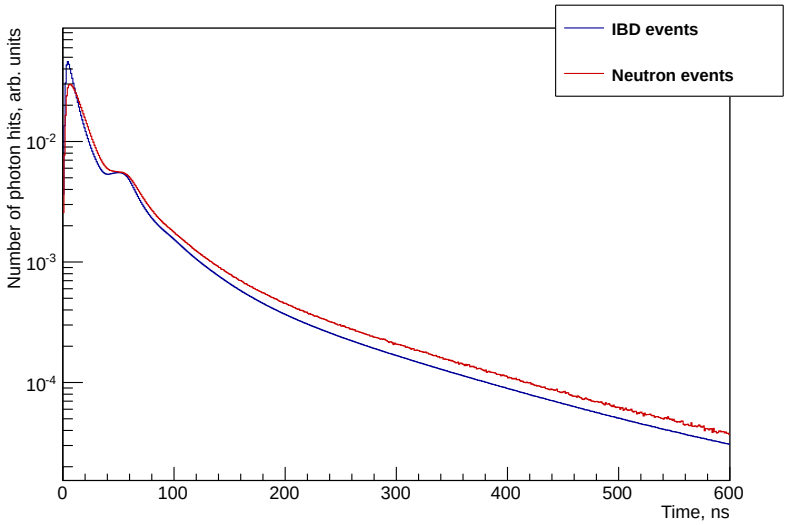

Figure 6.11: Comparison between the average normalized pulse shape of IBD (denoted in blue) and neutron (denoted in red) events in the center of LENA with $E_{vis} = 9.2\,MeV$.

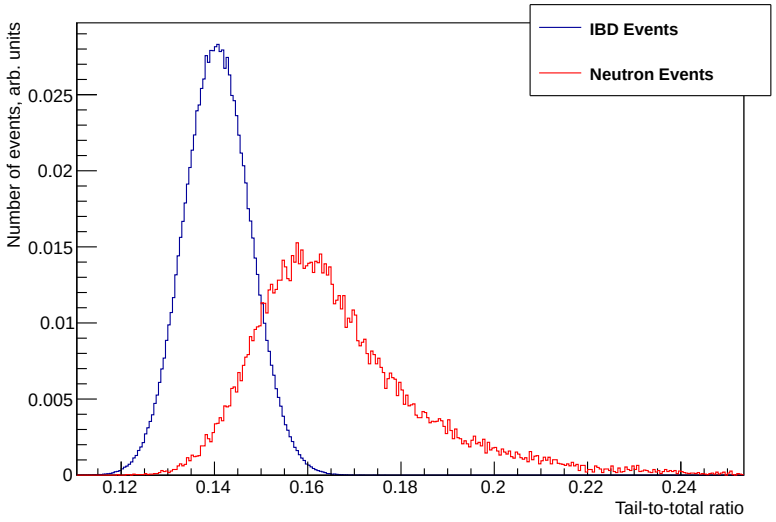

Figure 6.12: The tail-to-total ratio distribution for IBD (denoted in blue) and neutron events (denoted in red) in the center of LENA with $E_{vis} = 9.2\,MeV$.

IBD acceptance	Rate [10 y] tail-to-total method	Rate [10 y] gatti method	Rate [10 y] combined method
95.0 %	64.4 ± 1.4(stat.)	221 ± 3(stat.)	77.4 ± 1.6(stat.)
90.0 %	46.6 ± 1.2(stat.)	218 ± 3(stat.)	40.4 ± 1.1(stat.)
80.0 %	30.8 ± 1.0(stat.)	215 ± 3(stat.)	23.5 ± 0.9(stat.)
55.0 %	13.8 ± 0.7(stat.)	213 ± 3(stat.)	10.9 ± 0.6(stat.)
50.0 %	11.8 ± 0.6(stat.)	213 ± 3(stat.)	9.4 ± 0.5(stat.)
40.0 %	8.6 ± 0.5(stat.)	212 ± 3(stat.)	7.4 ± 0.5(stat.)

Table 6.5: The fast neutron background rate in the DSNB detection window for different pulse shape discrimination methods. In the combined method, the pulses are analyzed with both the tail-to-total and the gatti method. Without pulse shape discrimination, the fast neutron rate is 492 ± 4(stat.) events per 10 y.

atmospheric neutrino NC background.

In order to calculate the gatti parameter (see Section 5.1.2), several calibration runs were performed, using neutrons with mean visible energies ranging from 9.2 MeV to 29.2 MeV. Subsequently, the gatti parameter for a fast neutron or atmospheric NC event was calculated according to Section 5.2.1.

Table 6.5 shows the fast neutron background rate after the pulse shape discrimination, using the tail-to-total and the gatti method analogous to Section 5.2.1. Furthermore, the results for a combined method, where the tail-to-total and gatti cut are applied consecutively, are also depicted.

For 95 % IBD acceptance, the tail-to-total method reduces the fast neutron background from 492 ± 4(stat.) to 64.4 ± 1.4(stat.) events per 10 y. Contrary to the $\alpha - \beta$ discrimination (see Section 5.2), the performance of the gatti method is significantly worse with a reduction of the fast neutron background to 221 ± 3(stat.) events per 10 y. A possible explanation for this effect is that fast neutrons can undergo several reactions inside the scincillator. For example, a fast neutron can transfer almost all of its energy in one elastic scattering interaction with a proton, or in several individual elastic scattering reactions which are few ns apart. Furthermore, it can interact inelastically with a carbon nucleus, producing gammas, protons, deuterons and alphas. Each of these reactions has a different typical pulse shape and depending on the branching ratio of the reaction, the gatti weights are more or less optimized for it. Hence, it not possible to distinguish the pulse shapes of some neutron reaction channels from the IBD pulse shape with the gatti method. Thus, the gatti parameter distribution of the neutrons is very broad compared to the IBD events (see Figure 6.13) and the overall performance is worse than the tail-to-total method.

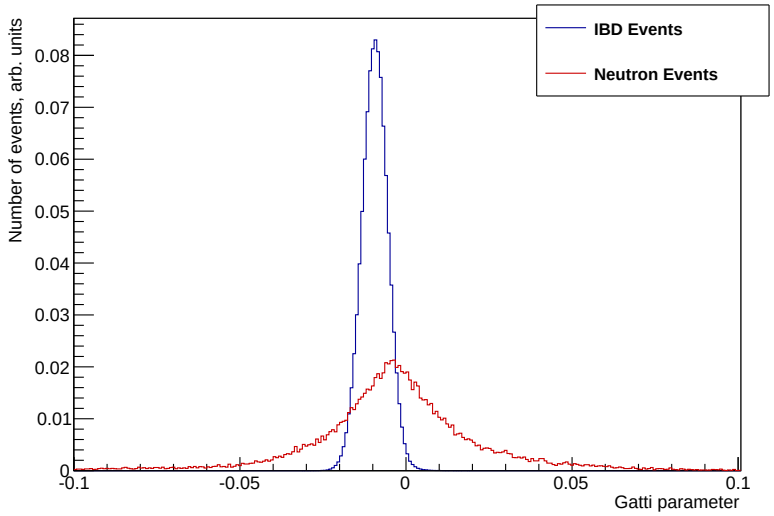

Figure 6.13: The gatti parameter distribution for IBD (denoted in blue) and neutron events (denoted in red) in the center of LENA with $E_{vis} = 9.2\,\text{MeV}$.

But as the gatti method works very well for the reaction channels with a high branching ratio, the discrimination efficiency of the tail-to-total method can be improved if the gatti method is applied afterwards. Using this combined method, the fast neutron background rate is reduced to 23.5 ± 0.9(stat.) events per 10 y for 80 % IBD acceptance, which is almost a factor of two better than the tail-to-total method and a factor of ten better than the gatti method, respectively. Nevertheless, this reduction is still not enough, so that a fiducial volume cut also has to be applied. Hence, in the following, the fiducial volume radius is set to 13.0 m, so that the fast neutron background rate is reduced to 4.4 ± 0.8(stat.) events per 10 y for 80 % IBD acceptance, which is in the same range as the atmospheric $\bar{\nu}_e$ and the reactor neutrino background (see Section 6.2.1 and Section 6.2.2). Due to these cuts, the DSNB signal is reduced by 25 % to 35.8 events per 10 y.

Table 6.6 shows the atmospheric NC background rate after the pulse shape discrimination, using the combined method. For 95 % IBD acceptance, the atmospheric NC rate is only reduced by a factor of ~ 3 to $1.0 \cdot 10^3$ events per 10 y, while the fast neutron rate was reduced by a factor of ~ 6 by this cut. If a more restrictive pulse shape cut with 55 % IBD acceptance is applied, the atmospheric NC rate is reduced by a factor of ~ 70 to 43.5 ± 0.5(stat.) events per 10 y. As the DSNB signal is also reduced, the background is still a factor of about two larger than the DSNB signal. Using a pulse shape cut with 40 % IBD acceptance, the atmospheric NC rate can be reduced to 21.8 ± 0.4(stat.) events per 10 y, such that is only slightly

IBD acceptance	Atmospheric NC rate [10 y]	DSNB Signal $\langle E_\nu \rangle = 12\,\text{MeV}$ [10 y]
95.0 %	1001 ± 3(stat.)	42.5
90.0 %	378 ± 2(stat.)	40.2
80.0 %	155 ± 1(stat.)	35.8
55.0 %	43.5 ± 0.5(stat.)	24.6
50.0 %	34.4 ± 0.5(stat.)	22.4
45.0 %	27.4 ± 0.5(stat.)	20.1
40.0 %	21.8 ± 0.4(stat.)	17.9

Table 6.6: The atmospheric NC backgrounds depending on the IBD acceptance, using the combined pulse shape discrimination method. For comparison, the corresponding DSNB event rates for $\langle E_\nu \rangle = 12\,\text{MeV}$ is also depicted. Without pulse shape discrimination, the atmospheric NC rate amounts to $3.0 \cdot 10^3$ events per 10 y.

larger than the DSNB signal. Due to this cut, the fast neutron background rate is also further reduced to 1.8 ± 0.2(stat.) events per 10 y.

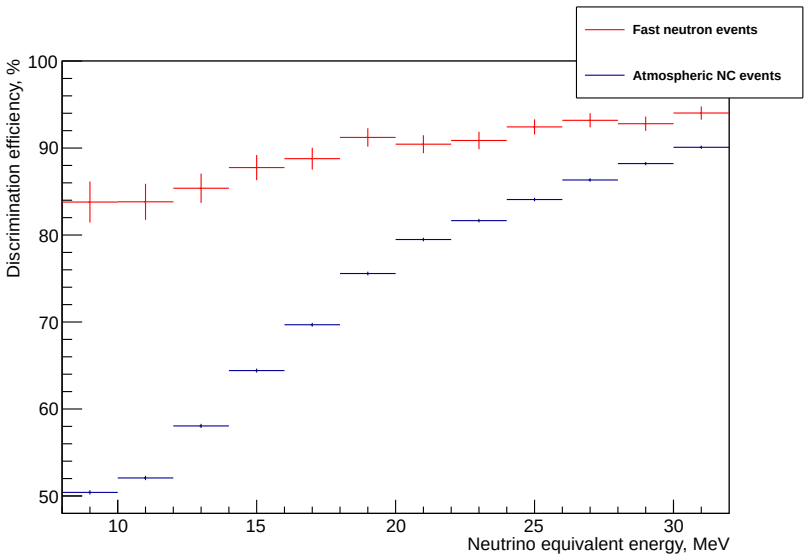

Figure 6.14: The energy dependent pulse shape discrimination efficiency for fast neutron and atmospheric NC events, using the combined method with 95 % acceptance.

Figure 6.14 shows the energy dependent pulse shape discrimination efficiency for

fast neutron and atmospheric NC events, using the combined method with 95 % acceptance. As expected, the discrimination efficiency for both fast neutron and atmospheric NC events rises with the visible energy, due to the increased photon statistics.

This is one reason for the better performance of the pulse shape discrimination for fast neutron events than for atmospheric NC events, as a larger fraction of the fast neutron events are in the upper half of the DSNB detection window compared to the atmospheric NC events (see Figure 6.8 and Figure 6.10).

Overall, the discrimination efficiency for fast neutron events is always higher than for atmospheric NC events. One reason for this is that the used gatti weights were calculated from positron and neutron events. Only 40 % of all atmospheric NC events have only a neutron in the final state (see Table 6.3), while the remaining events have multiple particles in the final state. Hence, the used gatti weights are more optimized for fast neutron events than for atmospheric events[8].

Another reason is that a larger fraction of the fast neutrons undergo inelastic scattering reactions on carbon compared to the neutrons that are emitted in an atmospheric NC event, as the energy of the fast neutrons is higher. Alpha particles can be emitted in these inelastic scattering reactions, such that the visible energy is quenched into the DSNB detection window. As the difference between the alpha and the electon-like positron pulse shape is much larger, these events can be discriminated with a higher efficiency compared to events where the neutron scattered elastically off a proton.

Figure 6.15 shows the resulting atmospheric NC spectrum after the combined pulse shape discrimination method with 40 % IBD acceptance was applied. Around 10 MeV neutrino equivalent energy, the atmospheric NC rate is still a factor of ~ 2 larger than the DSNB rate. But due to the rising discrimination efficiency it drops faster with increasing energy than the DSNB rate. Depending on the mean supernova neutrino energy, the atmospheric NC rate drops below the DSNB signal between 14 and 18 MeV. Hence, the atmospheric NC background could be further reduced if the lower limit of the DSNB detection is increased to 18 MeV. But this would reduce the already low DSNB event rate for $\langle E_\nu \rangle = 12$ MeV to less than 6 events per 10 y, which would be too small for a statistical significant detetection. Thus, it is not possible to further reduce the atmospheric NC background by diminishing the size of the DSNB detection window.

[8] The simulation of atmospheric NC events takes more computation time than the simulation of neutron events. Hence, it would take too much time to simulate calibration runs with atmospheric NC events, which would be needed to calculate gatti weights that are better optimized for the discrimination of atmospheric NC events.

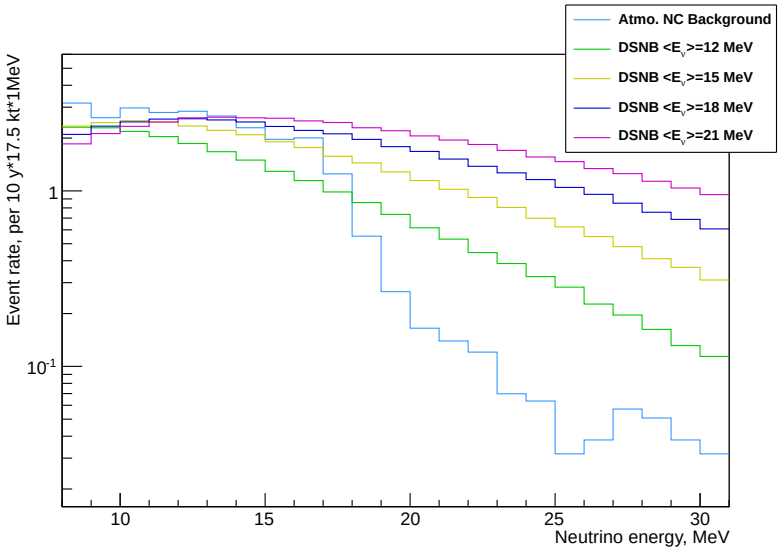

Figure 6.15: The atmospheric NC background spectrum after the combined pulse shape discrimination method with 40 % IBD acceptance was applied. For comparison, the DSNB spectra with $\langle E_\nu \rangle$ ranging from 12 MeV to 21 MeV are also depicted.

6.6 Detection Potential

Table 6.7 summarizes the contribution of the different background sources, using the combined pulse shape discrimination method with 40 % IBD acceptance and 13.0 m fiducial volume radius. Overall, 27.8 background events per 10 y are expected in the DSNB detection window, while the predicted DSNB rate ranges from 17.9 ($\langle E_\nu \rangle = 12$ MeV) to 35.2 ($\langle E_\nu \rangle = 21$ MeV) events per 10 y. Hence, it is clear that a detection of the DSNB is very challenging, especially for the case of $\langle E_\nu \rangle = 12$ MeV.

In a first step, it is assumed that the expected background rates are known without any uncertainty. While this of course unrealistic, it should be possible to determine the expected background rates with high precision. The reactor neutrino rate in the DSNB detection window can be extrapolated from the measured rate below 9.5 MeV. Analogously, the atmospheric $\bar{\nu}_e$ rate in the DSNB detection window can be estimated from the measured rate at higher energies.

As the fast neutron rate decreases with the radius of the fiducial volume, it can be determined by analyzing the dependence of the event rate on the radius of the reconstructed position. Another option is to look for IBD-like events, that were detected in coincidence with a muon which crossed the muon veto. Although the fast neutron rate can not be calculated directly from these events, they can still

Background source	Rate [10 y]
Reactor neutrinos	2.0
Atmospheric $\bar{\nu}_e$	2.2
^{9}Li $\beta^- - n$	< 0.01
Fast neutrons	1.8
Atmospheric NC	21.8
Sum	27.8
DSNB ($\langle E_\nu \rangle = 12$ MeV)	17.9

Table 6.7: The background rates in the DSNB detection window between 9.5 MeV and 25 MeV for the different sources, using the combined pulse shape discrimination method with 40 % IBD acceptance and 13.0 m fiducial volume radius.

be used to validate the Monte-Carlo simulation. Subsequently, the expected fast neutron rate can be calculated by using the validated Monte Carlo simulation.

Measureing the atmospheric NC event rate is challenging, as the efficiency of the applied pulse shape cut must be known with high precision. A possible option is to look for events in the center of the detector, where two neutron captures were detected, as these events can only be due to atmospheric neutrino NC reactions. While the efficiency for IBD-like atmospheric NC events cannot be calculated directly from these events, they can also be used to validate the Monte-Carlo simulation. Subsequently, the atmospheric NC event rate can be calculated with this validated Monte-Carlo simulation.

As the determination of the fast neutron rate and the atmospheric NC rate is quite complicated, the DSNB detection window should be blinded during the first 10 y of data taking. During this time period, the analysis procedure should be fixed by looking at the events that are outside the energy window, or by analyzing the events that have two or more neutron captures. After the detection window has been unblinded, the analysis procedures are applied without any changes. Otherwise, there would be the danger to introduce an experimental bias [112].

From the number of detected events and the expected background rate, the confidence interval for the DSNB rate can be calculated by using the Feldman-Cousins method [113]. By increasing the size of the confidence interval such that the lower limit is almost zero, the significance of the detection of the DSNB can be calculated.

Table 6.8 shows the expected detection signifance for different DSNB models with $\langle E_\nu \rangle$ ranging from 12 MeV to 21 MeV, using the Feldmann-Cousins method. For each DSNB model, it was assumed that the number of detected events equals the sum of the expected number of DSNB and background events. If $\langle E_\nu \rangle = 12$ MeV,

$\langle E_\nu \rangle$	Expected DSNB events [10 y]	Expected DSNB detection significance
12 MeV	17.9	$3.3\,\sigma$
15 MeV	25.7	$4.3\,\sigma$
18 MeV	31.5	$5.2\,\sigma$
21 MeV	35.2	$5.7\,\sigma$

Table 6.8: The expected detection significance for different DSNB models with $\langle E_\nu \rangle$ ranging from 12 MeV to 21 MeV, assuming that the expected background rates are perfectly known.

$\langle E_\nu \rangle$	5 % background uncertainty	10 % background uncertainty	25 % background uncertainty
12 MeV	$3.0\,\sigma$	$2.7\,\sigma$	$1.9\,\sigma$
15 MeV	$4.0\,\sigma$	$3.7\,\sigma$	$2.6\,\sigma$
18 MeV	$4.9\,\sigma$	$4.4\,\sigma$	$3.1\,\sigma$
21 MeV	$5.4\,\sigma$	$4.9\,\sigma$	$3.5\,\sigma$

Table 6.9: The expected detection significance for different DSNB models with $\langle E_\nu \rangle$ ranging from 12 MeV to 21 MeV, assuming that the expected background rates are known with 5 to 25 % precision.

the DSNB can be detected with an expected significance of $3.3\,\sigma$ after 10 y data taking. As the number of detected events is subject to statistical fluctuations, the detected significance can of course be larger or smaller. The expected detection significance rises with the mean supernova neutrino energy, and is above $5\,\sigma$ for $\langle E_\nu \rangle > 18$ MeV.

Up to now, it was assummed that the number of expected background events is known. A more realistic scenario is that the expected background rate is only known with a certain precision. In this case, the detection significance can be calculated according to [114]. Table 6.9 shows the expected detection significance for different DSNB models with $\langle E_\nu \rangle$ ranging from 12 MeV to 21 MeV, assuming that the expected background rates are known with 5 to 25 % uncertainty.

If the background is known with 25 % uncertainty, the DSNB detection significance is dramatically reduced such that a $3\,\sigma$ detection of the DSNB after 10 y is only possible for $\langle E_\nu \rangle >= 18$ MeV. For 10 % background uncertainty, a $3\,\sigma$ detection is possible for $\langle E_\nu \rangle >= 15$ MeV. In case that the background uncertainty is 5 %, the DSNB can be detected with $3\,\sigma$ significance for each DSNB model and with more than $5\,\sigma$ significance for $\langle E_\nu \rangle = 21$ MeV.

Hence, the background needs to be known with a uncertainty of less than 5 % in order to detect the DSNB. Thus, the pulse shape discrimination efficiency for atmospheric NC events needs to be known with $\sim 0.1\,\%$ precision, which should be possible but is very challenging.

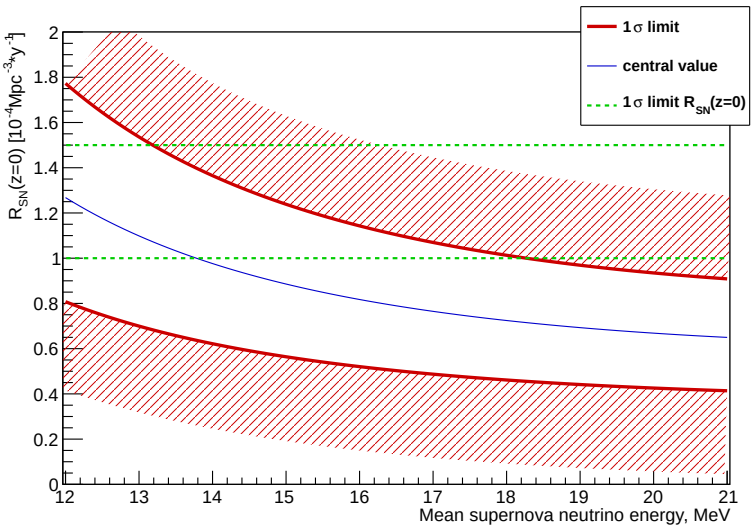

Figure 6.16: The $1\,\sigma$ confidence interval for the supernova rate $\mathrm{R_{SN}(z=0)}$ and the mean supernova neutrino energy, assuming 5 % background uncertainty and that 46 IBD events ($\langle \mathrm{E}_\nu \rangle = 12\,\mathrm{MeV}$) were detected. For comparison, the current $1\,\sigma$ confidence interval for $\mathrm{R_{SN}(Z=0)}$ is also depicted (green dashed line).

As the DSNB event rate is very small and a factor of two below the background rate, it will probably not be possible to directly determine $\langle \mathrm{E}_\nu \rangle$ from the energy distribution of the detected events. Nevertheless, it is possible to extract some information about the redshift dependent supernova rate ($\mathrm{R_{SN}}$) and $\langle \mathrm{E}_\nu \rangle$ from the number of detected events. Figure 6.16 shows the $1\,\sigma$ confidence interval for the supernova rate $\mathrm{R_{SN}(z=0)}$ and the mean supernova neutrino energy, assuming 5 % background uncertainty and that 46 IBD like events ($\langle \mathrm{E}_\nu \rangle = 12\,\mathrm{MeV}$) were detected. The redshift dependent supernova rate is already known with 25 % uncertainty (see Section 1.4) and it is very likely that the uncertainty will be reduced during the next 20 years. Hence, it will be possible to determine $\langle \mathrm{E}_\nu \rangle$ from the number of detected events, though the uncertainty will be quite large.
In case that no DSNB signal is detected, the current limit on the DSNB flux of the Super-Kamiokande experiment could be significantly improved. Assuming that 28 events are detected after 10 y and that the background is known with 5 % uncertainty, the upper limit on the DSNB rate would be $26.4\,\frac{\mathrm{events}}{47.8\,\mathrm{kt}\cdot 10\,\mathrm{y}}$ (90 % C.L.).

Hence, the upper limit on the DSNB flux above 17.3 MeV would be $0.4\,\bar{\nu}_e\,\mathrm{cm}^{-2}\mathrm{s}^{-1}$ for $\langle E_\nu \rangle = 18\,\mathrm{MeV}$, which is a factor of about 8 below the current limit (see Section 1.5.1). Even in a pessimistic scenario of 25 % background uncertainty, the flux limit could be improved by a factor ~ 5 to $0.6\,\bar{\nu}_e\,\mathrm{cm}^{-2}\mathrm{s}^{-1}$.

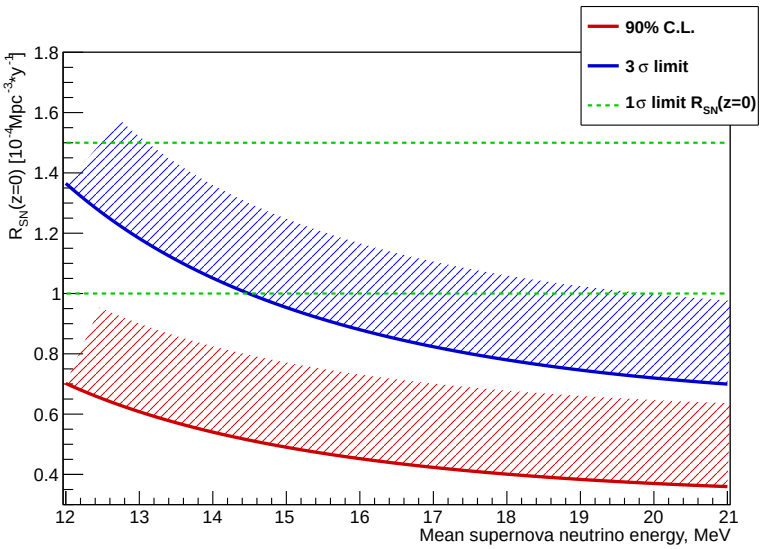

Figure 6.17: The $3\,\sigma$ (depicted in blue) and 90 % C.L. (depicted in red) exclusion contours for the supernova rate $R_{SN}(z = 0)$ and the mean supernova neutrino energy, assuming 5 % background uncertainty and that no DSNB signal was detected ($N_{det} = \langle N_{bg} \rangle$). For comparison, the current $1\,\sigma$ confidence interval for $R_{SN}(z = 0)$ is also depicted (green dashed line).

Figure 6.17 shows the exclusion contours for the supernova rate $R_{SN}(z = 0)$ and the mean supernova neutrino energy, assuming 5 % background uncertainty and that no DSNB signal was detected. The whole current parameter space would be excluded with 90 % C.L. and a huge part of the parameter space would be excluded with $3\,\sigma$ signficance. Hence, if no excess above the expected number of background events in the DSNB detection window is found in LENA, all current standard DSNB models would be ruled out with more than 90 % C.L.

Chapter 7

Conclusions

During the last decade, the Borexino [27] and KamLAND [51] experiments have demonstrated the great potential of the liquid scintillator technology. As the target mass of these experiments is rather small with 278 t and 1 kt, LENA (**L**ow **E**nergy **N**eutrino **A**stronomy) has been proposed as a next generation 50 kt liquid scintillator detector. Its main physics goals are the detection of solar neutrinos, supernova neutrinos, geoneutrinos, and the search for the proton decay.
One major focus of the present work is the test of the MSW-LMA prediction [12] for the electron neutrino survival probability P_{ee} by measuring solar ^{8}B neutrinos [20]. This test is important as new physics could influence P_{ee} in the transition region between vacuum and matter dominated oscillations ($2\,\mathrm{MeV} < E_\nu < 5\,\mathrm{MeV}$). Due to the huge target mass of the LENA detector, external gamma background, which limits the detection threshold in Borexino for elastic scattering reactions of ^{8}B neutrinos with electrons to 3 MeV electron recoil energy, can be suppressed by reducing the fiducial volume. Hence, an unprecedentedly low detection threshold of 2 MeV could be achieved in LENA, allowing a rigorous test of the MSW-LMA prediction in the transition region.
As a prerequisite for the ^{8}B analysis, an energy reconstruction algorithm was developed, which uses the information of several simulated calibration runs at different energies between 0.3 MeV and 1.0 MeV. The algorithm was tested with a full detector Monte Carlo simulation based on GEANT4 [72] and no systematic shift between the reconstructed and the true energy was found at 1 MeV. The obtained energy resolution is $\sigma_E = 6.2\,\% \cdot \sqrt{E/\mathrm{MeV}} + 0.3\,\%$. Above 1.5 MeV, a small systematic shift between the reconstructed and the true energy of 0.5 % to 1.0 % was found, which is due to the fact that the maximum energies of the calibration runs was 1 MeV. Hence, an extensive calibration campain using many sources with a wide distribution of energies will be needed.
Afterwards, the electron recoil spectra of solar neutrinos were simulated, using the flux predictions of the BS05(AGS,OP) standard solar model [14]. Besides

the elastic neutrino electron scattering (ES) channel, which was used for the ^{8}B measurement in Borexino [29] and Super-Kamiokande [41], LENA can also detect the CC reactions of electron neutrinos on ^{13}C. This detection channel has the advantage that the subsequent decay of the ^{13}N nuclei produced can be used to reduce the background by a coincidence measurement. Another advantage is that the neutrino energy can be measured directly. This is not possible in the ES channel, as only the energy of the recoiling electron is measured so that the signal at each electron recoil energy is a convolution of different neutrino energies. The disadvantage of the ^{13}C channel is that the event rate is with $\frac{675\,\text{counts}}{47.8\,\text{kt}\cdot\text{y}}$ almost two orders of magnitude lower than the event rate of the ES channel ($\frac{6.2\cdot10^4\,\text{counts}}{47.8\,\text{kt}\cdot\text{y}}$).

In addition, different background sources were studied. There are three different types of backgrounds for the ES channel: cosmogenic radioisotopes, which are produced in-situ by crossing muons, intrinsic radioactivity and external gamma rays. For the cosmogenic radioisotopes, the results of the Borexino experiment [29, 27] were scaled to the expected muon flux at the mine in Pyhäsalmi, the most probable location for LENA. The ^{10}C background can be reduced to about 1 count per 47.8 kt · y by vetoing a cylinder with 2 m radius around each traversing cosmic muon for $\sim$ 110 s, which also reduces the ^{11}Be background to less than 0.01 count per 47.8 kt · y. As only a small volume around each muon is vetoed, the dead time introduced amounts to an acceptable level of 9.1 %. After this cut, the ^{11}C rate is still more than one order of magnitude higher than the ^{8}B signal, which limits the measurement of the ^{8}B spectrum to above 2 MeV.

Above 2 MeV, the only remaining intrinsic radioactive isotope is ^{208}Tl[1]. Assuming that the same radiopurity levels ($c(^{232}\text{Th}) = (6.5 \pm 1.5) \cdot 10^{-18}\text{g/g}$) as in Borexino[2] [29] are achieved, the ^{208}Tl spectrum surpasses the ^{8}B signal between $\sim$ 3 MeV and $\sim$ 5 MeV by up to 50 %.

Using the radioimpurity levels of the Borexino PMTs [92], light concentrators and of the concrete at the LNGS [52], the external gamma background was simulated. The resulting external gamma background rate surpasses the ^{8}B signal by several orders of magnitude below $\sim$ 3 MeV electron recoil energy, while no background was present above 3.5 MeV electron recoil energy. Hence, the fiducial volume radius was set to 9 m for electron recoil energies between 2.0 MeV and 3.5 MeV in order to suppress the external gamma background to less than one event per day, reducing the fiducial mass from 47.8 kt to 19.2 kt. For higher electron recoil energies, the full fiducial volume was used.

[1] While ^{214}Bi has a Q-Value of 3.3 MeV, it can be tagged through the subsequent decay of the ^{214}Po daughter nucleus.

[2] Note that the radiopurity levels of the first data taking phase of Borexino are used and that the current radioactive background rates in Borexino are much lower due to the several purification campaigns.

Accidental coincidences of background as well as ES events provide a background for the neutrino detection via the ^{13}C channel. Using the simulated spectra, the accidental background was calculated for a fiducial volume with 11 m radius, which reduces the event rate to 425 counts per year. Below ~ 5 MeV neutrino equivalent energy, which is the sum of the energy of the prompt event and of the Q-Value of the CC reaction ($\nu_e + {}^{13}C \rightarrow {}^{13}N + e^-$, Q = 2.2 MeV), the accidental background is more than two orders of magnitude larger than the ^{8}B signal. Hence, the measurement of the ^{8}B spectrum is limited to above 5 MeV in the ^{13}C channel.

Using the simulated neutrino and background spectra according to the MSW-LMA prediction, 10^5 measurements of the ^{8}B neutrino spectrum were simulated. This simulated data was fitted with the expected spectrum according to the MSW-LMA prediction, including all relevant background sources. The ^{8}B rate was reconstructed with ~ 0.2 % statistical error after 5 y, which is a factor of ~ 5 better than the current statistical error of the Super-Kamiokande measurement [41]. Hence, the ^{8}B rate can be measured at unprecedented precision if the systematic error is at the level of ~ 1 %.

In the next step, the electron neutrino survival probability, P_{ee}, was reconstructed from the ^{8}B spectrum that was measured with the ^{13}C channel. Subsequently, the P_{ee} spectrum was fitted a constant, in order to test how well this wrong model can be excluded. Furthermore, the simulated spectrum for the ES channel was fitted with the spectrum expected according to the constant P_{ee} model. Finally, the results for both channels were combined to maximize the sensitivity of the analysis.

After 4 y measuring time, the constant P_{ee} model can be excluded with more than $5\,\sigma$ significance if the MSW-LMA prediction is correct. As the amount of intrinsic radioactive background is not known yet, the analysis was repeated with a two orders of magnitude larger intrinsic radioactive background compared to Borexino, which is a very pessimistic scenario. Even in this case, the upturn of the ^{8}B spectrum can be detected with $5\,\sigma$ significance after 5 y. In case that the upturn of the ^{8}B spectrum is not detected after 5 y, this would rule out the MSW-LMA prediction and show that new physics influence P_{ee} in the transition region between matter and vacuum dominated oscillations.

The second major focus of the present work is the study of the potential of LENA to detect the Diffuse Supernova Neutrino Background (DSNB). The DSNB was created by the cumulative neutrino emission of core-collapse supernovae throughout the history of the universe and was not detected up to now, due to its low flux. Detecting the DSNB is important as it allows to measure the average neutrino spectrum of a core-collapse supernova. Furthermore, it is an independent method to measure the redshift dependent supernova rate.

First of all, the DSNB spectra were simulated with four different mean supernova

neutrino energies ranging from $\langle E_\nu \rangle = 12\,\mathrm{MeV}$ to $\langle E_\nu \rangle = 21\,\mathrm{MeV}$ [34], using the inverse beta decay (IBD) channel ($\bar{\nu}_e + p \rightarrow e^+ + n$) which is only sensitive to $\bar{\nu}_e$. Depending on $\langle E_\nu \rangle$, 85 to 156 DSNB events are expected after 10 y of data taking. Subsequently, the contribution of the different background sources was studied. Contrary to Super-Kamiokande [39], LENA can detect the 2.2 MeV gamma of the neutron capture on hydrogen. Hence, the delayed coincidence of the prompt positron and the delayed neutron signal can be used to suppress background. One of the remaining backgrounds are reactor and atmospheric antielectron neutrinos. They pose an indistinguishable background and thus limit the detection window to neutrino energies between 9.5 MeV and 25 MeV. Due to this energy cut, the already small event rate is reduced to 48-95 events per 10 y.

Another two background sources are due to cosmic muons. While the majority of the produced cosmic radioisotopes can be vetoed by the delayed coincidence condition, ^{9}Li ($Q_{\beta^-} = 13.6\,\mathrm{MeV}$) can β^- decay into an excited state, leading to the emission of a neutron. This $\beta^- - n$ decay has the same delayed coincidence signature as the IBD reaction, and the rate above 9.5 MeV was calculated to be $\sim 1 \cdot 10^3 \frac{\mathrm{events}}{47.8\,\mathrm{kt \cdot 10\,y}}$. This background can be reduced to less than 0.01 events per 10 y by vetoing a cylinder with 2 m radius around each cosmic muon for 2.5 s, which introduces a negligible dead time of 0.2 %.

The other muon-induced background are fast neutrons, which are produced by cosmic muons in the surrounding rock. These fast neutrons have a large range and can propagate into the target volume without triggering the muon veto. Inside the target volume, the neutron produces a prompt signal due to scattering reactions on protons and carbon and a delayed signal when it gets captured on a free proton after thermalization, thus mimicking the IBD event signature. Using the GEANT4 based Monte-Carlo simulation, the fast neutron rate was found to be $\sim 4.9 \cdot 10^2 \frac{\mathrm{events}}{47.8\,\mathrm{kt \cdot 10\,y}}$. The fast neutron background can be reduced by using a smaller fiducial volume. If the radius of the fiducial volume is set to 11 m, the fast neutron rate is reduced to $\sim 4.9 \pm 0.4(\mathrm{stat.}) \frac{\mathrm{events}}{30.1\,\mathrm{kt \cdot 10\,y}}$, but the DSNB event rate is also reduced by over 30 %.

While atmospheric $\bar{\nu}_e$ are an indistinguishable background for the DSNB detection, NC reactions of atmospheric neutrinos of all flavours also provide a background. In these NC reactions, nucleons and heavier fragments are knocked out of a carbon nucleus. In case that a single neutron is emitted, the atmospheric NC event has the same delayed coincidence signature as an IBD event. The atmospheric NC background amounts to $\sim 3.3 \cdot 10^3 \frac{\mathrm{events}}{47.8\,\mathrm{kt \cdot 10\,y}}$ in the DSNB detection window, which is in agreement with the KamLAND measurement of this background [101] and more than one order of magnitude above the DSNB rate.

As IBD events have a typical pulse shape different from that of atmospheric NC events, the atmospheric NC background can be suppressed by a pulse shape anal-

ysis. However, due to the rather small differences between the two pulse shapes, a very restrictive pulse shape cut needs to be applied which accepts only 40 % of all IBD events. In that case, the atmospheric NC background can be reduced by almost two orders of magnitude to 21.8 ± 0.4(stat.) events per 10 y, using a fiducial volume with 13.0 m radius. The same cut also reduced the fast neutron rate to 1.8 ± 0.2(stat.) events per year.
Overall, using a fiducial volume with 13.0 m radius and applying a pulse shape cut with 40 % IBD acceptance, 28 background events per 10 y are expected between 9.5 MeV and 25 MeV, while the DSNB rate ranges from 18 to 35 events per 10 y. Assuming that the expected value of the background rate is known with 5 % uncertainty and that the current models are correct, the DSNB can be detected with more than $3\,\sigma$ significance after 10 y of data taking.
In case that no DSNB signal is found, the current Super-Kamiokande limit on the DSNB flux above 17.3 MeV [39] would be improved by a factor of about 8 to $0.4\,\bar{\nu}_\mathrm{e}\,\mathrm{cm}^{-2}\mathrm{s}^{-1}$ (90 % C.L.). Furthermore, all current standard DSNB models would be ruled out with more than 90 % C.L.

List of Figures

List of Tables

Bibliography

[1] D. Autiero et al. Large underground, liquid based detectors for astro-particle physics in Europe: scientific case and prospects. *JCAP*, 0711:011, 2007.

[2] M. Wurm et al. The next generation liquid-scintillator neutrino observatory LENA. *Astroparticle Phys.*, 35:685–732, 2012. arXiv:1104.5620.

[3] L. Bergström, A. Goobar. *Cosmology and Particle Astrophysics*, volume 2. Springer, 2003.

[4] The Super-Kamiokande Collaboration, Y. Fukuda et al. Evidence for oscillation of atmospheric neutrinos. *Phys.Rev.Lett.*, 81:1562–1567, 1998. arXiv:hep-ex/9807003.

[5] SNO Collaboration. Electron Energy Spectra, Fluxes, and Day-Night Asymmetries of ^8B Solar Neutrinos from the 391-Day Salt Phase SNO Data Set. *Phys. Rev.*, C72:055502, 2005. arXiv:hep-ex/0508053v2.

[6] KamLAND Collaboration. First results from kamland: Evidence for reactor anti-neutrino disappearance. *Phys.Rev.Lett.*, 90:021802, 2003. arXiv:hep-ex/0212021.

[7] S.M. Bilenky, C. Giunti, W. Grimus. Phenomenology of Neutrino Oscillations. *Prog.Part.Nucl.Phys.*, 43:1–86, 1999. arXiv:hep-ph/9812360v4.

[8] N. Schmitz. *Neutrinophysik*. Teubner Studienbücher, Stuttgart, 1997.

[9] J. Beringer et al. (Particle Data Group). *Phys.Rev.*, D86:010001, 2012. http://pdg.lbl.gov.

[10] M. Zralek. From kaons to neutrinos: quantum mechanics of particle oscillations. *Acta. Phys. Polon.*, B29:3925–3956, 1998. arXiv:hep-ph/9810543.

[11] Super-Kamiokande Collaboration. Solar neutrino measurements in super-kamiokande-i. *Phys. Rev.*, D73:112001, 2006. arXiv:hep-ex/0508053v2.

[12] E.K. Akhmedov, M.A. Tortola, J.W.F. Valle . A simple analytic three-flavour description of the day-night effect in the solar neutrino flux. *JHEP*, 0405:057, 2004. arXiv:hep-ph/0404083.

[13] P.C. de Holanda, Wei Liao, A.Yu. Smirnov . Towards precision measurement in solar neutrinos. *Nucl. Phys.*, B702:307–332, 2004. arXiv:hep-ph/0404042.

[14] J. N. Bahcall, A. M. Serenelli, S. Basu. New solar opacities, abundances, helioseismology, and neutrino fluxes. *Astrophys. J.*, 621:L85–L88, 2005. arXiv:astro-ph/0412440.

[15] J.N. Bahcall, P.I. Krastev. Does the Sun Appear Brighter at Night in Neutrinos? *Phys. Rev.*, C56:2839–2857, 1997. arXiv:hep-ph/9706239.

[16] The Borexino Collaboration. Absence of a day-night asymmetry of 862 keV Be-7 solar neutrino rate in Borexino and MSW oscillation parameters. *Phys.Lett.*, B707:22–26, 2012. arXiv:1104.2150.

[17] The Borexino Collaboration. First evidence of pep solar neutrinos by direct detection in borexino. *Phys.Rev.Lett.*, 108:051302, 2011. arXiv:1110.3230.

[18] H. Minakata and C. Pena-Garay. Solar Neutrino Observables Sensitive to Matter Effects. *Advances in High Energy Physics*, 2012:349686, 2012. arXiv:1009.4869.

[19] P.C. de Holanda, A. Yu. Smirnov. Solar neutrino spectrum, sterile neutrinos and additional radiation in the Universe. *Phys.Rev. D*, 83:113011, 2011. arXiv:1012.5627.

[20] J.N. Bahcall. Solar Neutrinos. *Encyclopedia of Physics, 3rd edition*, Vol. 2:2242, 2005.

[21] E. Adelberger et al. Solar Fusion Cross Sections. *Rev.Mod.Phys.*, 70:1265–1292, 1998. arXiv:astro-ph/9805121.

[22] J.N. Bahcall, M.C. Gonzalez-Garcia, C. Penya-Garay. Does the sun shine by pp or cno fusion reaction? *Phys.Rev.Lett.*, 90:131301, 2003. arXiv:astro-ph/0212331.

[23] J.N. Bahcall, M.H. Pinsonneault. What do we (not) know theoretically about solar neutrino fluxes. *Phys.Rev.Lett.*, 92:121301, 2004. arXiv:astro-ph/0402114.

[24] J.N. Bahcall, A.M. Serenelli, S. Basu. New solar opacities, abundances, helioseismology, and neutrino fluxes. *Astrophys.J.*, 621:L85–L88, 2005. arXiv:astro-ph/0412440.

[25] M. Asplund, N. Grevesse, J. Sauval. The solar chemical composition. *Nucl. Phys.*, A777:1–4, 2006. arXiv:astro-ph/0410214.

[26] N. Grevesse and A.J. Sauval. *Space Sci. Rev.*, 85:161, 1998.

[27] Borexino Coll., G. Bellini et al. Precision measurement of the ^{7}Be solar neutrino interaction rate in Borexino. *Phys. Rev. Lett.*, 107:141302, 2011. arXiv:1104.1816.

[28] The SNO collaboration. Measurement of the ν_e and total ^{8}b solar neutrino fluxes with the sudbury neutrino observatory phase-iii data set. *Phys. Rev.*, C87:015502, 2013.

[29] Borexino Coll., G. Bellini et al. Measurement of the solar ^{8}B neutrino rate with a liquid scintillator target and 3 MeV energy threshold in the Borexino detector. *Phys. Rev.*, D82:033006, 2010.

[30] S. Horiuchi, J.F. Beacom, E. Dwek. The Diffuse Supernova Neutrino Background is detectable in Super-Kamiokande. *Phys. Rev.*, D79:083013, 2009. arXiv:0812.3157.

[31] R. Diehl et al. Radioactive ^{26}Al and massive stars in the Galaxy. *Nature*, 439:45–47, 2006. arXiv:astro-ph/0601015.

[32] S. Ando and K. Sato. Relic neutrino background from cosmological supernovae. *New J. Phys.*, 6:170, 2004. arXiv:astro-ph/0410061.

[33] E. E. Salpeter. *Astrophys. J.*, 121:161, 1955.

[34] T. Yoshida et al. Neutrino-Nucleus Reaction Cross Sections for Light Element Synthesis in Supernova Explosions. *Astrophys. J.*, 686:448, 2008. arXiv:0807.2723.

[35] H. Yuksel and J.F. Beacom. Neutrino Spectrum from SN 1987A and from Cosmic Supernovae. *Phys. Rev.*, D76:083007, 2007. arXiv:astro-ph/0702613.

[36] M. T. Keil, G. G. Raffelt, H. T. Janka. Monte carlo study of supernova neutrino spectra formation. *Astrophys.J.*, 590:971–991, 2003. arXiv:astro-ph/0208035v2.

[37] T. A. Thompson, A. Burrows, P. A. Pinto. Shock breakout in core-collapse supernovae and its neutrino signature. *Astrophys.J.*, 592:434, 2003. arXiv:astro-ph/0211194.

[38] K. Sumiyoshi, S. Yamada, H. Suzuki. Dynamics and neutrino signal of black hole formation in non-rotating failed supernovae. I. EOS dependence. *Astrophys. J.*, 667:382–394, 2007. arXiv:astro-ph/0706.3762.

[39] The Super-Kamiokande Collaboration. Supernova Relic Neutrino Search at Super-Kamiokande. *Phys. Rev.*, D85:052007, 2012. arXiv:1111.5031.

[40] B. T. Cleveland et al. *Astrophys. J.*, 496:505, 1998.

[41] Y. Takeuchi. Results from Super-Kamiokande. In *The XXIV International Conference on Neutrino Physics and Astrophysics (Neutrino 2010)*, June 2010. arxiv:1112.3425.

[42] A. Gouvea, J. Jenkins . What can we learn from neutrino electron scattering? *Phys. Rev.*, D74:033004, 2006. arXiv:hep-ph/0603036.

[43] J. D. Jackson. *Classical Electrodynamics*. Wiley, New York, 1962.

[44] M. Wurm. *Cosmic Background Discrimination for the Rare Neutrino Event Search in Borexino and LENA*. PhD thesis, Technische Universität München, 2009.

[45] H. Sekiya. Low energy Investigations at Kamioka Observatory, 2012. arXiv:1301.7125.

[46] The SNO collaboration. Low-energy-threshold analysis of the phase i and phase ii data sets of the sudbury neutrino observatory. *Phys. Rev.*, C81:055504, 2010.

[47] The Borexino Collaboration. Cosmogenic Backgrounds in Borexino at 3800 m water-equivalent depth, 2013. arXiv:1304.7381.

[48] T. Marrodàn Undagoitia. *Measurement of light emission in organic liquid scintillators and studies towards the search for proton decay in the future large-scale detector LENA*. PhD thesis, Technische Universität München, 2008.

[49] Borexino Collaboration. First real time detection of ^{7}Be solar neutrinos by Borexino. *Phys.Lett.*, B658:101–108, 2007. arXiv:0708.2251v2.

[50] The Borexino Collaboration. Measurement of geo-neutrinos from 1353 days of Borexino, 2013. arXiv:1303.2571.

[51] KamLAND Collaboration. Production of Radioactive Isotopes through Cosmic Muon Spallation in KamLAND. *Phys.Rev.*, C81:025807, 2010. arXiv:0907.0066.

[52] L. Oberauer, P. Pfahler, M. Wurm. LAGUNA-LBNO Liquid Scintillator Specification Document. unpublished, 2012.

[53] V. A. Kudryavtsev, N. J. C. Spooner, J. E. McMillan. Simulations of muon-induced neutron flux at large depths underground. *Nucl. Instrum. Meth.*, A505:688–698, 2003. arXiv:hep-ex/0303007.

[54] M. Wurm et al. Search for modulations of the solar Be-7 flux in the next-generation neutrino observatory LENA. *Phys.Rev.*, D83:032010, 2011. arXiv:1012.3021.

[55] H. Janka et al. Core-Collapse Supernovae: Reflections and Directions, 2012. arXiv:1211.1378.

[56] M. Wurm et al. The next-generation liquid-scintillator neutrino observatory LENA. *Astroparticle Physics*, 35(11):685 – 732, 2012. arXiv:1104.5620.

[57] M. Kaiser. *Supernova Neutrinos in LENA: Towards a Time- and Flavor-Resolved Analysis*. Diploma thesis, Universität Hamburg, 2012.

[58] The KamLAND Collaboration. Reactor On-Off Antineutrino Measurement with KamLAND, 2013. arXiv:1303.4667.

[59] K.A. Hochmuth et al. Probing the earth's interior with a large-volume liquid scintillator detector. *Astropart.Phys.*, 27:21–29, 2007. arXiv:hep-ph/0509136v3.

[60] R. Möllenberg. *Monte Carlo Study of the Fast Neutron Background in LENA*. Diploma thesis, Technische Universität München, 2009.

[61] W.F. McDonough and S.S. Sun. The composition of the Earth. *Chem. Geol.*, 120:223, 1995.

[62] D.Hellgartner, M. Kaiser, K. Loo, S. Lorenz, R. Möllenberg, Y. Novikov, M. Soiron, M. Wurm. Report on Detector Performance Evaluation. unpublished, 2013.

[63] P. Nath, P. F. Perez. Proton stability in grand unified theories, in strings, and in branes. *Phys.Rept.*, 441:191–317, 2007. arXiv:hep-ph/0601023v3.

[64] Super-Kamiokande Collaboration,H. Nishino,S. Clark et a. Search for proton decay via $p \to e^+\pi^0$ and $p \to \mu^+\pi^0$ in a large water cherenkov detector. *Phys.Rev.Lett.*, 102:141801, 2009. arXiv:hep-ex/0903.0676v2.

[65] Super-Kamiokande Collaboration. Search for nucleon decay via modes favored by supersymmetric grand unification models in super-kamiokande-i. *Phys.Rev.*, D72:052007, 2005. arXiv:hep-ex/0502026v1.

[66] P. Coloma, Tracey Li, S. Pascoli. A comparative study of long-baseline superbeams within LAGUNA for large θ_{13}, 2012. arXiv:1206.4038.

[67] M. Wurm. The LENA project. In *522. Willhelm and Else Heraeus-Seminar: Exploring the neutrino sky and fundamental particle physics on the Megaton scale*, January 2013.

[68] S. Lorenz, 2013. private communication.

[69] G.M. Harper, A. Brown, E.F. Guinan. A new VLA-HIPPARCOS distance to betelgeuse and its implications. *Astron. J.*, 135:1430, 2008.

[70] D. Hellgartner. *Lepton track reconstruction in LENA and attenuation length measurements in liquid scintillators*. Diploma thesis, Technische Universität München, 2011.

[71] Q. Meindl. *Reconstruction and Measurement of Cosmogenic Signals in the Neutrino Experiment Borexino*. PhD thesis, Technische Universität München, 2013.

[72] S. Agostinelli et al. Geant4 - a simulation toolkit. *Nuclear Instruments and Methods*, 1A 506:250–303, 2003.

[73] J. Winter. *Phenomenology of Supernova Neutrinos, Spatial Event Reconstruction, and Scintillation Light Yield Measurements for the Liquid-Scintillator Detector LENA*. Diploma thesis, Technische Universität München, 2007.

[74] A. Willms. *C++ Programmierung*. Addison-Wesley, 1997.

[75] S. Lorenz. *Discrimination of Neutral Current Background in a Future Long-Baseline Experiment with LENA*. Diploma thesis, Universität Hamburg, 2012.

[76] Geant4 Colloboration. Geant4: Physics reference manual, 2012. http://geant4.web.cern.ch/geant4/UserDocumentation/UsersGuides/PhysicsReferenceManual/fo/PhysicsReferenceManual.pdf.

[77] Geant4 Colloboration. Geant4: Testing and validation, 2009. http://geant4.web.cern.ch/geant4/results/results.shtml.

[78] J. Apostolakis et al. Progress in hadronic physics modelling in geant4. *Journal of Phys.: Conference Series*, 160:012073, 2009.

[79] L. Oberauer, C. Grieb, F. von Feilitzsch, I Manno. Light Concentrators for Borexino and CTF. *Nucl. Instrum. Meth.*, A530:453–462, 2004. arXiv:physics/0310076.

[80] S. Aiello et al. The Measurement of Late-Pulses and After-Pulses in the Large Area Hamamatsu R7801 Photomultiplier with Improved Quantum-Efficiency Photocathode. http://www.lnf.infn.it/sis/preprint/detail.php?id=5251.

[81] J. B. Birks. *The Theory and Practise of Scintillation Counting*. Pergamon-Press, London, 1964.

[82] S. Wagner. *Ionization Quenching by Low Energy Electrons in the Double Chooz Scintillators*. Diploma thesis, University of Heidelberg, 2010.

[83] H.M. O'Keefe,E. O'Sullivan, M.C. Chen. Scintillation decay time and pulse shape discrimination in oxygenated and deoxygenated solutions of linear akylbenzene for the SNO+ experiment. *Nucl.Instrum.Meth.A*, 460:119–121, 2011. arXiv:1102.0797.

[84] J. Meyer. *Realization and Characterization of the Muon Veto Scintillator and the Buffer Liquid of the Double Chooz Experiment*. Diploma thesis, Technische Universität München, 2010.

[85] The Borexino Collaboration. Final results of Borexino Phase-I on low energy solar neutrino spectroscopy, 2013. arXiv:1308.0443.

[86] J.N. Bahcall. The pp solar neutrino energy spectrum. http://www.sns.ias.edu/ jnb/SNdata/ppspectrum.html.

[87] J.N. Bahcall and R.K. Ulrich. Solar models, neutrino experiments, and helioseismology. *Rev. Mod. Phys.*, 60:297–372, 1988. http://www.sns.ias.edu/ jnb/.

[88] J.N. Bahcall and E.Lisi, D.E. Alburger, L.D. Braeckeleer, S.J. Freedman, J. Napolitano. Standard neutrino spectrum from ^8B decay. *Phys. Rev.*, C54:411, 1996. http://www.sns.ias.edu/ jnb/.

[89] J.N. Bahcall. Hep energy spectrum. http://www.sns.ias.edu/ jnb/SNdata/Export/Hepspectrum/hepspectrum.dat.

[90] A. Ianni, D. Montanino, F.L. Villante. How to observe ^{8}B solar neutrinos in liquid scintillator detectors. *Phys. Lett.*, B627:38–48, 2005. arXiv:physics/0506171.

[91] R. B. Firestone and V.S. Shirley (Ed.). *Table of Isotopes, eight edition.* John Wiley and Sons, 1996.

[92] J.C. Maneira. *Calibration and Monitoring for the Borexino Solar Neutrino Experiment.* PhD thesis, Universidade de Lisboa, 2001.

[93] M. Hofmann. *Liquid Scintillators and Liquefied Rare Gases for Particle Detectors.* PhD thesis, Technische Universität München, 2012.

[94] R. Brun, F. Rademakers. *Nucl. Inst. and Meth. Phys.*, Res. A 389:81–86, 1997. http://root.cern.ch.

[95] K. A. Hochmuth. *Low Energy Neutrinos as geological and astrophysical Messengers.* PhD thesis, Technische Universität München, 2008.

[96] E. Gatti, F. De Martini. A new linear method of discrimination between elementary particles in scintillation counters. *Nuclear Electronics*, vol. 2:265–276, 1962.

[97] T. Lewke, 2013. private communication.

[98] A. Strumia, F. Vissani. Precise quasielastic neutrino/nucleon cross section. *Phys. Lett.*, B564:42–54, 2003.

[99] Triangle Universities Nuclear Laboratory TUNL. Nuclear data evaluation, retrieved July 5^{th}, 2013 . http://www.tunl.duke.edu/nucldata.

[100] LVD Collaboration. Measurement of the Neutron Flux Produced by Cosmic-Ray Muons with LVD at Gran Sasso. In *Proc. of 26th Intern. Cosmic Ray Conf.*, Salt Lake City, USA, 1999. arXiv:hep-ex/9905047.

[101] The KamLAND Collaboration. Search for extraterrestial antineutrino sources with the KamLAND detector. *Astrophys. J.*, 745:193, 2012. arXiv:1105.3516.

[102] M. Wurm et al. Detection potential for the diffuse supernova neutrino background in the large liquid-scintillator detector lena. *Phys. Rev. D75*, 023007, 2007. arXiv:astro-ph/0701305v1.

[103] C. Andreopoulos et al. The GENIE Neutrino Monte Carlo Generator. *Nucl. Instrum. Meth.*, A614:87–104, 2010.

[104] The T2K Collaboration. The T2K Experiment. *Nucl. Instrum. Meth.*, A659:106, 2011. arXiv:1106.1238.

[105] The IceCube Collaboration. The Design and Performance of IceCube Deep Core. *Astroparticle Phys.*, Volume 35, Issue 10:615–624, 2012. arXiv:1109.6096.

[106] G.D. Barr, T.K. Gaisser, P. Lipari, S. Robbins, T. Stanev . A three-dimensional calculation of atmospheric neutrinos. *Phys. Rev.*, D70:023006, 2004. arXiv:astro-ph/0403630.

[107] Y. Kamyshkov, E. Kolbe. Signatures of Nucleon Disappearance in Large Underground Detectors. *Phys.Rev. D*, 67:076007, 2003. arXiv:nucl-th/0206030v2.

[108] L. Lapikas, G. van der Steenhoven, L. Frankfurt, M. Strikman and M. Zhalov. The transparency of C-12 for protons. *Phys. Rev.*, C61:064325, 2000.

[109] A. J. Koning, S. Hilaire, and M.C. Duijvestijn. Talys 1.0. In *Proceedings of the International Conference on Nuclear Data for Science and Technology -ND 2007*, Nice, France, 2007. http://www.talys.eu.

[110] J. Winter. *Neutron scattering in organic liquid-scintillator and phenomenology of Supernova Neutrinos in LENA*. PhD thesis, Technische Universität München, 2013.

[111] E. Litvinoch, I. Machulin, S. Silaeva, S. Sukhotin, Y. Suvorov. Calibration of Borexino using the Am-Be source, 2009. Internal Report.

[112] J.R. Klein, A. Roodman. Blind Analysis in Nuclear and Particle Physics. *Ann. Rev. Nucl. Part. Sci.*, 55:141–163, 2005. http://www.osti.gov/scitech/biblio/889148.

[113] G. J. Feldman, R.D. Cousins. A Unified Approach to the Classical Statistical Analysis of Small Signals. *Phys. Rev.*, D57:3873–3889, 1998. arxiv:physics/9711021.

[114] W. Rolke, A. Lopez, J. Conrad, F. James . Limits and Confidence Intervals in presence of nuisance parameters. *Nucl. Instrum. Meth.*, A551:493–503, 2005.

Danksagung

An dieser Stelle möchte ich mich noch bei allen bedanken, ohne die diese Arbeit so nicht möglich gewesen wäre. Zuerst möchte ich mich bei Prof. Franz von Feilitzsch und seinem Nachfolger Prof. Stefan Schönert für die freundliche Aufnahme am Lehrstuhl E15 und die Möglichkeit, diese Arbeit anzufertigen, bedanken.
Bei meinem Doktorvater Prof. Lothar Oberauer möchte ich mich für die hervorrangende Betreuung dieser Arbeit und dafür das er immer ein offenes Ohr hatte bedanken. Die vielen Gespräche die wir in der letzten Jahren, auch über nichtphysikalische Themen, hatten werden mir immer im Gedächtnis bleiben. Außerdem kann man mit ihm als Beifahrer auf ein Navi problemlos verzichten.
Besonders möchte ich bei Dominikus Hellgartner dafür bedanken, dass er trotz Hochzeitsstress diese Arbeit korrigiert hat und dabei immer jeden noch so kleinen Fehler entdeckt hat. Darüber hinaus hatte er sich während der vergangen Jahre immer wieder Zeit genommen, um mit mir über meine Arbeit zu diskutieren und konnte mir durch seine guten Ideen stets weiterhelfen. Außerdem hat er es mir nie übel genommen, wenn durch ein Update der LENA Monte-Carlo-Simulation seine Analyse mal wieder nicht funktionierte.
Einen erheblichen Anteil am Erfolg dieser Arbeit hatte auch Dr. Michael Wurm, der immer gute Anregungen hatte und diese Arbeit auch Korrekturgelesen hat.
Ein großer Dank gilt meinen aktuellen und ehemaligen Bürokollegen: Dr. Martin Hofmann, Dr. Achim Gütlein, Nils Haag, Judith Meyer, Alexander Neumeier und Simon Appel, die immer für eine gute Arbeitsatmosphäre gesorgt hatten und mit denen man jederzeit über alles diskutieren konnte.
Bei unserer Sekretärin Maria Bremberger möchte mich dafür bedanken, dass sie alle bürokratische Angelegenheiten so weit wie möglich von mir ferngehalten hat und immer zur Verfügung stand, wenn ich ihre Hilfe benötigte.
Des Weiteren möchte ich bei allen anderen E15 Mitgliedern bedanken. Durch euch werden die letzten Jahre trotz einiger stressiger Momente immer positiv in meiner Erinnerung bleiben.
Zu guter Letzt möchte ich mich bei meiner Familie dafür bedanken, dass sie mir immer den nötigen Rückhalt gegeben hat.